Magnetocaloric and magnetoresistive properties of La0.67Ca0.33-xSrxMnO3

Dinesen, Anders Reves; Pryds, Nini; Mørup, Steen; Linderoth, Søren

Publication date:
2003

Document Version
Publisher's PDF, also known as Version of record

RISØ

Risø-PhD-5

Magnetocaloric and magnetoresistive properties of $La_{0.67}Ca_{0.33-x}Sr_xMnO_3$

Anders Reves Dinesen

Risø National Laboratory
Roskilde
Denmark
August 2004

Risø-PhD-Thesis

Author: Anders Reves Dinesen
Title: Magnetocaloric and magnetoresistive properties of $La_{0.67}Ca_{0.33-x}Sr_xMnO_3$
Department: Materials Research Department

This thesis is submitted in partial fulfillment of the requirements for obtaining the degree of PhD at the Technical University of Denmark (DTU).

Abstract This thesis presents results of an experimental investigation of magnetocaloric and magnetoresistive properties of a series of polycrystalline Ca- and Sr-doped lanthanum manganites, $La_{0.67}Ca_{0.33-x}Sr_xMnO_3$ ($0 \le x \le 0.33$), with the perovskite structure. The samples consisted of sintered oxide powders prepared the glycine-nitrate combustion technique. The compounds were ferromagnetic and showed a Curie transition in the temperature range 267–370 K (T_C increased with increasing x). An analysis of the structural properties was carried out by means of x-ray diffraction and the Rietveld technique. The variation of the Ca/Sr ratio was found to cause a transition from orthorhombic to rhombohedral symmetry in the composition range $0.110 < x < 0.165$. The analysis suggested a strong correlation between structural properties and magnetism, for instance a relationship between the mean Mn–O–Mn bond angle and the Curie temperature. The Mn–O–Mn bonds mediate ferromagnetism and electrical transport in these materials via the double-exchange mechanism. The magnetocaloric effect of the $La_{0.67}Ca_{0.33-x}Sr_xMnO_3$ samples was measured directly and indirectly (by means of magnetization measurements). All the samples showed a magnetocaloric effect in the vicinity of T_C. A model for the magnetocaloric effect based on Weiss mean field theory and classical theories for heat capacities was developed. The model provided reasonable predictions of the magnetocaloric properties of the samples. The compounds with low Sr content showed a magnetocaloric effect comparable to that of Gadolinium, the prototypical working material for magnetic refrigeration at room temperature. A less comprehensive part of the investigation regarded the magnetoresistive properties of the $La_{0.67}Ca_{0.33-x}Sr_xMnO_3$ system. It was found that the polycrystalline nature of the compounds played a decisive role for the magnetotransport properties. Characteristic grain boundary effects, such as a low-field magnetoresistance, which is absent in single-crystalline perovskites, were observed. The low-field effect is usually ascribed to spin-dependent scattering in grain boundaries. Qualitatively the results obtained for the $La_{0.67}Ca_{0.33-x}Sr_xMnO_3$ samples were consistent with this model. The resistivity contribution arising from the presence of grain boundaries increased with increasing Sr content. Reducing the sintering temperature also enhanced the grain boundary effects. The samples with low Sr content showed colossal magnetoresistance (CMR) near room temperature (~20-45 % with $\mu_0 H = 0.8$ T). The CMR effect was negligible for the samples with high Sr content. However, these samples exhibited a grain boundary-related magnetoresistance at room temperature.

Risø-PhD-5
August 2004

ISSN 0106-2840
ISBN 87-550-3223-0
ISBN 87-550-3224-9 (internet)

Contract no.:

Group's own reg. no.:

Sponsorship:

Cover :

Pages: 103
Tables: 6
References: 82

Risø National Laboratory
Information Service Department
P.O.Box 49
DK-4000 Roskilde
Denmark
Telephone +45 46774004
bibl@risoe.dk
Fax +45 46774013
www.risoe.dk

Contents

Preface and acknowledgements

This thesis is submitted in partial fulfillment of the requirements for obtaining the degree of Ph.D. at the Technical University of Denmark (DTU). The experimental work was carried out partly at the Department of Physics, DTU and partly at the Materials Research Department, Risø National Laboratory during the period of March 2000 to March 2003. The work was carried out under supervision of Dr. S. Linderoth, Materials Research Department, Risø, Prof. S. Mørup, Department of Physics, DTU, and Dr. N. H. Pryds, Materials Research Department, Risø. The work was financed by Risø National Laboratory and the Danish Research Academy.

I would like to extend my deepest gratitude to my supervisors Dr. Søren Linderoth, Prof. Steen Mørup, and Dr. Nini H. Pryds, who have provided me with constant support and encouragement throughout the past three years.

I would also like to express my thanks to the staff at to Materials Research Department, Risø, for being very helpful and supportive. In particular, I would like to thank: John Kjøller, Ole Emil Olsen, Ebtisam Abdellahi, Asger Abrahamsen, Jørgen Bilde-Sørensen, Morten Mostgaard Eldrup, John A. Wert, Allan Schrøder Pedersen, and Helmer Nilsson.

The staff members at the Department of Physics are also thanked. I would like to mention: Helge Rasmussen, Claus Schelde Jacobsen, Jianzhong Jiang, and Thomas Aaerø Anhøj. Otto V. Nielsen is gratefully acknowledged for assiting in magnetization measurements and for providing the Department of Physics with a vibrating-sample magnetometer.

I would like to thank Carsten Trebbien and Christian Bender Koch for helping with the preparation of this manuscript.

I also owe a dept of gratitude to Jørgen Schou and Bo Toftmann Christensen, Optics and Fluid Dynamics Department, Risø, and Jørgen Bøttiger, Department of Physics and Astronomy, University of Aarhus, for assisting with part of my work, not covered by this thesis.

Finally, I would like to thank my spouse for being very supportive and patient during stressed periods of this work.

Anders Reves Dinesen
March 10, 2003

Revised and reprinted August 2004

Resumé

Formålet med nærværende afhandling er at belyse de magnetokaloriske og magnetoresistive egenskaber ved en serie af ferromagnetiske Ca- og Sr-substituerede lanthanmanganoxider med den generelle formel $La_{0.67}Ca_{0.33-x}Sr_xMnO_3$ ($0 \le x \le 0.33$). Disse materialer har den såkaldte perovskit-krystalstruktur. De tilhører familien af manganitter med blandet valens, som er kendt for deres specielle magnetiske og elektriske egenskaber, som viser sig at være stærkt forbundne, hvilket bl.a. forklares ved den ferromagnetiske koblingsmekanisme kaldet *double exchange*. Syv $La_{0.67}Ca_{0.33-x}Sr_xMnO_3$ prøver (med x = 0, 0.055, 0.110, 0.165, 0.220, 0.275 og 0.33) blev syntetiseret i form af finkornede pulvere ved glycin-nitrat forbrænding. Efter pulverpresning og sintring bestod prøverne af hårde stykker keramik. Prøvernes sammensætning blev målt med energidispersiv røntgenspektroskopi (EDS) og svarede stort set til ovennævnte værdier af x. EDS-analysen tillod dog ikke en nøjagtig bestemmelse af iltindholdet, som kunne forventes at variere fra den nominelle værdi. Prøvernes overflademorfologi blev studeret med scanning-elektron mikroskopi (SEM). Det stigende Sr-indhold forårsagede en gradvis reduktion af kornstørrelsen og forøgelse af porøsiteten. Prøvernes strukturelle egenskaber blev undersøgt ved hjælp af røntgendiffraktion (XRD) og Rietveld-analyse. En faseovergang fra ortorhombisk til rhombohedral symmetri for $x \approx 0.15$ blev observeret. På grundlag af Rietveld-analysen kunne en gradvis ændring af Mn–O–Mn bindingsvinklen i materialerne påvises. Dette syntes at være den direkte årsag til en stigning af Curietemperaturen fra 267 K for $La_{0.67}Ca_{0.33}MnO_3$ til 370 K for $La_{0.67}Sr_{0.33}MnO_3$. Prøvernes magnetokaloriske egenskaber blev målt efter to forskellige fremgangsmåder. Den adiabatiske temperaturændring som følge af påtrykning af et ydre magnetfelt blev målt direkte. Den magnetiske entropiændring, som også er et mål for den magnetokaloriske effekt, blev beregnet på grundlag af magnetiseringsmålinger. Alle prøverne udviste en maksimal magnetokalorisk effekt ved deres respektive Curie-temperatur i god overensstemmelse med den termodynamiske teori. En model for den magnetokaloriske effekt i $La_{0.67}Ca_{0.33-x}Sr_xMnO_3$ systemet blev opstillet, og det viste sig muligt at reproducerede de eksperimentelle resultater. Prøverne med lavt Sr indhold udviste en magnetokalorisk effekt af samme størrelsesorden som den magnetokaloriske effekt, der kan observeres i rent gadolinium – det eneste materiale som hidtil har været anvendt praksis i forbindelse med magnetisk køling nær stuetemperatur. Magnetisk køling med $La_{0.67}Ca_{0.33-x}Sr_xMnO_3$ som kølemateriale synes derfor at være muligt. Resitiviteten af udvalgte prøver blev målt som funktion af temperatur og påtrykt magnetfelt. To typer magnetoresistans blev observeret. Ved Curietemperaturen udviste prøverne såkaldt *colossal magnetoresistance* (CMR-effekt), d.v.s. en meget stor ændring af resistiviteten som følge af påtrykningen af et ydre magnetfelt. For $La_{0.67}Ca_{0.33}MnO_3$ observeredes en magnetoresistans på over 40 % med et påtrykt felt på 0.8 T. For enkeltkrystallinske materialer aftager CMR-effekten gradvist under Curie-temperaturen. Dette var ikke tilfældet for $La_{0.67}Ca_{0.33-x}Sr_xMnO_3$ prøverne, hvor magnetoresistansen steg systematisk med aftagende temperatur. Denne effekt blev tilskrevet tilstedeværelsen af korngrænser i prøverne. Ved lave temperaturer udviste prøverne et kraftigt magnetoresistanssignal selv i forholdsvis lave magnetfelter (< 0.1 T). Dette er en karakteristik korngrænseeffekt, som normalt forklares ved spredning af polariserede ledningselektroner i korngrænser, som adskiller magnetisk ordnede domæner. De opnåede resultater syntes at være i overensstemmelse med denne model.

Notation

List of symbols

Symbol	Name	Units
B	Magnetic flux density	T
C_P	Specific heat capacity at constant pressure	$Jkg^{-1}K^{-1}$
$C_{P,H}$	Specific heat capacity at constant pressure and constant magnetic field	$Jkg^{-1}K^{-1}$
ΔS_M	Isothermal magnetic entropy change	$Jkg^{-1}K^{-1}$
ΔT_{ad}	Adiabatic temperature change	K
2θ	X-ray diffraction angle	Degrees (= °)
g	Landé factor	Dimensionless
G	Conductivity	$\Omega^{-1}m^{-1}$
H	Magnetic field strength	Am^{-1}
H_I	Initial magnetic field strength	Am^{-1}
H_F	Final magnetic field strength	Am^{-1}
I	Electrical current	A
$LFMR$	Low-field magnetoresistance	Relative
m	Magnetic moment	Am^2
M	Magnetization per unit volume	Am^{-1}
μ	Permeability	NA^{-2}
MR	Magnetoresistance	Relative
n_s	Spins per unit mass	kg^{-1}
P	Pressure	Pa
μ_r	Relative permeability	Dimensionless
ρ	Density	kgm^{-3}
R	Resistance	Ω
ρ	Resistivity	Ωm
ρ_H	Resistivity in an applied field	Ωm
S	Specific entropy	$Jkg^{-1}K^{-1}$
S_M	Specific magnetic entropy	$Jkg^{-1}K^{-1}$
σ	Specific magnetization	Am^2kg^{-1} or $JT^{-1}kg^{-1}$
T	Temperature	K
T_C	Curie temperature	K
Θ_D	Debye temperature	K
V	Volume	m^3
U	Voltage	V
χ	Magnetic susceptibility	Dimensionless

Physical constants

Symbol	Quantity	Value	Units
e	Electron charge	$1.60218 \cdot 10^{-19}$	C
k_B	Boltzmann's constant	$1.3807 \cdot 10^{-23}$	JK^{-1}
μ_0	Vacuum permeability	$4\pi \cdot 10^{-7}$	NA^{-2}
μ_B	Bohr magneton	$9.27400899 \cdot 10^{-24}$	JT^{-1}

Glossary of abbreviations

Abbreviation	Meaning
a. u.	Arbitrary Units
DSC	Differential Scanning Calorimetry
FWHM	Full Width at Half Maximum
XRD	X-Ray Diffraction

1 Introduction and motivation

1.1 Introductory remarks

This thesis presents results of an experimental study on magnetocaloric and magnetoresistive properties a series of calcium- and strontium-doped lanthanum manganese oxides. These oxides belong to the broad family of materials known as the mixed-valence manganites, $R_{1-x}A_xMnO_3$, where R is a rare-earth cation such as La, Pr, Y, Nd, etc., and A is an alkali or alkaline earth cation such as Ca^{2+}, Sr^{2+}, Ba^{2+}, Na^{2+}, K^{2+}, etc. The designation mixed-valence manganites arise from the fact that the materials may contain manganese in several valence states, depending on the substitution parameter x. The materials are also called perovskite manganites because their crystal structure resembles that of the mineral perovskite, and sometimes doped manganites because the substitution of the R cation with an A cation may serve as hole doping. One of the main features of these materials is the close relationship between magnetism and electrical transport properties. End-members with $x = 0$ or $x = 1$ are usually antiferromagnetic insulators, while compounds with intermediate compositions may be ferromagnetic and conducting.

The mixed-valence manganites have been studied for more than five decades but are still considered modern materials because of their wide potential for technological application. Ferromagnetic manganites may exhibit a magnetoresistance effect, which is comparable to, or even larger than, the giant magnetoresistance (GMR) well known from magnetic multilayers, for which reason it has been designated colossal magnetoresistance (CMR). Potential applications of the CMR effect in mixed-valence manganites include magnetic sensors, magnetoresistive read heads, and magnetoresistive random access memory (MRAM). In addition to colossal magnetoresistance, the ferromagnetic mixed-valence manganites may also exhibit a very large magnetocaloric effect, and they seem to be promising candidates as working substances in magnetic refrigeration technology. Manganites play an important role as electrodes in solid oxide fuel cells and they may also be used for catalysis and in oxygen sensors. The present work deals with the two first mentioned phenomena; magnetoresistance and magnetocaloric effect.

Although the magnetocaloric and magnetoresistive properties of mixed-valence manganites seem very promising with regards to technological application, their practical utility is not unlimited. Both the large magnetocaloric and magnetoresistance effects, which may be observed for ferromagnetic manganites, are usually confined to a relatively narrow temperature range around the ferromagnetic transition temperature. $La_{0.67}Ca_{0.33}MnO_3$, for instance, can exhibit an enormous magnetoresistance around the Curie temperature of ~260K but would still be useless for a magnetic sensor device designed for room temperature purposes. Likewise, $La_{0.67}Sr_{0.33}MnO_3$, which has a Curie temperature of about 370 K, cannot be used as refrigerant in a household magnetic refrigerator because the magnetocaloric effect is vanishing at ambient temperatures. The two examples emphasize the importance of being able to modify the Curie temperature and thereby the magnetocaloric and magnetoresistive temperature working range of mixed-valence manganites in a controlled and reproducible manner. This technological need was the main motivation for carrying out a study of the mixed-valence manganite sub-family $La_{0.67}Ca_{0.33-x}Sr_xMnO_3$ ($x \in [0; 0.33]$).

As indicated above, the end-members of the $La_{0.67}Ca_{0.33-x}Sr_xMnO_3$ series, $La_{0.67}Ca_{0.33}MnO_3$ and $La_{0.67}Sr_{0.33}MnO_3$, exhibit a Curie transition below and above room

temperature, respectively. Therefore, it was expected that the solid solutions between the end-members, i.e. the compounds with $0 < x < 0.33$, would have Curie temperatures in the range of the two extreme values, ~260 and ~370K, respectively. This would include Curie temperatures near room temperature and thereby magnetocaloric and magnetoresistive temperature working ranges relevant for devices designed to be operated at ambient conditions. The aim of the experimental study was to understand the possible relationship between composition and the structural, magnetic and electronic properties of the $La_{0.67}Ca_{0.33-x}Sr_xMnO_3$ series and thereby to contribute to the elucidation of the physical properties of these fascinating materials.

1.2 Brief historical review

In the early fifties Jonker and van Santen (1950) reported on the preparation of polycrystalline mixed-valence manganites. They discussed the structural and magnetic properties of $La_{1-x}A_xMnO_3$. They found that the manganites crystallize in the perovskite structure and observed a close relationship between the doping factor x and the structural and magnetic properties. They showed that the end-members with $x = 0$ and $x = 1$ are antiferromagnetic, while compositions with $x \cong 0.3$ are ferromagnetic. Zener (1951a, 1951b) suggested an explanation for this phenomenon, introducing the so-called double exchange mechanism – a ferromagnetic exchange coupling between magnetic ions in different valence states. Volger (1950) measured the magnetoresistance, i.e. the change of resistance due to application of a magnetic field, of a sintered ceramic $La_{0.8}Sr_{0.2}MnO_3$. He observed a negative magnetoresistance of about 8 % near the Curie temperature of the compound. In the nineties new interest in mixed-valence manganites was prompted by the discovery of very large magnetoresistance values in high-quality thin films. Jin *et al*. (1994) reported on thousand-fold change in resistivity and a corresponding magnetoresistance of 127,000 % in a La-Ca-Mn-O thin film (at 77 K and with an external field of 6 T). They called this effect colossal magnetoresistance (CMR). CMR effect has also been observed for Sr- and Ba-doped lanthanum manganites (von Helmolt *et al*., 1994).

Today, the mixed-valence manganites are very generally termed CMR materials, although the extremely large magnetoresistance values are found only in high-quality thin films. Gupta *et al*. (1996) and Hwang *et al*., (1996) showed that polycrystalline manganites part from the CMR effect, which is largest at the Curie temperature, may show a large low-field magnetoresistance below the transition temperature. They ascribed this to grain boundary effects. Grain boundaries give rise to a low-field magnetoresistance, which is absent in single-crystalline materials. A few years ago, Morelli *et al*. (1996) presented results on the magnetocaloric effect of Ca, Ba, and Sr doped lanthanum manganite thin films. They found that the magnetic entropy change due to application of an external field was on the same order of magnitude as that of gadolinium, which is the material usually suggested as working substance in room-temperature magnetic refrigeration. This result prompted a large number of investigations also on polycrystalline manganites, e.g. Zhang *et al*. (1996) and Guo *et al*., (1997).

1.3 Outline of this thesis

The thesis is structured as follows: Chapter 2 gives a general introduction to the structural, magnetic and electronic properties of mixed-valence manganites. Chapter 3 describes the preparation of $La_{0.67}Ca_{0.33-x}Sr_xMnO_3$ samples and some of their basic characteristics (composition and morphology). Chapter 4 presents results on structural and magnetic properties of the $La_{0.67}Ca_{0.33-x}Sr_xMnO_3$ samples. Chapter 5 regards the magnetocaloric properties of the samples. The magnetoresistive properties of the materials are

discussed in Chapter 6. Chapter 7 gives a conclusion. Appendix A contains a brief introduction to the Rietveld refinement technique.

2 Physical properties of mixed-valence lanthanum manganites

2.1 Introduction

The aim of this chapter is to give a general introduction to structural, magnetic, and electronic properties of doped lanthanum manganites, and hereby form the basis for the discussion on the experimental results obtained for the series of $La(Ca,Sr)MnO_3$ compounds under investigation. The samples belong to the broad family of manganese oxides, $R_{1-x}A_xMnO_3$, where R is a rare-earth cation (La^{3+}, Pr^{3+}, Y^{3+}, Nd^{3+}, …) and A an alkali- or alkaline earth cation (Ca^{2+}, Sr^{2+}, Ba^{2+}, Na^{+}, K^{+}, …). These materials are known as mixed-valence manganites, because Mn may coexist in several valence states. Strictly speaking, the term manganite only applies to compounds containing tetravalent Mn but these materials are called manganites regardless of their Mn valence. They are also called doped manganites, referring to the fact that the substitution of the rare-earth cation (R) with an alkali- or alkaline earth cation (A) serves as hole doping. The materials are also known as perovskite or perovskite-like manganites, because their crystal structure resembles that of the mineral perovskite. Part of the following discussion applies to mixed-valence manganites in general, but the main emphasis is laid on the Ca- and Sr-doped lanthanum manganites, $La_{1-x}(Ca,Sr)_xMnO_3$.

2.2 Ionic composition

Lanthanum manganite, $La_{1-x}A_xMnO_3$, can be regarded as a binary system consisting of a solid solution between the end-members $LaMnO_3$ and $AMnO_3$, corresponding to $x = 0$ and $x = 1$, respectively. In general, the oxygen atom has a great avidity for two electrons and studies of the crystal chemistry of lanthanum manganites Jonker and van Santen (1950) have shown that oxygen occurs exclusively as O^{2-}, regardless of the nature of the atom A and the value of x. Thus, the formal valence states of the $x = 0$ end-member is $La^{3+}Mn^{3+}O_3^{2-}$. If, however, a number of La^{3+} ions are substituted by a divalent ion, such as Ca^{2+} or Sr^{2+}, a corresponding number of Mn ions become tetravalent. Hence, the resulting compound have mixed manganese valence and can be written $La_{1-x}^{3+}A_x^{2+}(Mn_{1-x}^{3+}Mn_x^{4+})O_3^{2-}$. The co-existence of manganese in two valence states plays a crucial role to the electrical and magnetic properties of these materials. This point will be treated further below.

2.3 Structural properties

Lanthanum manganites crystallize in the various derivatives of the so-called perovskites structure named after the mineral perovskite, $CaTiO_3$. Figure 1 illustrates the ideal cubic perovskite structure, with the general formula ABO_3. The structure may be conceived as a close-packed array formed of O^{2-} anions and A cations with B cations located at the octahedral interstitial sites. The BO_6 octahedra make contact to each other by their vertices and form a three-dimensional network. In lanthanum manganites the A-sites of the perovskite structure are occupied by La^{3+} and, if $x > 0$, the substituted cations (Ca^{2+}, Sr^{2+}, etc.). The B-sites are occupied by Mn ions.

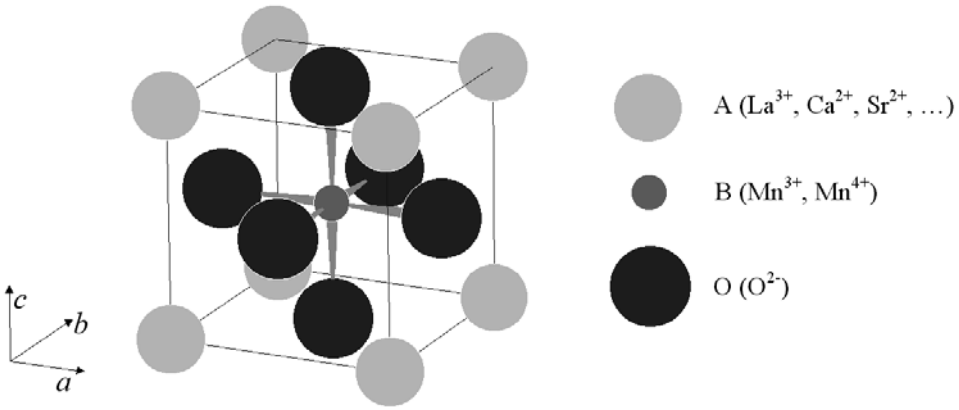

Figure 1. Unit cell structure of prototype cubic perovskite, ABO_3, with the A ions situated at the corners, the B ions in the center and the oxygen ions at the centers of the faces.

The stability of the perovskite structure depends strongly on the size of the A-site and B-site ions. If there is a size mismatch between the A-site and B-site ions and the space in the lattice where they reside, the perovskite structure will become distorted. Goldschmidt (1958) defined a tolerance factor,

$$t^* = \frac{r_A + r_O}{\sqrt{2}(r_B + r_O)}, \tag{1}$$

where r_A and r_B are the mean radii of the ions occupying the A-sites and B-sites, respectively, and r_O is the ionic radius of oxygen. For the ideal cubic perovskite $t^* = 1$. This criterion is fulfilled if the radius of the A-site cation equals that of oxygen (0.140 nm) and the radius of the B-site cation is equal to $(\sqrt{2}-1)r_O = 0.058\,\text{nm}$. If t^* differs slightly from unity the atoms are displaced from their ideal positions to minimize the free energy and a distorted perovskite structure is formed. Stable perovskites may be obtained in oxides for which $0.89 \lesssim t^* \lesssim 1.02$. Larger deviations from unity will lead to a different structure, e.g. ilmenite for $t^* < 1$ and calcite for $t^* > 1$ (Jonker and van Santen, 1950).

Table 1 shows ionic radii used for calculation of tolerance factors of lanthanum manganites doped with Ca, Sr, or both. In distorted perovskite structures the coordination number for the A-site may differ from the ideal twelve. The table also includes ionic radii for nine-fold oxygen coordination of the A-site ions.

Table 1. Ionic radii in (Ca,Sr)-doped lanthanum manganite perovskites (in nm). The A-site cation radii are given for twelve-fold and nine-fold oxygen coordination (separated by comma), while the B-site cation radii are given for six-fold oxygen coordination. Source: Shannon (1976).

A-site		**B-site**		**O-site**	
La^{3+}	0.136, 0.1216	Mn^{4+}	0.053	O^{2-}	0.140
Ca^{2+}	0.134, 0.118	Mn^{3+}	0.0645		
Sr^{2+}	0.144, 0.131				

The basic material of the lanthanum manganite family, $LaMnO_3$, has an orthorhombic, so-called O′-type, perovskite structure (at ambient conditions), which apart from the buckling of the network of MnO_6 octahedra arising from the misfit in ionic sizes ($t^* = 0.95$), incorporates a severe distortion of the MnO_6 octahedra due to the Jahn-Teller effect of Mn^{3+} (see e.g. Coey *et al*. (1999)).

Doped lanthanum manganites have other kinds of distorted perovskite structures depending on the nature of the dopant, the degree of doping, temperature, etc. For $La_{1-x}Ca_xMnO_3$, the O′-type orthorhombic structure of the parent material is gradually replaced by another orthorhombic structure, called O-type, which does not involve Jahn-Teller distortion. At $x = 0.4$ an additional phase transformation involving a not uniquely defined T phase occurs (Nagaev, 1996). Strontium-doped lanthanum manganite, $La_{1-x}Sr_xMnO_3$, shows a transition from O′-type to O-type orthorhombic symmetry around $x \approx 0.1$, but for $x \leq 0.175$ it forms a rhombohedral structure (again considering ambient temperatures) (Urushibara *et al*., 1995; Yamada *et al*., 1996). Apart from compositional variation phase transformations may be induced by changing the temperature, or, in some cases, by applying an external field. The latter has been observed for $La_{1-x}Sr_xMnO_3$ with $x = 0.17$ (Asamitsu *et al*., 1996). The structural phase transformations in $La_{1-x}Ca_xMnO_3$ and $La_{1-x}Sr_xMnO_3$ are usually accompanied by changes of the magnetic and electronic phases. Combined structural, magnetic, and electronic phase diagrams for the two lanthanum manganite series are shown later in Figure 6.

2.4 Magnetic and electronic properties

A fundamental characteristic of mixed-valence manganites is the close relationship between electronic transport and magnetism. A key feature is the simultaneous transition from antiferromagnetic and insulating properties to ferromagnetic and conducting properties induced by A-site substitution. The basic theory for this phenomenon was established by Zener (1951a, 1951b), who introduced the concept of double-exchange – the spin-dependent transfer of an electron from a Mn^{3+} ion to a neighboring Mn^{4+} ion via the interstitial O^{2-} ion. The theory was later refined by Anderson and Hasegawa (1953) and by de Gennes (1960). An extensive review of the theories for the special electronic and magnetic properties of mixed-valence manganites can be found in Coey *et al*. (1999). A brief summary follows below.

The magnetic and electronic properties of lanthanum manganites, $La_{1-x}A_xMnO_3$ (A = Ca, Sr, …) are strongly related to the simultaneous presence of manganese in different valence states. The end-members, $x = 0$ and $x = 1$, containing Mn in only one valence state (for divalent A-site substitution either 3+ or 4+, respectively), are usually antiferromagnetic insulators, but intermediate compositions, which have mixed Mn valence, may be ferromagnetic and have good conducting properties. The electronically active orbitals are the manganese d orbitals. The ground state electronic configuration of trivalent and quadrivalent Mn is $3d^4$ and $3d^3$, respectively. The five d orbitals, each of which can accommodate one spin-up and one spin-down electron, are split by the octahedral crystal field originating from the six oxygen ions surrounding the Mn ion (cf. Figure 1). The crystal splitting groups the d orbitals into three-fold degenerate low-energy t_{2g} orbitals (d_{xy}, d_{yz}, and d_{zx}) and two high-energy e_g orbitals ($d_{x^2-y^2}$ and $d_{z^2-r^2}$). The splitting, which is on the order of 1.5 eV (Coey *et al*., 1995) is not large enough to cause low-spin states; the electrons occupy the orbitals with maximum spin in accordance with the first Hund rule (see Figure 2). Hence, the electronic configuration of Mn^{3+} is $t_{2g}^{3\uparrow}e_g^{\uparrow}$, while Mn^{4+}

have the configuration $t_{2g}^{3\uparrow}$. Mn^{3+} is known to be a strong Jahn-Teller ion in octahedral sites, i.e. it can benefit energetically from a distortion of the oxygen octahedron (see e.g. Yosida (1996)). Figure 2 illustrates the Jahn-Teller splitting arising from a tetragonal elongation of the octahedron. The energy of Mn^{3+} is lowered by about 0.6 eV (Coey *et al*., 1999), while Mn^{4+} gains nothing from distortion of the oxygen octahedron.

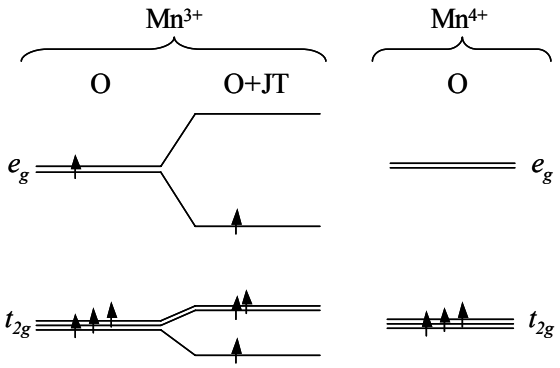

Figure 2. One-electron electronic structure of Mn^{3+} and Mn^{4+} in octahedral coordination. For Mn^{3+} the electronic structure is shown before and after Jahn-Teller distortion (O and O+JT, respectively.

As illustrated in Figure 3 the t_{2g} orbitals have their lobes oriented between the oxygen neighbors. Therefore the three t_{2g} electrons of Mn^{3+} and Mn^{4+} tend to form a localized core with net spin 3/2. The e_g orbital, however, overlap strongly with the *p* orbital of the oxygen neighbor to form a σ^* antibonding band.

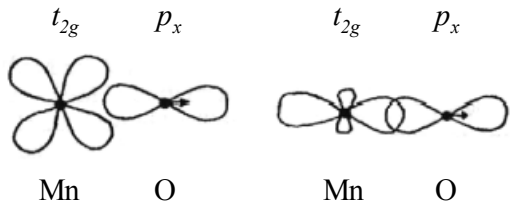

Figure 3. Illustration of orbital overlaps between Mn t_{2g} and Mn e_g orbitals with a p orbital of a neighboring O ion.

For $x = 0$ end-member $LaMnO_3$ the Fermi level falls in the gap between the two Jahn-Teller e_g bands explaining why the material is insulating although it has a partially filled *d*-band. When *x* is increased, e.g. by substituting a number of La^{3+} ions with Ca^{2+} or Sr^{2+}, the σ^* band becomes partially filled (the divalent substitution serves as hole doping). The σ^* electrons can travel from a Mn^{3+} site to an adjacent Mn^{4+} site via the interstitial O^{2-} ion and the material may become conducting. The exchange coupling associated with electron transfer between Mn^{3+} and Mn^{4+}, which is called double exchange, can be evaluated describing the Mn pair as two fixed Mn^{4+} ion cores 1 and 2 both with spin $S = S_1 = S_2 = 3/2$ and a mobile electron with spin $s = 1/2$ (see also Figure 4). The double exchange Hamiltonian can be written in block form (Anderson and Hasegawa, 1953; Coey *et al*., 1999)

$$\begin{bmatrix} -J_H \mathbf{S}_1 \cdot \mathbf{s} & t_0 \mathbf{I} \\ t_0 \mathbf{I} & -J_H \mathbf{S}_2 \cdot \mathbf{s} \end{bmatrix}, \tag{2}$$

where J_H is the on-site Hund rule coupling. The diagonal elements correspond to energy states of the electron and an Mn^{4+} ion core at site 1 and 2, respectively. The off-diagonal elements take into account the transfer between site 1 and site 2, t_0 is the normal transfer integral (depending on the spatial wavefunctions), and **I** is the 2×2 unit matrix. The diagonalization procedure will not be carried out here. It turns out that for $J_H >> t_0$ there are two low-energy solutions to the secular equation:

$$E = -\frac{J_H S}{2} \pm t_0 \cos\left(\frac{\theta}{2}\right), \tag{3}$$

where θ is the angle between the two Mn^{4+} core spins. As can be seen, the ground state energy of this system is lowest if the neighboring core spins are parallel. Thus, the double exchange coupling leads to ferromagnetism, and the effective transfer integral can be written

$$t = t_0 \cos\left(\frac{\theta}{2}\right). \tag{4}$$

The double exchange model is based on the assumption that electron transfer takes place with spin memory, and the transfer integral t_0 depends on the angle between the adjacent core spins. An electron traveling from a Mn^{4+} core with one spin direction to another Mn^{4+} core with a different spin direction causes a violation of Hund's first rule and energy is required to align the spins on the Mn site, where the electron arrives.

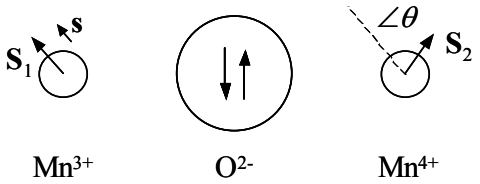

Figure 4. Schematic illustration of the double exchange mechanism – the transfer of a mobile electron between two adjacent Mn^{4+} sites. The transfer is possible because of the hybridization between the e_g orbitals of the Mn ions with the p orbitals of the interstitial oxygen ion.

Since the electron transfer is related to the angle between neighboring magnetic moments, the double exchange model explains why mixed-valence manganites show a close relationship between transport properties and magnetism. As mentioned in Section 2.2 above the amount of Mn^{4+} present in a mixed-valence manganite such as $La_{1-x}Ca_xMnO_3$ is determined by x. Figure 5 shows the low-temperature ferromagnetic moment and electrical conductivity of $La_{1-x}Ca_xMnO_3$ as a function of x (or equivalently the Mn^{4+} content). For $x = 0$ the material is antiferromagnetic and shows a low conductivity, but as x is increased and double exchange becomes dominant, the ferromagnetic moment as well the conductivity increases. Maximum values are observed around $x = 0.33$, where the ferromagnetic moment approaches the theoretical spin-only value for a ferromagnetic mixture of Mn^{3+} and Mn^{4+} (calculated as $(1-x)4\mu_B + x3\mu_B$, where μ_B is the Bohr mag-

neton). Upon a further increase of x the ferromagnetic moment and the conductivity start to decrease. This is due to the direct overlap between the manganese t_{2g} orbitals, which leads to antiparallel exchange coupling because only the spin-down states are empty (Goodenough, 1955). In the range $0.33 < x < 0.5$ there is a competition between the ferromagnetic Mn^{3+}–Mn^{4+} double exchange coupling and the antiferromagnetic Mn^{4+}–Mn^{4+} coupling. At $x = 0.5$ antiferromagnetism becomes dominant. The conductivity is once again low.

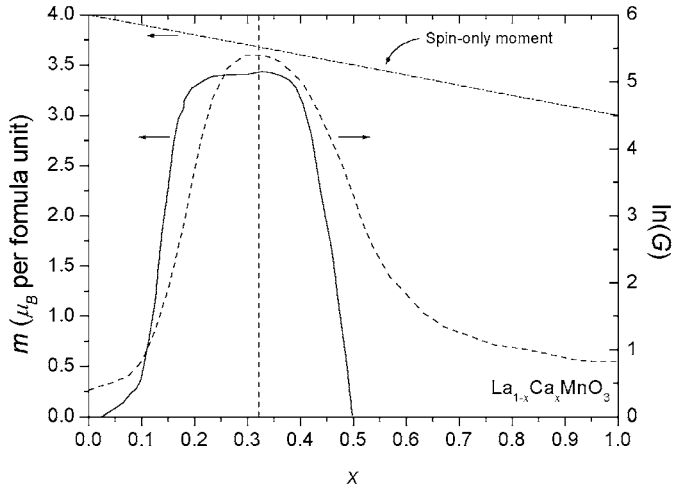

Figure 5. Low-temperature ferromagnetic moment (given in Bohr magnetons per formula unit) and conductivity at 80K (a. u.) of $La_{1-x}Ca_xMnO_3$ as a function of the substitution factor x. The theoretical spin-only moment corresponding to a mixture of Mn3+ and Mn3+ is shown (straight line). Adapted from Coey et al. (1999).

2.5 Summary

Mixed-valence manganites are complex materials showing a rich variety of structural, magnetic and electronic phases. Phase transitions may be induced by changing the composition, changing the temperature, or sometimes by applying an external magnetic field. Usually structural, magnetic, and electronic phase transitions occur simultaneously. Figure 6 shows combined structural, magnetic and electronic phase diagrams of $La_{1-x}Ca_xMnO_3$ and $La_{1-x}Sr_xMnO_3$. With regard to magnetic and conducting properties the optimum composition of both Ca- and Sr-doped lanthanum manganite is given by $x = 0.33$. This is one reason why $La_{0.67}Ca_{0.33}MnO_3$ and $La_{0.67}Sr_{0.33}MnO_3$ were chosen as parent materials for the present study. The investigation regarded phenomena, which are usually expected to show a maximum close to the ferromagnetic transition, namely magnetocaloric effect and colossal magnetoresistance. The phase diagram of $La_{1-x}Ca_xMnO_3$ shows that the Curie temperature of $La_{0.67}Ca_{0.33}MnO_3$ is about 260 K. For $La_{0.67}Sr_{0.33}MnO_3$ T_C is about 370 K. This was another reason for choosing these materials. It was anticipated that by preparing solid solutions between these compounds it would be possible to tailor materials with a ferromagnetic transition temperature close to room temperature thus having optimum magnetic and electrical properties at ambient conditions.

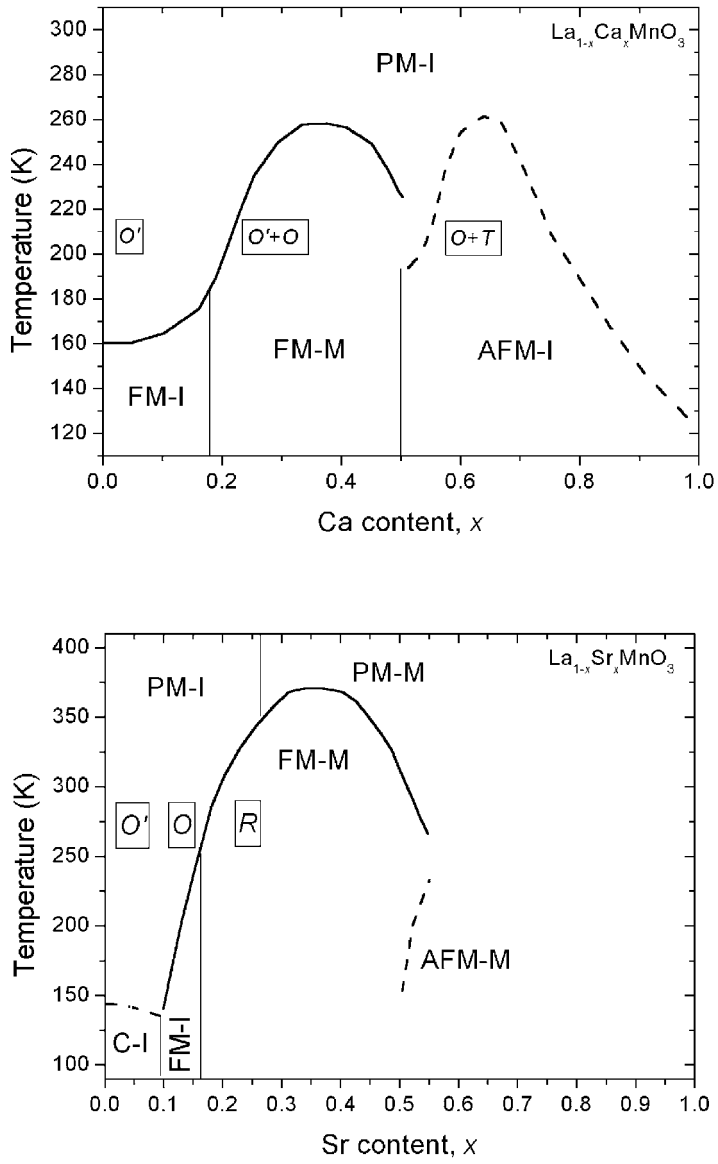

Figure 6. Magnetic and electronic phase diagrams of $La_{1-x}Ca_xMnO_3$ (top plate) and $La_{1-x}Sr_xMnO_3$ (bottom plate). Magnetic and electronic regions are indicated as follows: PM-I = paramagnetic insulator, PM-M: paramagnetic metal, FM-I = ferromagnetic insulator, FMM = ferromagnetic metal, AFM-M: antiferromagnetic metal, and C-I: spin-canted insulator. Symbols in boxes refer to structural phases (defined in the text). Top plate adapted from Coey et al. (1999), Schiffer et al. (1995), Nagaev (1996). Bottom plate adapted from Urushibara et al. (1995), and Tokura and Tomioka (1999).

3 Preparation of $La_{0.67}Ca_{0.33-x}Sr_xMnO_3$ samples

3.1 Introduction

Lanthanum manganites (and manganites in general) can be prepared by many different synthesis techniques and in various forms, including single crystals, polycrystalline ceramics and thick or thin films. Single crystals can be grown in several ways, for instance by the floating-zone method (Urushibara et al., 1995). Polycrystalline samples can be prepared by solid state mixing, involving repeated steps of mixing, grinding and heating of oxides until a single-phase manganite is obtained. Polycrystalline manganites can also be synthesized by various wet-chemical methods (Mori *et al*., 2000; Philip and Kutty, 2000). Thick manganite films can be produced by spraying techniques and well-defined 2D-patterns can be obtained using screen printing techniques (Balcells *et al*., 2000). Thin films are usually grown by laser ablation (pulsed laser deposition) or sputtering using sintered polycrystalline targets (Prellier *et al*., 2001). Depending on the substrate, thin films can be prepared in epitaxial as well as polycrystalline forms (Gupta *et al*., 1996).

The Ca- and Sr-doped lanthanum manganite samples under investigation in the present work were polycrystalline ceramics prepared by the so-called glycine-nitrate combustion technique (Chick *et al*., 1990). This chapter gives a detailed description of the sample preparation, followed by a discussion on sample composition and morphology.

3.2 Target compositions and sample designation

A series of lanthanum-calcium-strontium manganites with the general composition $La_{0.67}Ca_{0.33-x}Sr_xMnO_3$ were prepared for this investigation. The formula indicates that the manganites should be considered as Sr substituted La–Ca manganites. This is unintended since they could equally well be regarded as Ca substituted La–Sr manganites, or, more generally, as solid solutions between the end-members, $La_{0.67}Ca_{0.33}MnO_3$ and $La_{0.67}Sr_{0.33}MnO_3$.

The $La_{0.67}Ca_{0.33-x}Sr_xMnO_3$ series consisted of seven samples with target compositions given by x = 0, 0.055, 0.110, 0.165, 0.220, 0.275, and 0.33, corresponding to Ca/Sr ratios of 100:0, 83.3:16.7, 66.7:33.3, 50:50, 33.3:66.7, 16.7:83.3, and 0:100, respectively. Thus, the variation of x corresponded to an equidistant exchange of Ca and Sr.

Both complete formulas and abbreviated sample notation will be used throughout the following. For example, the sample with x = 0.110 will be written $La_{0.67}Ca_{0.220}Sr_{0.110}MnO_3$, or sometimes designated the x = 0.110 sample. The compositions corresponding to x = 0 and x = 0.33 will often be referred to as the end-members of the series.

3.3 Glycine-nitrate combustion synthesis

The glycine-nitrate combustion method is a chemical method, producing a finegrained powder. It was introduced by Chick *et al*. (1990) and suggested for preparation of various compounds such as manganites, chromites, zirconates, ferrites and oxide superconductors.

The sample synthesis started with the preparation of aqueous nitrate solutions; one for each element of the final oxide product. In the present case this involved the metal nitrates $La(NO_3)_3{\cdot}6H_2O$, $Ca(NO_3)_2{\cdot}H_2O$, $Sr(NO_3)_2{\cdot}H_2O$, and $Mn(NO_3)_2{\cdot}4H_2O$ (all of them

pro analysis grade). Each of these salts was dissolved in deionized water, aiming at a concentration of about 0.1 kg metal per kg solution. The exact concentration of metal was determined graviometrically, following formation of oxide from the nitrate solutions by heating at 580 K for five hours. To improve accuracy, the graviometric analysis was carried out in triplicate.

Having the metal nitrate stock solutions of known concentration at hand, the glycine-nitrate combustion synthesis was carried out as follows. Metal nitrate solutions were mixed in appropriate proportions depending on the target composition in a large beaker. Glycine (H_2NCH_2COOH) was added in granular form in an amount corresponding to a glycine/nitrate ratio of approximately 0.6. The solution was stirred using a magnetic stirrer until the glycine was completely dissolved. The purpose of adding glycine is described briefly below. The beaker was placed on a hot plate and the solution was allowed to boil. When excess water had been removed, a viscous liquid remained. After a short while the liquid began to swell and turned into viscous foam. Eventually, the solution spontaneously self-ignited and an ultra-fine grained powder was produced. The combustion reaction was quite vigorous and in order not lose the powder to ventilation system of the fume cupboard, a "smokestack" covered by a stainless steel sieve was placed above the beaker containing the solution. To obtain a well-crystallized single-phase oxide product, the collected powder was calcined (i.e. heat-treated) in air for five hours at 1375 K (more information on the crystallographic properties follows in the next chapter). The calcination caused a weak aggregation and subsequently the samples were ground by hand in a mortar. Finally, a few grams of the calcined powder were pressed into a bar ($\sim 5\times5\times20 mm^3$), which was sintered in air for five hours at 1775 K. The sintered bar constituted the final sample, now consisting of a solid piece of material. The synthesis procedure, which is summarized in Figure 7, was carried out for each of the seven target compositions mentioned above.

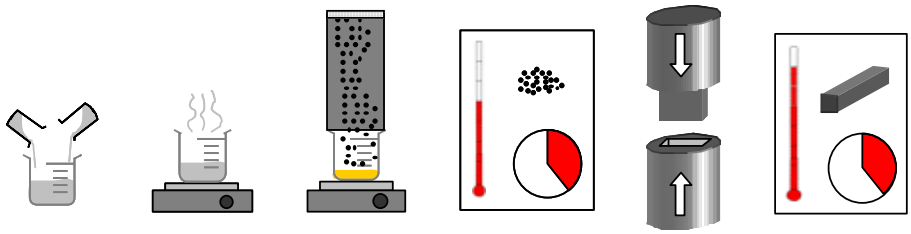

Figure 7. Step-by-step illustration of the glycine-nitrate synthesis procedure: i) Mixing of metal nitrate solutions with glycine. ii) Removal of water by boiling. iii) Glycine-nitrate combustion and collection of oxide powder. iv) Calcination in air at 1375K for five hours. v) Powder pressing. vi) Sintering in air at 1775K for five hours.

3.3.1 The purpose of glycine

The glycine plays a dual role in the glycine-nitrate process. Glycine, H_2NCH_2COOH, is an amino acid with a carboxylic acid group (COOH) at one end and an amine group (H_2N) at the other. Both groups have the ability of forming complexes with the metal cations in the solution (La^{3+}, Sr^{2+}, etc.). The complexation improves the solubility of the metal cations and prevents selective precipitation during the removal of water by boiling. The metal ions are kept in solution and randomly distributed until the point of ignition and oxide formation. This gives an oxide with great compositional uniformity. In addi-

tion to the complexation, glycine serves as a fuel for the combustion reaction. The combustion is driven by the oxidation of glycine by the nitrate ions.

3.4 Elemental analysis

The elemental composition and homogeneity of the $La_{0.67}Ca_{0.33-x}Sr_xMnO_3$ samples were investigated by means of quantitative energy dispersive x-ray spectroscopy (EDS) using a JEOL-840 scanning electron microscope equipped with an x-ray detector. For composition detection the microscope was operated at 12 kV.

Figure 8 shows a typical EDS spectrum of the $La_{0.67}Sr_{0.33}MnO_3$ sample. The spectrum contains characteristic peaks of La, Ca, Sr, Mn, O, and C. The C peak is probably due to the carbon paste used for mounting of the sample. For some samples, a small amount of Al was detected. This was ascribed to the corundum used for polishing of the samples carried out prior to the EDS analysis.

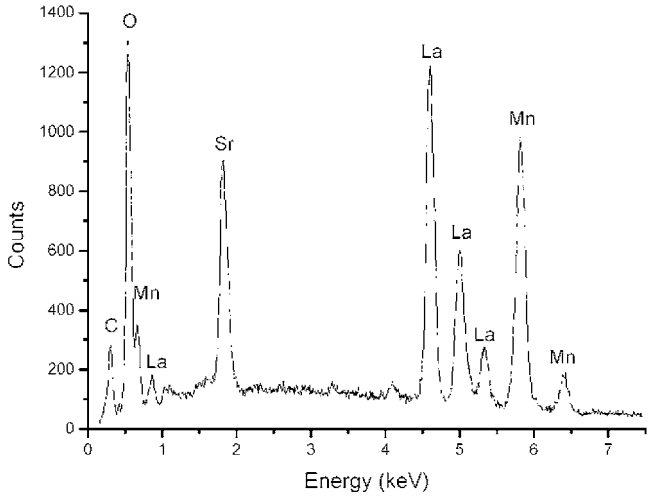

Figure 8. EDS spectrum of an $La_{0.67}Sr_{0.33}MnO_3$ sample. Characteristic peaks are labeled by corresponding elements.

Figure 9 shows the relative amounts of La, Ca, Sr, and Mn in the seven samples; based on average values obtained from about 5 to 10 EDS spectra recorded at selected surface areas (typically 50×50 μm^2). The oxygen contents, which could not be determined properly from the spectra (see discussion below), were fixed at 60 % in accordance with the target composition, $La_{0.67}Ca_{0.33-x}Sr_xMnO_3$.

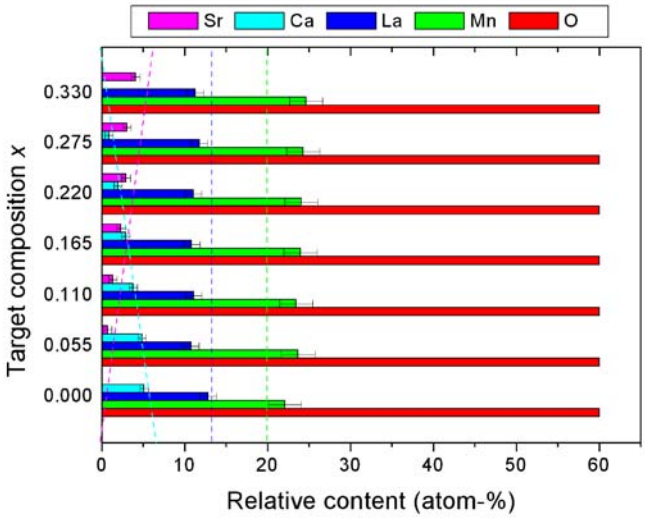

Figure 9. Elemental composition of the $La_{0.67}Ca_{0.33-x}Sr_xMnO_3$ samples measured by means of energy dispersive x-ray spectroscopy. The horizontal columns indicate the average relative amounts of La, Sr, Ca, and Mn based on averages obtained from 5–10 EDS measurements. The oxygen contents were fixed at 60 %. The dashed lines indicate expected (target) amounts of La, Ca, Sr, and Mn (the color code is indicated in the legend).

In general, the measured sample compositions were in quite good agreement with the target compositions. The samples show an excess content of Mn (expected to be 20 %) and a lack of La (with target value 13.4 %). The Ca and Sr contents are also somewhat too low compared to the expected values. However, the analysis shows very clearly that Ca and Sr are exchanged in an approximately linear manner, as intended (cf. Section 3.2). Sample homogeneity was examined by comparing EDS spectra obtained for areas with spectra obtained when the electron beam was focused on single spots. The ions appeared to be uniformly distributed in all the samples.

The disagreement between observed and expected compositions could be an instrumental issue. In fact, the EDS technique is not very well suited for porous specimens like the $La_{0.67}Ca_{0.33-x}Sr_xMnO_3$ samples (Bilde-Sørensen, 2002). First, the x-ray lines of oxygen occur close to the detection limit of the EDS detector, for which reason the analysis does not provide precise information on oxygen stoichiometry (this explains why the oxygen contents were fixed at 60 % above). Second, due to scattering effects, porosities may influence on the x-ray peak intensities of the various elements in the sample, and thus on the relative distribution of elements obtained from the EDS spectra. As can be seen in Section 3.5 below, the $La_{0.67}Ca_{0.33-x}Sr_xMnO_3$ samples were quite porous. Accordingly, the best agreement between measured and target compositions were obtained for the $La_{0.67}Ca_{0.33}MnO_3$ sample, which is the least porous of the seven samples.

Since the oxygen stoichiometry has not been determined properly it would perhaps be more correct to use the formula $La_{0.67}Ca_{0.33-x}Sr_xMnO_{3\pm\delta}$ for the manganite compounds. However, bearing this in mind, the slightly simpler notating not involving $\pm\delta$ will be used in the following.

3.5 Grain size and morphology

The grain size and surface morphology of the $La_{0.67}Ca_{0.33-x}Sr_xMnO_3$ series were investigated by scanning electron microscopy (SEM) utilizing a JEOL-840 microscope operated at an acceleration voltage of 15 kV.

Figure 10 shows surface electron micrographs of selected $La_{0.67}Ca_{0.33-x}Sr_xMnO_3$ samples. The variation in composition causes significant morphological changes. The $La_{0.67}Ca_{0.33}MnO_3$ sample consists of highly aggregated grains and appears to have almost no porosities. The closely packed grains occur in different polygonal forms. When the Sr content is increased at the expense of Ca, the grain size decreases. In such a case the morphology of the grain interfaces become neck-like. Apparently, the samples become more porous.

A computer based SEM image analysis was carried out to estimate the grain size of the samples. For each sample, the size of about 100 grains (chosen at random) was measured. The size of a grain was defined as the mean diagonal of a polygon drawn along the edges of the grain. Figure 11 shows the size distribution of the $La_{0.67}Ca_{0.33}MnO_3$ sample obtained this way. A gaussian fit was applied to determine the mean grain size (the center of the distribution). The inset of the figure illustrates the polygonization of a single grain. The size of the grain was determined as the average length of the two diagonals.

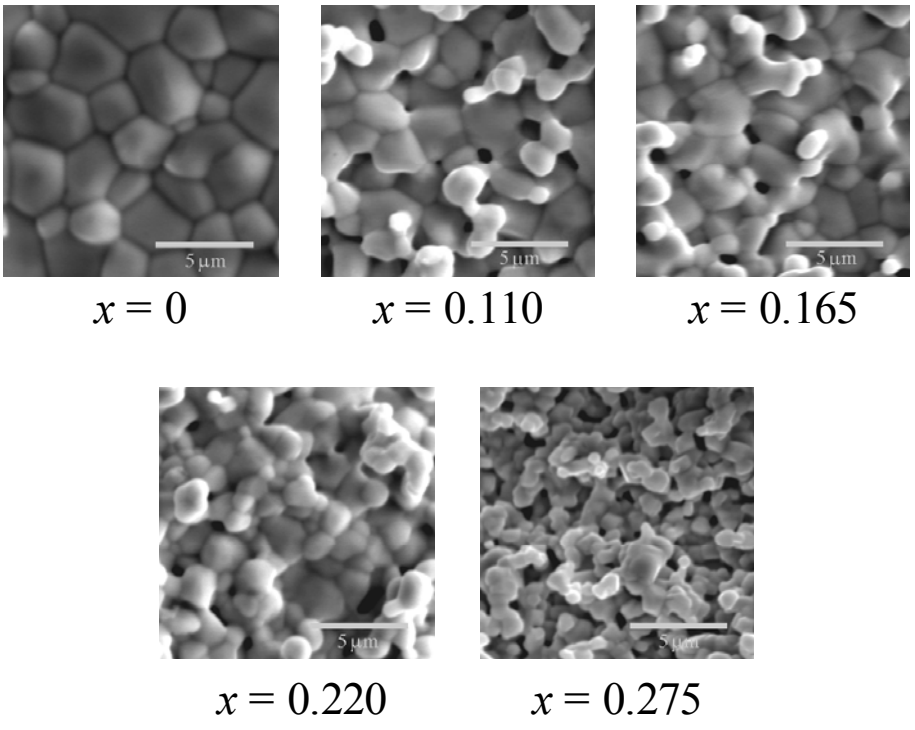

Figure 10. Surface electron micrographs of five selected $La_{0.67}Ca_{0.33-x}Sr_xMnO_3$ samples. The scale bars correspond to 5 µm (the images are scaled equally).

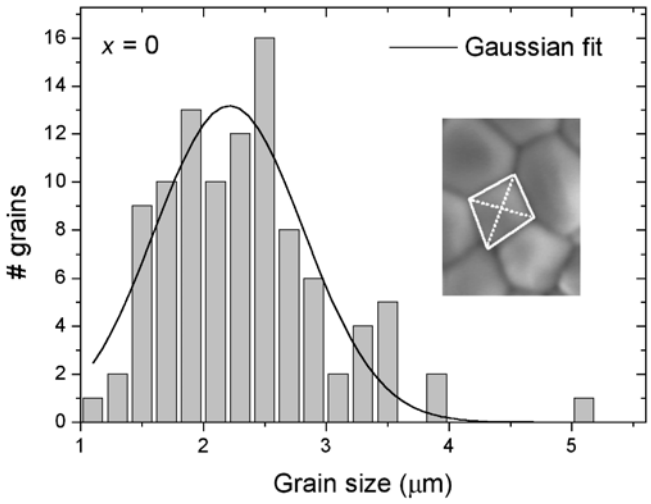

Figure 11. Grain size distributions of $La_{0.67}Ca_{0.33}MnO_3$ based on 100 grains. The solid line represents a least-squares-fitted gaussian. The inset illustrates how a single grain was polygonized. The size of the grain was determined as the average length of the two diagonals (dotted lines).

The result of the grain size analysis is summarized in Figure 12 showing the mean grain size against *x*. The error bars indicate the FWHM of the gaussian size distributions. Considering the very simple method used for the grain size measurements, a surprisingly robust linear relationship between the Ca–Sr ratio (given by *x*) and the mean grain size is observed. It is evident that Sr tends to hinder grain growth and aggregation. This can be attributed to the reduced diffusion rate associated with the exchange of Ca ions with the more than twice as heavy Sr ions (see also Mori *et al*. (2000)).

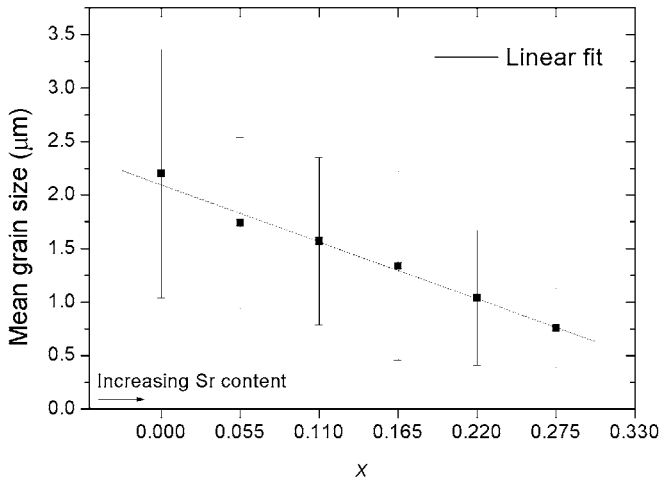

Figure 12. Mean grain size of the $La_{0.67}Ca_{0.33-x}Sr_xMnO_3$ samples as a function of x. The error bars indicate the FWHM of the corresponding grain size distributions. The solid line represents a linear least-squares fit to the data.

3.6 Summary

Ceramic $La_{0.67}Ca_{0.33-x}Sr_xMnO_3$ powders with nominal compositions x = 0, 0.055, 0.110, 0.165, 0.220, 0.275, and 0.33, respectively, were prepared by the glycine-nitrate combustion technique. The variation of x corresponds to an equidistant exchange of the A-site cations Ca and Sr. The oxide powders were pressed into bars and sintered at 1775 K for five hours in air. Energy dispersive spectroscopy showed that the samples were composed approximately according to the target compositions given by the x values listed above. The samples showed high compositional uniformity. Only an insignificant amount of impurity elements was detected. The sample morphology was influenced by the variation of the Ca/Sr ratio. Upon increased Sr content, the grain size decreased and the samples became more porous.

4 Structural and magnetic properties of the $La_{0.67}Ca_{0.33-x}Sr_xMnO_3$ series

4.1 Introduction

This chapter presents results on the crystallographic and magnetic properties of the $La_{0.67}Ca_{0.33-x}Sr_xMnO_3$ series. The crystallographic properties were investigated by means of x-ray diffraction, and Rietveld refinement was used to extract detailed information on the structural changes associated with the variation of the Ca/Sr ratio. Combined with magnetization data a strong relationship between structure and magnetism in the $La_{0.67}Ca_{0.33-x}Sr_xMnO_3$ system is documented. Possible explanations for this relationship will be discussed.

4.2 Experimental procedures

The structural characterization of the $La_{0.67}Ca_{0.33-x}Sr_xMnO_3$ series was carried out by x-ray diffraction (XRD) using a STOE&CIE powder diffractometer with Bragg-Brentano geometry and CuKα radiation. Scanning was performed at angles between $2\theta = 20°$ and 90° in steps of 0.05 degrees. Integration time was 30 s per step, providing a good counting statistics. In preparation for the XRD measurements, a small piece of each sample was crushed using a mortar and high-purity silicon was added as internal standard for correction of peak positions. The composition of the $La_{0.67}Ca_{0.33-x}Sr_xMnO_3$ series with 33 % hole doping was expected to lead to ferromagnetic compounds (cf. Section 2.4). This was confirmed by measuring the temperature dependence of the magnetization. All samples in the series showed smooth paramagnetic-to-ferromagnetic transitions. Magnetization measurements were carried out using a non-commercial 69 Hz vibrating-sample magnetometer (VSM).

4.3 Structural characterization

Figure 13 (a) shows x-ray diffraction patterns of the $La_{0.67}Ca_{0.33-x}Sr_xMnO_3$ samples mixed with silicon. All diffractograms were obtained at room temperature. Due to the slightly different relative amounts of Si added to the samples the Si peak intensities vary. The Si peaks occur at angles very close to the expected ones (e.g. $2\theta = 28.443°$ for the intense 111 reflection) and only minor peak position corrections were required. At first, the diffraction patterns appear to be very similar. However, from the enlarged view of the $2\theta = 32°–33.5°$ region, shown in Figure 13 (b), it is clear that the compositional variation causes significant structural changes. As x is increased, the intense diffraction peak observed for the $La_{0.67}Ca_{0.33}MnO_3$ sample ($x = 0$) gradually splits up into two peaks. The transformation seems to be complete for the $x = 0.165$ sample. Upon a further increase of x, the doublet is shifted slightly towards lower reflection angles. Corresponding gradual changes of the XRD lines can be observed at other reflection angles.

By XRD indexation the samples were shown to be well-crystallized perovskite oxides containing no impurity phases. The fitted line positions of the samples with low values of x, i.e. with no splitting of the main reflection, suggested an orthorhombic perovskite unit cell. This structure has an intense 112 reflection at about $2\theta = 32.8°$ flanked by two weaker reflections, 200 and 020, respectively. The superposition of the three diffraction peaks appears as a single line in the observed x-ray pattern. For the samples with $x \gtrsim 0.165$, the XRD patterns were found to correspond to a perovskite unit cell with

rhombohedral symmetry. This structure have two intense reflections around $2\theta = 32.6°$, 110 and 104, respectively. The partially overlapping reflections are separated by about $\Delta(2\theta) = 0.2°$ and appear as a doublet. Thus, this preliminary analysis indicated that the gradual change of the XRD patterns, induced by increasing the amount of Sr at the expense of Ca, was associated with an orthorhombic-to-rhombohedral phase transition. This conclusion is, of course, only valid for room temperature. The x-ray analysis did not provide any information on a possible temperature dependence on the structural properties of the samples.

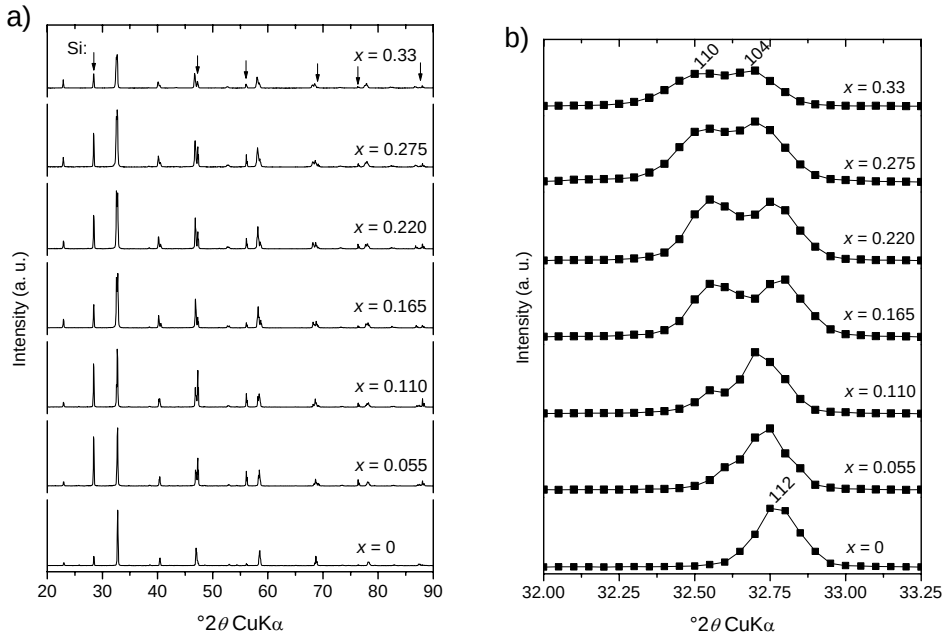

Figure 13. a) X-ray diffraction patterns of $La_{0.67}Ca_{0.33-x}Sr_xMnO_3$ samples mixed with Si. Curves are labeled by corresponding x values. Diffraction peaks of Si are marked by arrows (in the diffractogram of the x = 0.330 sample). b) Enlarged view of the diffraction angle range 2θ = 32–33.5°.

4.3.1 Rietveld analysis

To give a more detailed description of the structural changes caused by the exchange of Ca and Sr, a Rietveld refinement analysis (Rietveld, 1967; Rietveld, 1969) was adopted. This method is far more complex than basic indexation. It provides a complete structural model and a fit of the entire diffractogram, including line positions, line widths and relative line intensities. A Rietveld model employs lattice parameters, atomic positions, occupation factors, thermal parameters, etc. A thorough introduction to the Rietveld refinement method can be found in Young (1995). Appendix A gives a brief introduction and is intended for readers not familiar with the technique. The Rietveld analysis was carried out using the computer program Rietica (Hunter, 1997).

Structural model

Establishing a Rietveld model from scratch can be a tedious task. One must provide an initial set of structural parameters (space group, lattice constants, atom types, atomic positions, etc.), which results in a calculated x-ray pattern in fairly good agreement with the observed x-ray pattern. Otherwise the minimization algorithm will probably diverge and the result will be of no physical relevance. Fortunately, suggestions for initial parameter

values for the two end-members of the $La_{0.67}Ca_{0.33-x}Sr_xMnO_3$ series could be obtained from the literature (Guo *et al*., 2000; Guo *et al*., 2000; Dai *et al*., 1996) and are used with appropriate modifications. The previous investigations suggest to use the space group Pbnm with $Z = 4$ for $La_{0.67}Ca_{0.33}MnO_3$ and the space group $R\bar{3}c$ with $Z = 6$ for $La_{0.67}Sr_{0.33}MnO_3$ (Z is the number of formula units per unit cell) These space groups represent orthorhombic and rhombohedral symmetry, respectively. Each space group has a number of equivalent crystal positions – the so-called Wyckoff positions. When setting up a Rietveld model, the available atoms or ions must be distributed among these positions. Table 2 gives an overview of the equivalent crystallographic positions and the corresponding relative crystal coordinates of the Pbnm and $R\bar{3}c$ space groups. The table also lists the atomic site occupation corresponding to the nominal compositions of the $La_{0.67}Ca_{0.33-x}Sr_xMnO_3$ compounds. For the Pbnm space group, one third of the oxygen ions were placed at 4*c* sites and the remaining oxygen ions at 8*e* sites. In the following, the notation O^{2-I} and O^{2-II} are used to distinguish these ions.

Table 2. An overview of equivalent crystallographic positions (given in Wyckoff notation) of the space groups Pbnm and $R\bar{3}c$, with corresponding coordinates and the atomic occupation factors used for refinement of the $La_{0.67}Ca_{0.33-x}Sr_xMnO_3$ series.

Space group	Z	Position	Coordinates	Atomic occupation
Pbnm (no. 62,3)	4	4*a*	(0,0,0)	$2.667Mn^{3+}$ and $1.333Mn^{4+}$
		4*c*	(*x*,*y*,0.25)	$2.667La^{3+}$, $(1.333 - 4x)Ca^{2+}$
				$4xSr^{2+}$ and $4O^{2-I}$
		8*d*	(*x*,*y*,*z*)	$8O^{2-II}$
$R\bar{3}c$ (No. 167)	6	6*b*	(0,0,0)	$2.667Mn^{3+}$ and $1.333Mn^{4+}$
		6*a*	(0,0,0.25)	$4La^{3+}$, $(2 - 6x)Ca^{2+}$ and $6xSr^{2+}$
		18*e*	(*x*,0,0.25)	$18O^{2-}$

Fitting procedure

As mentioned above, the x-ray patterns of the end-members were refined using initial parameters obtained from the literature. Acceptable fits with low deviations were obtained, confirming that the structural model were applicable to the $La_{0.67}Ca_{0.33-x}Sr_xMnO_3$ system. The new sets of parameters derived this way were then used as initial guesses for the remaining samples. The refinements were carried out from both ends of the composition range in a trial-and-error manner as illustrated in Figure 14.

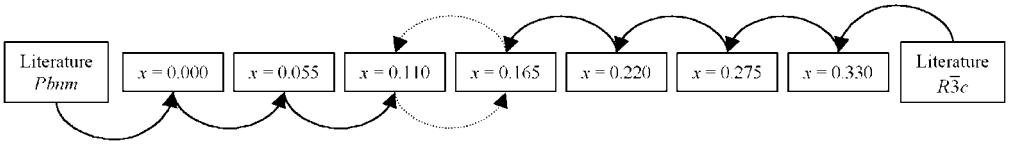

Figure 14. Schematic illustration of the procedure used for Rietveld refinement of x-ray patterns of $La_{0.67}Ca_{0.33-x}Sr_xMnO_3$ samples. Initial sets of Rietveld parameters obtained from literature were applied to the end-members. The new refined parameter sets were then used as initial guesses for the next members of the composition range. Solid arrows

indicate successful refinements. Dashed arrows indicate unstable refinements leading to improper fits.

In order to track the crystallographic changes caused by the Ca/Sr exchange, selected parameters, such as lattice constants and atomic positions, were allowed to vary during refinement. To ease the interpretation as many parameters as possible were kept fixed. Table 3 lists the most important Rietveld parameters and gives an idea of the degree of freedom associated with the refinements.

Table 3. An overview of the most important parameters of the Rietveld model and an indication whether they were fixed or allowed to vary during refinement. Symbols are explained in Appendix A.

Parameter group	Parameter	Fixed or free
Structural	Space group	Fixed
	Z	Fixed
	α, β, γ	Fixed
	a, b, c	Free
Atomic	Atom types	Fixed
	Atomic positions	Both fixed and free
	Site occupation	Fixed
	Temperature factor	Fixed
Experimental	Wavelength	Fixed
	Zero point	Fixed
Peak shape	U, V, W	Free
	$\gamma_1, \gamma_2, \gamma_3$	Free
Other	Background level	Free

Results of the Rietveld analysis

As indicated in Figure 14, it turned out that the rhombohedral space group (Pbnm) was applicable to the samples with $x \leq 0.110$. An attempt to use this space group with the next sample in the series ($x = 0.165$) resulted in an unstable refinement (the minimization algorithm diverged). Likewise, the rhombohedral space group ($R\bar{3}c$) did only apply to the samples with $x \geq 0.165$. This suggests that the orthorhombic-to-rhombohedral phase transition takes place between $x = 0.110$ and 0.165 (at room temperature). It does not, however, exclude the possibility of the samples with x values near this composition range being multiphase. To examine this possibility further, the x-ray patterns of the $La_{0.67}Ca_{0.220}Sr_{0.110}MnO_3$ and $La_{0.67}Ca_{0.165}Sr_{0.165}MnO_3$ samples were refined with a Rietveld model allowing weighed contributions of both space groups. However, in the case

of $La_{0.67}Ca_{0.220}Sr_{0.110}MnO_3$, the minimization algorithm basically eliminated the weight of the rhombohedral space group and vice versa. Thus, the phase transition of the $La_{0.67}Ca_{0.33-x}Sr_xMnO_3$ system is restricted to the range $x \in [0.110; 0.165]$ and it appears to be rather sharp.

The result of the Rietveld analysis is summarized graphically in Figure 15 (p. 32). The figure shows experimental and calculated XRD patterns with residuals. The main reflections of the two end-members are labeled by corresponding crystallographic indices. The insets show enlarged views of the $2\theta = 32–33.3°$ regions. The relatively low amplitudes of the residual patterns (green lines) qualitatively indicate that the profile fits are good. This confirms that the structural model is valid. The large deviations seen in the vicinity of the Si reflections are due to the fact that these regions were excluded from the calculations. The splitting of the main reflection around $2\theta = 32.7°$, which can be ascribed to the phase transition, is clearly reproduced. For instance, the orthorhombic Pbnm space group allows for a weak shoulder on the low-angle side of the intense superposition of the 200, 112 and 020 reflections, while the complete splitting into a double-line can only be described by applying the rhombohedral $R\bar{3}c$ space group. Another important observation is the good agreement between the relative line intensities of the observed and the calculated x-ray patterns. The relative line intensities depend strongly on atom types and on the site occupation fractions. In the present analysis these parameters were fixed in accordance with the target compositions of the synthesis. Thus, the Rietveld analysis indicates that the sample compositions are close to nominal. However, for all the diffractograms, especially the one of $La_{0.67}Sr_{0.33}MnO_3$, a somewhat better fit could be obtained by allowing a slight variation of the oxygen content. This suggests a deviation from the nominal MnO_3 stoichiometry, emphasizing that $La_{0.67}Ca_{0.33-x}Sr_xMnO_{3\pm\delta}$ would be a more general formula for the manganite system (cf. Section 3.2). With this notion in mind the sample designations remain unchanged in the following.

Numerical values of the refined structural parameters are listed in Table 4 (p. 34) and Table 5 (p. 35). The tables show, respectively, results obtained for the orthorhombic and rhombohedral phases. Additional informative quantities calculated from these parameters are also listed.

Comparing the refined parameters of the seven $La_{0.67}Ca_{0.33-x}Sr_xMnO_3$ samples it is clear that the exchange of Ca by Sr causes systematic changes of the structural properties. For both the orthorhombic and the rhombohedral phases, the lattice parameters, and hence the unit cell volume, increase slightly with increasing x. The calculated density increases linearly (from 6040 kgm^{-3} for $La_{0.67}Ca_{0.33}MnO_3$ to 6390 kgm^{-3} for $La_{0.67}Sr_{0.33}MnO_3$) in accordance with the equidistant exchange of Ca with Sr. The compositional variation is also seen to cause changes of the relative atomic positions and thereby of bond lengths and bond angles. Selected inter-atomic distances and bond angles are listed in the tables. The Mn–O bonds are of particular interest because they play a crucial role to the magnetic and transport properties of the manganites (cf. Section 2.4). The orthorhombic phases have three inequivalent Mn–O bonds; one $Mn–O^{I}$ bond and two $Mn–O^{II}$ bonds. Although the individual bond lengths show some variation, the mean bond distance, $\langle d(\text{Mn–O})\rangle$, seems to be independent of the Ca/Sr ratio. For all values of x the mean Mn–O bond distance is about 0.196 nm. Almost equivalent values were obtained for the rhombohedral samples; cf. Table 5. Contrary to the Mn–O distance, the mean Mn–O–Mn bond angle is clearly influenced by the compositional variation. The bond angle increases gradually from about 162° for $La_{0.67}Ca_{0.33}MnO_3$ to about 170° for

$La_{0.67}Sr_{0.33}MnO_3$. In Figure 16 the mean Mn–O bond distance and the mean Mn–O–Mn bond angle are plotted against *x*.

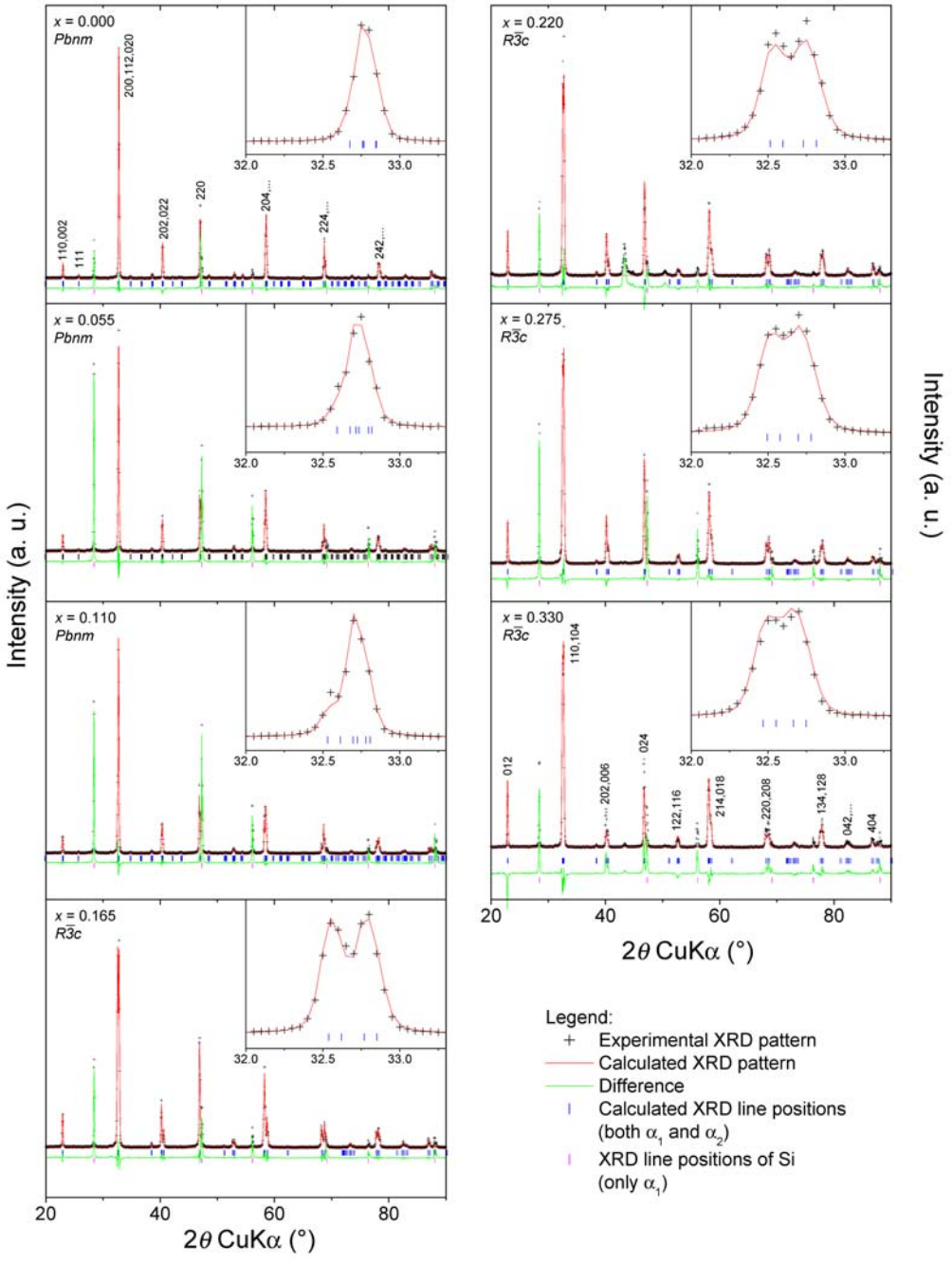

Figure 15. Experimental and refined XRD patterns for the seven $La_{0.67}Ca_{0.33-x}Sr_xMnO_3$ samples. Lines and symbols are explained in the legend. Insets show enlarged views of

the diffraction angle range $2\theta = 32–33.2°$ for each pattern. Miller indices of main reflections are shown for $La_{0.67}Ca_{0.33}MnO_3$ and $La_{0.67}Sr_{0.33}MnO_3$

Table 4. Refined structural parameters for the $La_{0.67}Ca_{0.33-x}Sr_xMnO_3$ sample with $x \leq 0.110$, i.e. orthorhombic phases. Content: Unit cell dimensions (a, b, c), unit cell volume (V), density (ρ), atomic positions (x, y, z) (no not confuse with composition parameter x), bond lengths (d) with corresponding number of nearest neighbors (NN), bond angles for selected bonds, and tolerance factors, t (defined in Section 2.3, p.13). Angular brackets indicate that the given values are an average of the refined values for the corresponding parameter. Units and errors (order of magnitude) are given in the rightmost column.*

Space group: Pbnm, $Z = 4$ (No. 62, 3)					
Unit cell angles: $\alpha = 90°$, $\beta = 90°$, $\gamma = 90°$					
Composition	x	0	0.055	0.110	
Unit cell	a	0.5471	0.5480	0.5491	$\pm 3 \cdot 10^{-4}$ nm
	b	0.5456	0.5457	0.5459	$\pm 3 \cdot 10^{-4}$ nm
	c	0.7709	0.7711	0.7712	$\pm 3 \cdot 10^{-4}$ nm
	V	0.230	0.230	0.231	$\pm 10^{-3}$ nm^3
	ρ	6040	6100	6160	± 10 kgm^{-3}
Site 4*a*	x	0	0	0	
	y	0	0	0	
Occupied by	z	0	0	0	
Mn^{3+}, Mn^{4+}	N	2.67, 1.33	2.67, 1.33	2.67, 1.33	
Site 4*c*	x	0.4974	0.4999	0.4991	$\pm 4 \cdot 10^{-4}$
	y	0.0202	0.0159	0.0135	$\pm 4 \cdot 10^{-4}$
Occupied by	z	0.25	0.25	0.25	
La^{3+}, Ca^{2+}, Sr^{2+}	N	2.67, 1.33, 0	2.67, 1.11, 0.22	2.67, 0.89, 0.44	
Site 4*c*	x	0.5428	0.5471	0.5445	$\pm 4 \cdot 10^{-4}$
	y	0.4912	0.4948	0.5012	$\pm 4 \cdot 10^{-4}$
Occupied by	z	0.25	0.25	0.25	
O^{2-I}	N	4	4	4	
Site 8*d*	x	0.2436	0.2223	0.2302	$\pm 4 \cdot 10^{-4}$
	y	0.2816	0.2740	0.2710	$\pm 4 \cdot 10^{-4}$
Occupied by	z	0.0389	0.0358	0.0329	$\pm 4 \cdot 10^{-4}$
O^{2-II}	N	8	8	8	
Bonds lengths	d(Mn–O^{I}), NN	0.1942, 2	0.1945, 2	0.1943, 2	$\pm 5 \cdot 10^{-4}$ nm
	d(Mn–O^{II}), NN	0.2056. 2	0.1978, 2	0.1962, 2	$\pm 5 \cdot 10^{-4}$ nm
	d(Mn–O^{II}), NN	0.1865, 2	0.1948, 2	0.1955, 2	$\pm 5 \cdot 10^{-4}$ nm
	$\langle d$(Mn–O)$\rangle$, NN	0.1954, 6	0.1957, 6	0.1953, 6	$\pm 5 \cdot 10^{-4}$ nm
	$\langle d$((La,Ca,Sr)–O)$\rangle$, NN	0.2602, 8	0.2604, 8	0.2623, 8	$\pm 5 \cdot 10^{-4}$ nm
Bond angles	$\angle$(Mn–O^{I}–Mn)	166.87	164.57	165.58	±0.5°
	$\angle$(Mn–O^{II}–Mn)	160.34	160.04	162.46	±0.5°
	$\langle\angle$(Mn–O–Mn)$\rangle$	162.50	161.55	163.5	±0.5°
Tolerance factor	t^*	0.918	0.920	0.923	
Fit information	χ^2	2.5	2.6	2.7	

Table 5. Refined structural parameters (for room temperature) of $La_{0.67}Ca_{0.33-x}Sr_xMnO_3$ samples with $x \geq 0.165$ (rhombohedral phases Content: Unit cell dimensions (a, b, c), unit cell volume (V), density (ρ), atomic positions (x, y, z) (no not confuse with composition parameter x), bond lengths (d) with corresponding number of nearest neighbors (NN), bond angles for selected bonds, and tolerance factors, t (defined in Section 2.3, p.13). Angular brackets indicate that the given values are an average of the refined values for the corresponding parameter. Units and errors (order of magnitude) are given in the rightmost column.*

Space group: $Z = 6$ (No. 167) Unit cell angles: $\alpha = 90°$, $\beta = 90°$, $\gamma = 120°$							
Composition	x		0.165	0.220	0.275	0.330	
Unit cell	a		0.5491	0.5499	0.5497	0.5504	$\pm 3{\cdot}10^{-4}$ nm
	b		0.5491	0.5459	0.5497	0.5504	$\pm 3{\cdot}10^{-4}$ nm
	c		1.3311	1.3340	1.3345	1.3364	$\pm 3{\cdot}10^{-4}$ nm
	V		0.348	0.349	0.349	0.351	$\pm 10^{-3}$ nm^3
	ρ		6230	6270	6340	6390	± 10 kgm^{-3}
Site 6*b*	x		0	0	0	0.0	
	y		0	0	0	0.0	
Occupied by	z		0	0	0	0.0	
Mn^{3+}, Mn^{4+}	N		4, 2	4, 2	4, 2	4, 2	
Site 6*a*	x		0	0	0	0	
	y		0	0	0	0	
Occupied by	z		0.25	0.25	0.25	0	
La^{3+}, Ca^{2+}, Sr^{2+}	N		4, 1, 1	4, 0.67, 0.33	4, 0.33, 1.67	4, 0, 2	
Site 18*e*	x		0.4493	0.4502	0.4556	0.4578	± 10 kgm^{-3}
	y		0	0	0	0	
Occupied by	z		0.25	0.25	0.25	0.25	
O^{-2}	N		18	18	18	18	
Bond lengths	d(Mn–O), NN		0.1955, 6	0.1957, 6	0.1953, 6	0.1948, 6	$\pm 5{\cdot}10^{-4}$ nm
	$\langle d$((La,Ca,Sr)–O)$\rangle$, NN		0.2638, 8	0.2644, 8	0.2654, 8	0.2679, 8	$\pm 5{\cdot}10^{-4}$ nm
Bond angles	$\angle$(Mn–O–Mn)		163.62	163.92	165.65	169.62	±0.5°
Tolerance factor	t^*		0.925	0.928	0.931	0.934	
Fit information	χ^2		2.8	4.1	1.9	2.9	

Figure 17 (p. 37) displays graphical representations of the crystal structures of the orthorhombic and rhombohedral phases as seen from various spatial directions. The three-dimensional models were based on the refined atomic positions of the $La_{0.67}Ca_{0.33}MnO_3$ and $La_{0.67}Sr_{0.33}MnO_3$ samples, respectively. Similarly to the elementary perovskite structure shown in Figure 1 (p. 14), the compounds are seen to consist of MnO_6 octahedra residing in the lattice formed by La, Ca, and Sr. The MnO_6 octahedra are linked in the corners and form three-dimensional networks. Mn–O–Mn–O–… chains extend in different crystallographic directions. The MnO_6 octahedra are tilted and rotated and the deviations from the ideal 180° Mn–O–Mn bond angles of the parent cubic perovskite structure are evident. The largest tilt angles (and therefore smallest Mn–O–Mn bond angles) are seen for the Pbnm compounds.

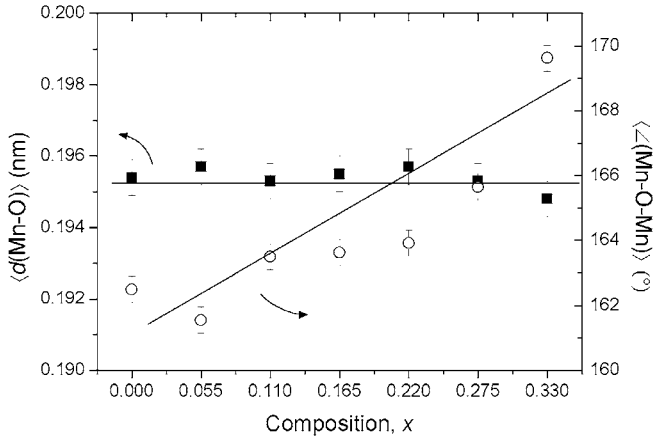

Figure 16. Average Mn–O bond distance (closed squares) and mean Mn–O–Mn bond angle (open circles) in $La_{0.67}Ca_{0.33-x}Sr_xMnO_3$ as a function of the composition parameterx. Solid lines are linear fits serving as guides to the eye.

With respect to the crystallographic properties, the principal difference between the members of the $La_{0.67}Ca_{0.33-x}Sr_xMnO_3$ series is the mean ionic radius $\langle r_A \rangle$ of the A-site cations (La, Ca, and Sr). The mean ionic radius increases systematically with increasing x due to the difference in ionic radii of Ca^{2+} and Sr^{2+} (cf. Table 1 and Figure 18). This suggests that $\langle r_A \rangle$ is the essential structural parameter responsible for the change of the Mn–O–Mn bond angle. This assertion is supported by previous investigations on the relationship between composition and structure in perovskite manganites (García-Muñoz *et al*., 1996; García-Muñoz *et al*., 1997; Hwang *et al*., 1995). These authors also considered manganite systems with ~33 % divalent A-site substitution and studied the effect of varying the mean radius of the A-site ions. However, rather than changing the size of the divalent cation, their approach was to vary the size of the trivalent A-site member, i.e. they considered the series $(R_{1-y}R'_y)_{0.67}A_{0.33}MnO_3$, where (R, R') = La, Y, Nd, etc., and A = Ca, Sr, Ba, etc. The authors obtained results to a very high degree resembling the results obtained for the $La_{0.67}Ca_{0.33-x}Sr_xMnO_3$ series in the present work: The mean Mn–O bond was nearly the same, i.e. ~0.196 nm, for all the members of the $(R_{1-y}R'_y)_{0.67}A_{0.33}MnO_3$ series, and thus equivalent to the Mn–O bond distance in the $La_{0.67}Ca_{0.33-x}Sr_xMnO_3$ samples. The mean Mn–O–Mn bond angle increased systematically with increasing A-site ionic radius at a rate of 1226°/nm. The corresponding value for the $La_{0.67}Ca_{0.33-x}Sr_xMnO_3$ series of this study is 1391°/nm. Regardless of the precise nature of the R, R', and A ions, the compounds with $\langle r_A \rangle \lesssim 0.124$ nm were orthorhombic

(Pbnm symmetry), while the compounds with $\langle r_A \rangle \gtrsim 0.124$ nm were rhombohedral ($R\bar{3}c$ symmetry). For the $La_{0.67}Ca_{0.33-x}Sr_xMnO_3$ series the transition from orthorhombic to rhombohedral symmetry occurs around $x = 0.110$–0.165, i.e. for $\langle r_A \rangle \approx 0.123$ nm (cf. Figure 18).

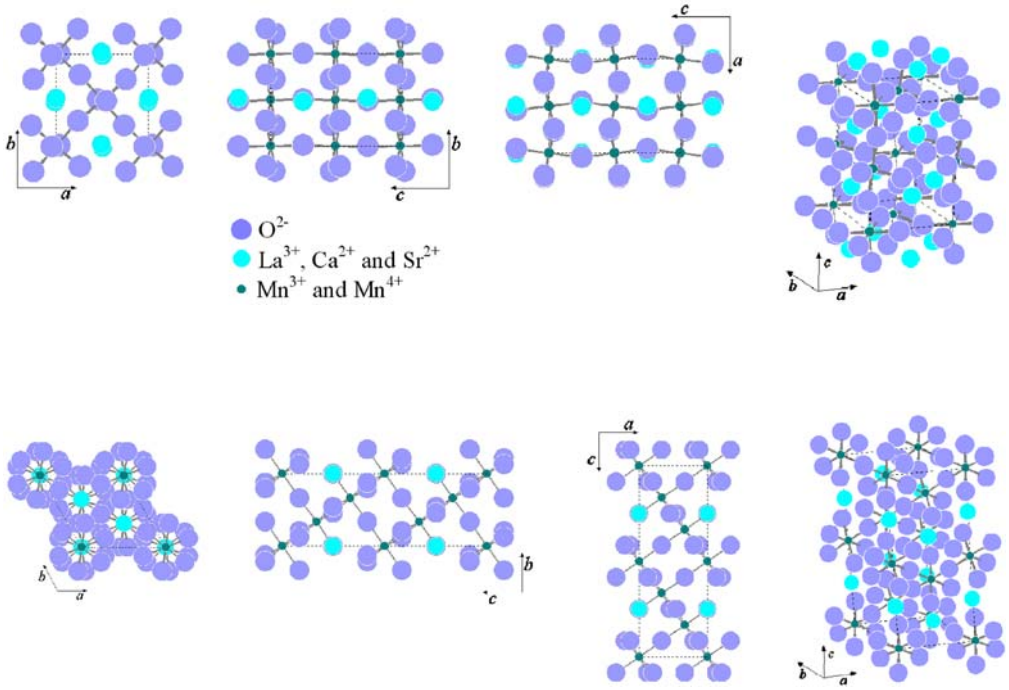

Figure 17. Graphical representations based on refined atomic positions of the orthorhombic Pbnm phase, e.g. $La_{0.67}Ca_{0.33}MnO_3$ (top panels) and the rhombohedral (R3c) phase, e.g. $La_{0.67}Sr_{0.33}MnO_3$ (bottom panels). From left are shown projections onto the ab, bc and ac lattice planes, and the structures seen from a random spatial direction. The legend identifies the ions. Unit cell boundaries are indicated by dotted lines.

Together these results stress that $\langle r_A \rangle$ is a fundamental structural parameter, not only for $La_{0.67}Ca_{0.33-x}Sr_xMnO_3$ series but for the manganite family $R_{1-x}A_xMnO_3$ in general. This can be understood by invoking the Goldsmith's tolerance factor, t^*, which was introduced in Section 2.3 (cf. Equation (1)). t^* values of the $La_{0.67}Ca_{0.33-x}Sr_xMnO_3$ series are listed in Table 4 and Table 5, and is plotted against x in Figure 18. The tolerance factor is 0.918 for the $x = 0$ end-member and it increases linearly to 0.934 for $x = 0.33$, in accordance with the increasing mean ionic radius. The tolerance factor can be regarded as a measure of the size mismatch between the radius of the A-site ions and the space between the MnO_6 octahedra, where they reside (Hwang *et al.*, 1995). $t^* = 1$ corresponds to a perfect size match and the Mn–O–Mn bond angle would be 180° (*ibid.*). When $t^* < 1$, the A-site ions are too small to fill the space between the MnO_6 octahedra. This forces the octahedra to tilt and rotate in an attempt to reduce the excess space around the A-site. The results in a decrease of the Mn–O–Mn bond angle.

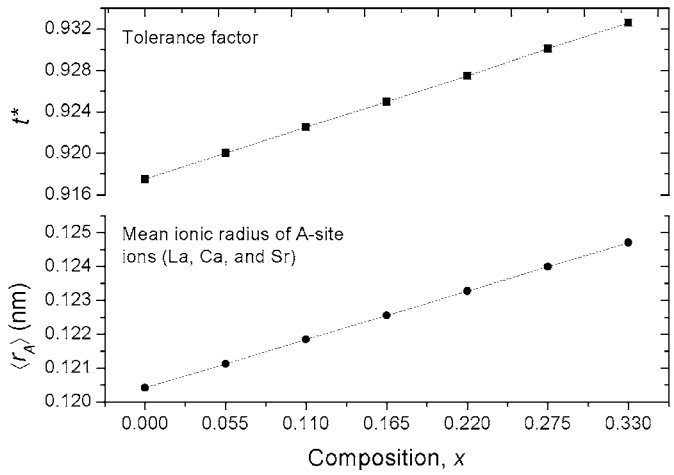

Figure 18. Tolerance factor, t^*, (top panel) and mean radius $\langle r_A \rangle$ of A-site ions (bottom panel) as a function of the composition parameter x of the $La_{0.67}Ca_{0.33-x}Sr_xMnO_3$ series. Mean radii were calculated by the expression $\langle r_A \rangle = 0.67 r_{La^{3+}} + (0.33 - x) r_{Ca^{2+}} + x r_{Sr^{2+}}$ using values of ionic radii listed in Table 1 (assuming nine-fold coordination for the A-sites). Tolerance factors were calculated using Equation (1).

In the following, the linkage between the crystal structure and other physical properties of the $La_{0.67}Ca_{0.33-x}Sr_xMnO_3$ samples will be treated in detail. The discussion of the crystallographic structure and the Rietveld analysis is therefore concluded here with a brief summary:

- The $La_{0.67}Ca_{0.33-x}Sr_xMnO_3$ samples with a low Sr content have orthorhombic symmetry (space group Pbnm), while the samples with a high Sr content are rhombohedral (space group $3\overline{R}c$). The phase transition takes place in the composition range $0.110 \leq x \leq 0.165$.
- The Rietveld analysis showed that the chemical compositions of the $La_{0.67}Ca_{0.33-x}Sr_xMnO_3$ samples are close to the nominal target compositions.
- The Mn–O bond distance is ~0.196 nm and is independent of x.
- The Mn–O–Mn bond angle increases systematically with x (from 162° to 170°).
- There exist a correlation between the mean A-site radius $\langle r_A \rangle$ (which is directly proportional to x) and the Mn–O–Mn bond angle. This can be understood from the distortion of the network of MnO_6 octahedra arising from the size mismatch between $\langle r_A \rangle$ and the space left between the octahedra.

4.4 Magnetic properties: Curie transitions

Figure 19 shows the temperature dependence of the inverse low-field susceptibility for the $La_{0.67}Ca_{0.33-x}Sr_xMnO_3$ compounds as calculated from magnetization data. Here the susceptibility is defined as $(\sigma/H)^{-1}$ (the susceptibility is usually defined as M/H, where M is the magnetization per volume). The samples exhibit Curie-Weiss behavior, i.e. linear temperature dependence in the paramagnetic part of the inverse susceptibility. The Curie temperatures were determined by extrapolating the paramagnetic part of the inverse susceptibility, as shown for the $La_{0.67}Sr_{0.33}MnO_3$ sample. This was done by linear regression with an error of about ±2 K.

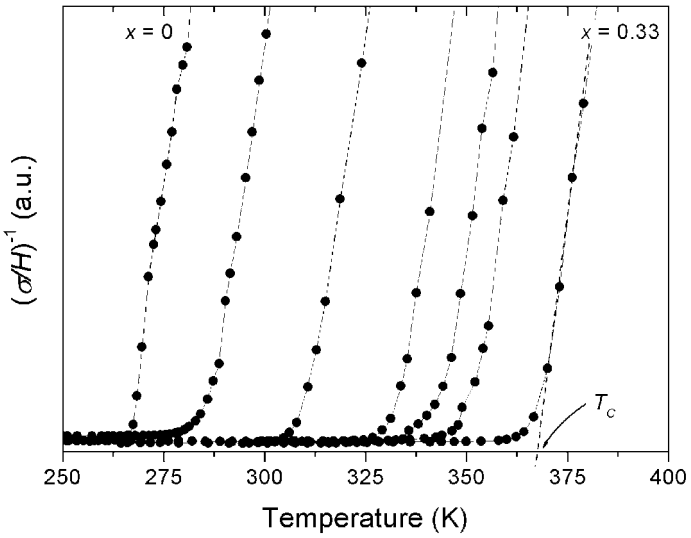

Figure 19. Inverse susceptibility (defined as $(\sigma/H)^{-1}$) of the $La_{0.67}Ca_{0.33-x}Sr_xMnO_3$ samples. Curie temperatures were deduced by extrapolation of the linear parts of the susceptibility curves as shown for the $La_{0.67}Sr_{0.33}MnO_3$ sample (x = 0.33).

Figure 20 shows the deduced T_C values as a function of the composition parameter x. The Curie temperature increases systematically with x but with a decreasing rate, which could indicate that T_C is approaching a saturation level. The T_C range of the $La_{0.67}Ca_{0.33-x}Sr_xMnO_3$ series spans about 100 K, from 267 K for the $x = 0$ end-member to 369 K for the $x = 0.33$ end-member.

It is evident that x can be used as a tuning parameter for the Curie temperature. This is of great practical interest, because it allows for tailoring of compounds with pre-specified properties (for instance, both the magnetocaloric effect and the magnetoresistance are expected to exhibit maxima near T_C). A least-squares fit to a second order polynomial suggested the following purely empirical relationship between the Curie temperature and x: $T_C(x) \approx (-480x^2 + 462x + 265)$ K (shown as a dotted line in Figure 20). For example, the compound $La_{0.67}Ca_{0.26}Sr_{0.07}MnO_3$ would be expected to show a Curie transition at room temperature (assuming that the sample synthesis is carried out as described in Chapter 3).

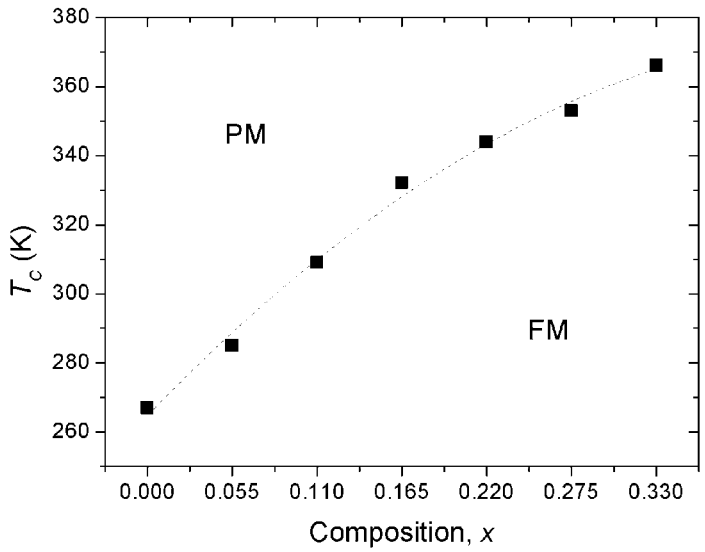

Figure 20. Curie temperatures of the $La_{0.67}Ca_{0.33-x}Sr_xMnO_3$ compounds as a function of x. The paramagnetic (PM) and ferromagnetic (FM) regimes are indicated. The dotted line represents the best fit to a second order polynomial and is given by $T_C(x) = (-480x^2 + 462x + 265)$ K.

4.5 Relationship between structure and magnetism

In Figure 21 the Curie temperatures obtained for the $La_{0.67}Ca_{0.33-x}Sr_xMnO_3$ compounds have been plotted into a phase diagram of temperature versus mean A-site ionic radius for the manganite system $R_{0.7}A_{0.3}MnO_3$ (R = trivalent rare earth ion, A = divalent alkali earth ion). In spite of the slight difference between the divalent doping factors (0.33 in the present investigation), the T_C values fits very well into the phase diagram, which was constructed from results obtained for a broad range of compositions prepared by substituting various ions into the A-site (Hwang *et al.*, 1995).

Figure 21 emphasizes that the Curie temperature depends more specifically on the mean radius, $\langle r_A \rangle$, of the A-site ions than on the composition parameter x. Even more specifically, the relationship between T_C and $\langle r_A \rangle$ is due to the linkage between $\langle r_A \rangle$ and the Mn–O–Mn bond angle. This can be understood from the following: The concept of double-exchange and magnetic interaction in mixed-valence manganites were discussed previously (cf. Section 2.4). To recapitulate, the ferromagnetic properties of manganite systems are ascribed to the hopping of mobile e_g (S = 1/2) electrons between localized Mn^{4+} core spins (S = 3/2) with strong on-site Hund's coupling. The hopping takes place via the interstitial oxygen ion. The strength of the ferromagnetic coupling is related to the hybridization strength between e_g(Mn)–$2p_\sigma$(O)–e_g(Mn) orbitals (Coey *et al.*, 1999). The orbital overlap, and thereby the hybridization strength, depend strongly on both the Mn–O distance and the Mn–O–Mn bond angle. Intuitively, it seems that the hybridization is weakened when the bond angle decreases (see inset, Figure 22). Thus, a smaller Mn–O–Mn bond angle gives a weaker ferromagnetic coupling and thereby a lower Curie temperature (recall that T_C represents the temperature, where the ferromagnetic exchange energy can no longer compensate for the thermally induced spin fluctuations).

Figure 22 shows the Curie temperatures of the $La_{0.67}Ca_{0.33-x}Sr_xMnO_3$ series as a function of the mean Mn–O–Mn bond angle obtained from the Rietveld analysis. In accordance with the above considerations, T_C increases with increasing bond angle. For large angles T_C seems to saturate. The solid line represents a least-squares fit to the expression

$T_C(\varphi) = \alpha\cos(\varphi) + \beta\cos^2(\varphi) + \gamma\cos^3(\varphi)$, where φ denotes the bond angle. The value of β was found to be one order of magnitude larger than the values of α and γ. Thus, to first approximation $T_C(\varphi) \approx \cos^2(\varphi)$ (fitted values for α, β, and γ are given in the caption of Figure 22). A similar result (with slightly larger α, β, and γ values, however) were obtained by García-Muñoz *et al*. (1996), whom considered the relationship between the Mn–O–Mn bond angle and T_C for variously A-site substituted $R_{1-y}A_yMnO_3$ compounds with $y \approx 0.67$. The authors performed electronic band width simulations and showed that the overlap between the e_g(Mn)–$2p_\sigma$(O)–e_g(Mn) orbitals to first order also scales with $\cos^2(\varphi)$, once again pointing to a close relationship between T_C and the orbital overlap and thereby the bond angle.

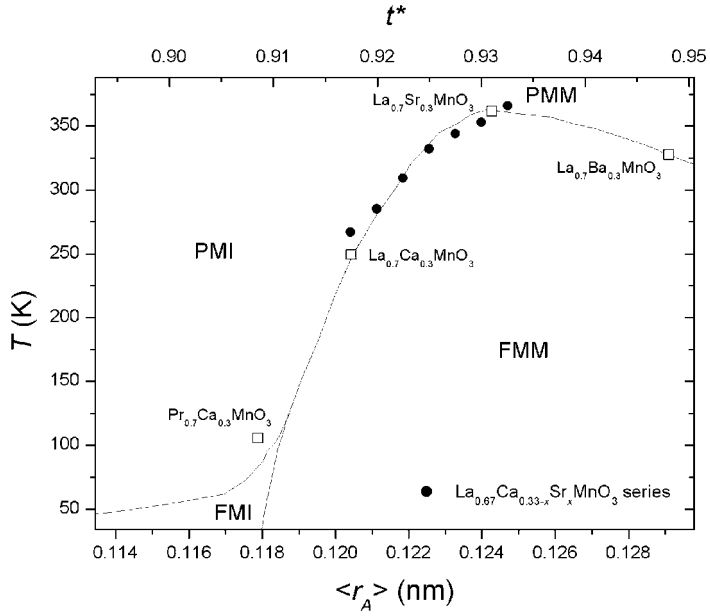

Figure 21. Phase diagram illustrating the relationship between the mean radius of the A-site ions and the magnetic transition temperature in the manganite family $R_{0.7}A_{0.3}MnO_3$ (R = trivalent rare-earth cation, A = divalent alkali earth cation). Round symbols denote T_C values obtained for the $La_{0.67}Ca_{0.33-x}Sr_xMnO_3$ series of the present investigation. The different magnetic (and electronic) regimes are designated PMI (paramagnetic insulator), PMM (paramagnetic metal), FMM (ferromagnetic metal), and FMI (ferromagnetic insulator). Diagram adopted from Hwang et al. (1995).

Even though the Mn–O–Mn bond angle and $\langle r_A \rangle$ play decisive roles for the magnetic coupling strength in mixed-valence manganites these are not the only factors influencing T_C. For instance, there is a tendency for the Curie temperature to decrease with increasing electropositivity of the divalent A-site cation, because a more electropositive cation will tend to strengthen the t_g(Mn)–$2p_\sigma$(O)–t_g(Mn) hybridization, which causes antiferromagnetic coupling between Mn neighbors (García-Muñoz *et al*., 1997). This is mentioned to emphasize that the relationship between T_C and $\langle r_A \rangle$, which is evident for the $La_{0.67}Ca_{0.33-x}Sr_xMnO_3$ series and for other mixed-valence manganite systems, cannot be generalized to put forward an universal T_C versus $\langle r_A \rangle$ law. By comparing results for a wide range of compositions Thomas *et al*. (1997) showed that there is no clear trend associating the Curie temperature of mixed-valence manganites with the size, atomic weight, or electropositivity of the divalent A-site cation.

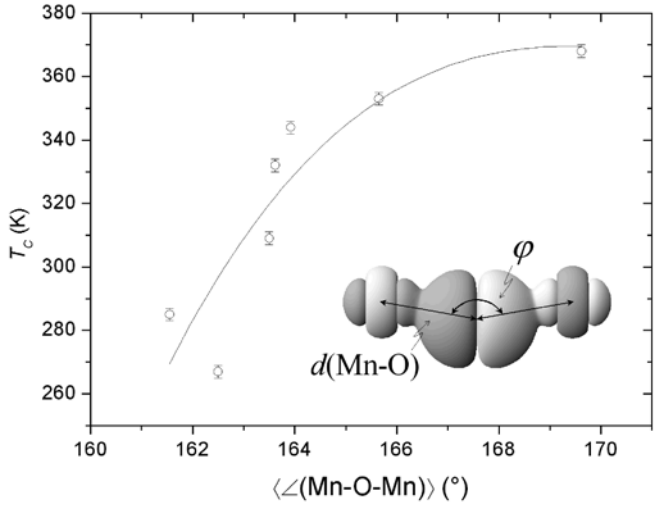

Figure 22. Curie temperature, T_C, of the $La_{0.67}Ca_{0.33-x}Sr_xMnO_3$ series as a function of the refined mean Mn–O–Mn bond angle. Solid line is the best fit to the expression $T_C(\varphi) = \alpha \cos(\varphi) + \beta \cos^2(\varphi) + \gamma \cos^3(\varphi)$, with $\alpha = 8.9 \cdot 10^4$, $\beta = 1.8 \cdot 10^5$, and $\gamma = 9.2 \cdot 10^4$ (φ denotes the bond angle). The inset illustrates the overlap between two manganese e_g orbitals with an interstitial oxygen p_σ orbital. The orbitals and the orbital separation are drawn approximately to correct scale.

4.5.1 Broadening of the Curie transition

From Figure 19 (p. 39) it appears that the ferromagnetic transition in the $La_{0.67}Ca_{0.33}MnO_3$ sample is markedly sharper than the transition of the remaining samples in the series. This is also illustrated in Figure 23 (a), which shows the temperature dependence of the specific magnetization around the Curie point for the two end-members and the intermediate $x = 0.165$ compound. Several factors may explain the different rates at which the magnetization drops in the $La_{0.67}Ca_{0.33-x}Sr_xMnO_3$ samples. Variations in compositional homogeneity or oxygen stoichiometry could cause variations of the Curie temperature on a local scale and thereby a smearing of the overall Curie transition. However, the maximum slope of the magnetization curves, i.e. the slope at T_C, decreases very systematically with x, indicating that there exist a more direct relationship between the composition and the broadening of the Curie transition for the $La_{0.67}Ca_{0.33-x}Sr_xMnO_3$ system.

The broadening of the magnetic transition could be attributed to the decreasing grain size associated with the increased Sr content (cf. Section 3.5). A smaller grain size gives a larger proportion of surface-near spins, which may be weaker ferromagnetically coupled than spins in the bulk of the grains. This could give a distribution of Curie temperatures and thus a broadened magnetic transition. A grain size dependent broadening of the Curie transition has previously been observed in granular Sr-doped lanthanum manganites (Zhang *et al*., 1997; Zhang *et al*., 1999).

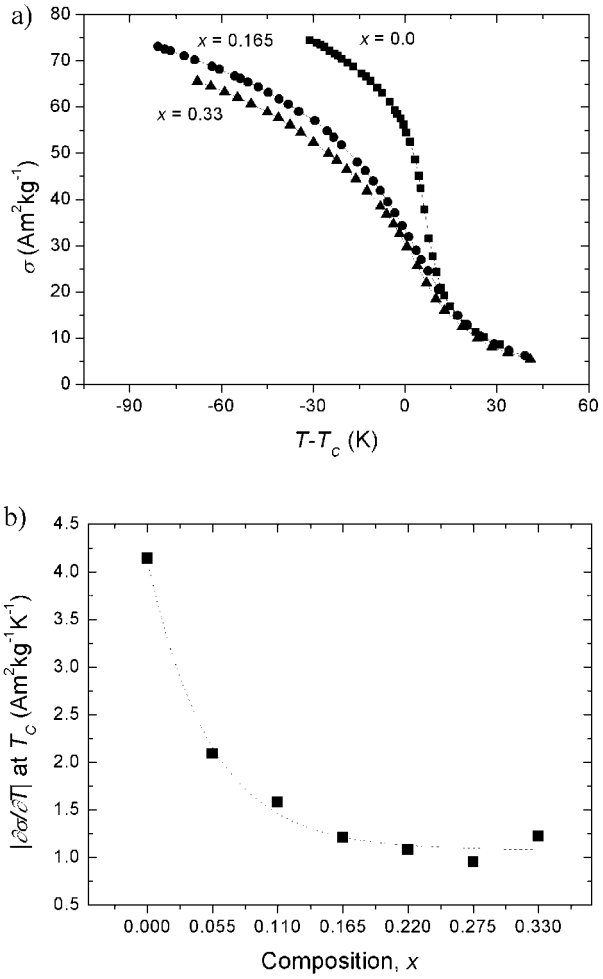

Figure 23. a) Specific magnetization as a function of temperature (relative to T_C) in a constant magnetic field of 1.2T for three selected $La_{0.67}Ca_{0.33-x}Sr_xMnO_3$ samples. b) Slope of magnetization curve at the Curie point as a function of composition (given by x). Dotted line serves as guide to the eye.

It has been shown (Radaelli *et al*., 1995; Dai *et al*., 1996; Guo *et al*., 1997), that the ferromagnetic transition in Ca-doped lanthanum manganites can be accompanied by an abrupt change of the lattice parameters. This effect was attributed to an electron-phonon coupling arising from the dynamic Jahn-Teller distortion of the MnO_6 octahedra. Mn^{3+} is a strong Jahn-Teller ion, i.e. it can benefit energetically from a lowering of the symmetry of the crystal field set up by its oxygen neighbors and will therefore tend to cause a distortion of the MnO_6 octahedra (cf. Section 2.4). The Jahn-Teller splitting of the e_g(Mn) orbital is closely related to the orbital overlapping in the MnO_6 octahedra. An increased electron-phonon coupling is expected when the band width associated with the e_g(Mn)–$2p_\sigma$(O)–e_g(Mn) hybridization becomes narrower (García-Muñoz *et al*., 1997). For the $La_{0.67}Ca_{0.33-x}Sr_xMnO_3$ system this would imply that the electron-phonon coupling is enhanced when the Ca content increases, i.e. when the x value is small (a lower x gives a smaller Mn–O–Mn angle and thus a narrower e_g(Mn)–$2p_\sigma$(O)–e_g(Mn) band width). It is possible that a coupling between the lattice and magnetism via the dynamic Jahn-Teller distortion plays a role to the very sharp drop in magnetization observed for the $La_{0.67}Ca_{0.33}MnO_3$ sample because an abrupt change of the unit cell volume at T_C could

contribute to the change of magnetization. This suggestion is, of course, purely speculative. The temperature dependence on the lattice parameters in the vicinity of T_C definitely deserves to be investigated further.

4.6 Summary and conclusions

The structural properties of the $La_{0.67}Ca_{0.33-x}Sr_xMnO_3$ series were analyzed by means of x-ray diffraction (at room temperature) and the Rietveld technique. The variation of the Ca/Sr ratio (given by x) was found to cause significant structural changes. The main findings were a crossover from Pbnm to $R\bar{3}c$ symmetry in the composition range $x \in [0.110; 0.165]$ and a strong dependence of the properties of the Mn–O-Mn bond on the x parameter. The structural changes were ascribed to the change of the mean radius $\langle r_A \rangle$ of the A-site ions caused by the exchange of Ca and Sr. The Mn–O–Mn bond angle was found to increase with the mean A-site ionic radius. The Mn–O bond distance, however, was nearly the same in all members of the series. The ferromagnetic Curie temperature of the samples was determined from magnetization measurements. T_C increased systematically with x. This was also assigned to the gradual increase of $\langle r_A \rangle$, or, more specifically to the increase of the Mn–O–Mn bond angle, which affects the e_g(Mn)–$2p_\sigma$(O)–e_g(Mn) orbital overlap and thereby the strength of the magnetic coupling between neighboring Mn ions. Hence, through the dependence sequence $x \rightarrow \langle r_A \rangle \rightarrow \langle \angle(\text{Mn–O–Mn}) \rangle \rightarrow T_C$, the Curie temperature of $La_{0.67}Ca_{0.33-x}Sr_xMnO_3$ can be adjusted using x as tuning parameter. A systematic broadening of the ferromagnetic transition with increasing x was observed. This was ascribed to decreasing grain size associated with a larger Sr content. Dynamic Jahn-Teller distortion might be of significance to the drop in magnetization at T_C, especially for the samples with low x values.

5 Magnetocaloric properties of the $La_{0.67}Ca_{0.33-x}Sr_xMnO_3$ series

5.1 Introduction

This chapter presents results of an investigation of the magnetocaloric properties of the samples in the $La_{0.67}Ca_{0.33-x}Sr_xMnO_3$ series. As described in Section 5.2, the magnetocaloric effect in a material can be expressed in two terms: the isothermal magnetic entropy change ΔS_M, and the adiabatic temperature change ΔT_{ad} upon a change of the applied magnetic field, respectively. Both quantities are temperature and magnetic field dependent and are often written $\Delta S_M(T)_{\Delta H}$ and $\Delta T_{ad}(T)_{\Delta H}$, respectively. In the present study both magnetocaloric quantities were measured. The consistency of the two kinds of measurements was evaluated using results of heat capacity measurements. A model for the magnetocaloric effect, based on Weiss mean field theory and classical theories for heat capacity contributions, is established. A comparison between observed and calculated magnetocaloric effects will be presented. The chapter is concluded with a discussion on the application of the $La_{0.67}Ca_{0.33-x}Sr_xMnO_3$ compounds for magnetic refrigeration. First, a general introduction to the magnetocaloric effect is given.

5.2 The magnetocaloric effect

When a dc magnetic field is applied to a solid, which is thermally isolated from its surroundings, a change of the temperature of the solid may be observed. This phenomenon is known as magnetocaloric effect or, more precisely, the adiabatic temperature change due to a change of the applied magnetic field. The magnetocaloric effect was first discovered by Warburg (1881) in pure iron and explained physically by Debye (1926) and Giauque (1927).

The magnetocaloric effect is the result of entropy changes arising from the coupling of the magnetic spin system of the solid with the applied magnetic field. The total entropy of a magnetic solid is the sum of the lattice, electronic, and magnetic entropies (S_L, S_E, and S_M, respectively). In most cases the lattice and electronic entropies are essentially independent of the magnetic field H, whereas the magnetic entropy depends strongly on H. An applied field will usually tend to align the magnetic spins and thus decrease the entropy of the spin system (see Figure 24). Hence, if the applied field is changed by ΔH at a constant temperature T, the magnetic entropy is changes $\Delta S_M(T)_{\Delta H}$, while S_L and S_E remain constant. The quantity $\Delta S_M(T)_{\Delta H}$ is the isothermal magnetic entropy change.

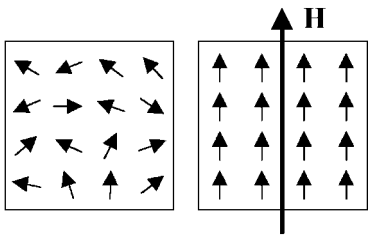

Figure 24. Simplified illustration of the effect of applying an external magnetic field **H** *to a ferromagnetic spin system. The field increases the order in the spin system by forcing the spins to align in its direction. Increasing order corresponds to decreasing entropy.*

If the change of the magnetic field takes place adiabatically, the total entropy is conserved. In this case, the combined lattice and electronic entropies must change by $\Delta(S_L + S_E) = -\Delta S_M$ in order to fulfill the condition $\Delta S = 0$. The change of lattice and electronic entropies may cause a change of the temperature of the magnetic solid, e.g. by intensified or reduced lattice vibrations, depending on the sign of ΔH. This temperature change is the adiabatic temperature change, $\Delta T_{ad}(T)_{\Delta H}$, introduced above. Due to the linkage between the isothermal magnetic entropy change and the adiabatic temperature change the magnetocaloric effect may be expressed in both terms. The schematic *S*–*T* diagram in Figure 25 illustrates the relationship between the two quantities. The figure shows the total entropy of a ferromagnetic solid in two different external magnetic fields, H_I and H_F, respectively, where $H_F > H_I$. $\Delta S_M(T)_{\Delta H}$ and $\Delta T_{ad}(T)_{\Delta H}$ are indicated for a given value of T and a magnetic field change $\Delta H = H_F - H_I$.

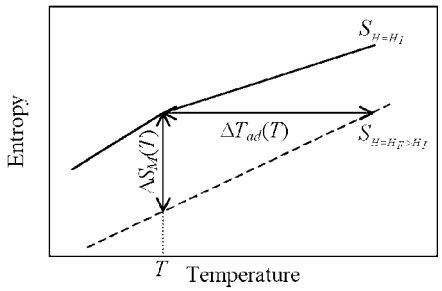

Figure 25. Schematic S–T diagram for a ferromagnetic solid, showing the total entropy in magnetic fields H_I and H_F, respectively ($H_F > H_I$), and illustrating the presence of the magnetocaloric effect at temperature T. The vertical arrow shows the isothermal magnetic entropy change, $\Delta S_M(T)_{\Delta H}$, and the horizontal arrow shows the adiabatic temperature change, $\Delta T_{ad}(T)_{\Delta H}$.

5.2.1 Basic thermodynamics of the magnetocaloric effect

According to classical thermodynamics and the thermodynamic Maxwell equation, the infinitesimal entropy change *dS* in a spin system can be calculated (Morrish, 1965) from

$$dS = \left(\frac{\partial S}{\partial T}\right)_H dT + \mu_0 \left(\frac{\partial \sigma}{\partial T}\right)_H dH \,, \tag{5}$$

where *dT* is the temperature change, σ the magnetization, μ_0 the permeability of free space, and *dH* the change of the external magnetic field. For an isobaric process at constant *H* the second law of thermodynamics gives

$$\left(\frac{\partial S}{\partial T}\right)_H = \frac{C_{P,H}}{T} \,, \tag{6}$$

where $C_{P,H}$ is the heat capacity at constant pressure, *P*, and constant magnetic field. Considering a reversible adiabatic process ($dS = 0$) and combining Equations (5)and (6) it is found that

$$dT = -\mu_0 \frac{T}{C_{P,H}} \left(\frac{\partial \sigma}{\partial T}\right)_H dH \,. \tag{7}$$

The adiabatic temperature change is now obtained by integrating Equation (7) from the initial field, H_I, to the final field, H_F:

$$\Delta T_{ad}(T)_{\Delta H} = -\mu_0 \int_{H_I}^{H_F} \frac{T}{C_{P,H}} \left(\frac{\partial \sigma}{\partial T} \right)_H dH \,. \tag{8}$$

The adiabatic temperature change is seen to be proportional to the absolute temperature and to the derivative of the magnetization with respect to temperature at constant magnetic field, while it is inversely proportional to the heat capacity at constant pressure and constant field. For paramagnetic and ferromagnetic substances, the magnetization decreases with temperature and hence, $(\partial\sigma/\partial T)_H$ is negative. T and $C_{P,H}$ are always positive and it follows that a positive change of the magnetic field is associated with a positive adiabatic temperature change, as expected.

For an isothermal magnetization process, the magnetic contribution to the entropy change ΔS_M can be deduced from Equation (5), once again integrating over the field gives the following expression:

$$\Delta S_M(T)_{\Delta H} = \mu_0 \int_{H_I}^{H_F} \left(\frac{\partial \sigma}{\partial T} \right)_H dH \tag{9}$$

Once more using the argument that $(\partial\sigma/\partial T)_H$ is negative, it is seen that a positive change of the magnetic field gives rise to a negative change of the magnetic entropy, as one would expect from intuition.

The relationship between the adiabatic temperature change and the isothermal magnetic entropy change is far from trivial. Equation (6) can be rewritten as

$$dS(T)_H = \frac{C_{P,H}}{T} dT \tag{10}$$

and hence,

$$-\Delta S_M(T)_{\Delta H} = \int_{T}^{T+\Delta T_{ad}(T)_{\Delta H}} \frac{C(T)_{P,H_F}}{T} dT \tag{11}$$

It can be shown (Pecharsky *et al*., 2001) that the following equation is a solution of Equation (11):

$$\Delta S_M(T)_{\Delta H} = -\frac{C(T_1)_{P,H_F}}{T_1} \Delta T_{ad}(T)_{\Delta H} \,, \tag{12}$$

where T_1 is an unknown temperature in the interval $[T;T+\Delta T_{ad}(T)_{\Delta H}]$. For small adiabatic temperature changes, T_1 can be approximated by T, which gives

$$\Delta S_M(T)_{\Delta H} \cong -\frac{C(T)_{P,H_F}}{T} \Delta T_{ad}(T)_{\Delta H} \,. \tag{13}$$

In summary, the theoretical expressions of the adiabatic temperature changes and the isothermal magnetic entropy change due to a change to the applied magnetic field are given by Equations (8) and (6), respectively, and the quantities can be correlated using Equation (13).

From these equations it follows that the magnetocaloric effect (if taken as the absolute value of $\Delta S_M(T)_{\Delta H}$ or $\Delta T_{ad}(T)_{\Delta H}$) is large when $\left|\partial\sigma / \partial T\right|$ is large, i.e. when the magnetization changes rapidly with temperature. The largest magnetocaloric effect would therefore be expected at temperatures close to magnetic transitions temperatures, i.e. for ferromagnetic materials in the vicinity of the Curie temperature, T_C; see Figure 26.

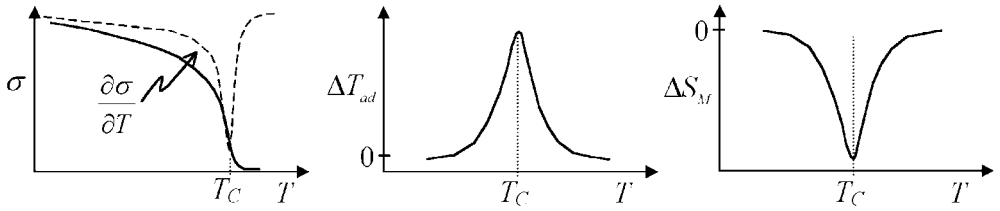

Figure 26. Schematic illustration of the temperature dependence of magnetization and the corresponding magnetocaloric effect in a ferromagnetic material. The magnetization changes rapidly around the Curie temperature T_C. According to Equations (8) and (9) this gives rise to a positive peak for the adiabatic temperature change and a negative peak for isothermal magnetic entropy change.

5.3 Experimental techniques

The magnetic entropy change is not directly measurable, but as will be shown below, $\Delta S_M(T)_{\Delta H}$ can be derived from magnetization measurements. This approach is referred to as an indirect measurement of the magnetocaloric effect. The adiabatic temperature change can be measured directly. Measurements of $\Delta T_{ad}(T)_{\Delta H}$ are called direct measurements of the magnetocaloric effect. There exists an additional indirect technique involving measurements of heat capacity at constant pressure as a function of temperature in constant magnetic fields. This method provides a complete characterization of the magnetocaloric properties of a solid, because it allows the calculation of both $\Delta S_M(T)_{\Delta H}$ and $\Delta T_{ad}(T)_{\Delta H}$ (Gschneidner, Jr. and Pecharsky, 2000). The technique based on measurements of $C_P(H,T)$ was not applied in the present investigation. Only zero-field heat capacity measurements were performed.

5.3.1 Indirect measurements of the magnetocaloric effect

The isothermal magnetic entropy change, $\Delta S_M(T)_{\Delta H}$, can be determined from measurements of magnetization as a function of the applied magnetic field and temperature. This can be seen from Equation (9), p. 49. For a small temperature change ΔT this equation can be rewritten to give the approximation

$$\Delta S_M(T_{avg})_{\Delta H} \cong -\mu_0 \frac{1}{\Delta T}\int_{H_I}^{H_F}(\sigma(H,T)-\sigma(H,T+\Delta T))_H\, dH\,, \qquad (14)$$

where T_{avg} denotes the average temperature of T and $T+\Delta T$, i.e. $T+\Delta T/2$. The integral in Equation (14) corresponds to the area enclosed between the two isothermal magnetization curves $\sigma(H)$ and $\sigma(H,T+\Delta T)$. Having obtained experimental magnetization curves with discrete external fields separated by ΔH, the calculation of this area is straightforward using numerical integration. Thus, a complete $\Delta S_M(T)_{\Delta H}$ curve can be derived from a series of isothermal magnetization curves obtained at discrete temperatures with an appropriate, i.e. fairly small, temperature interval. This concept is illustrated in Figure 27.

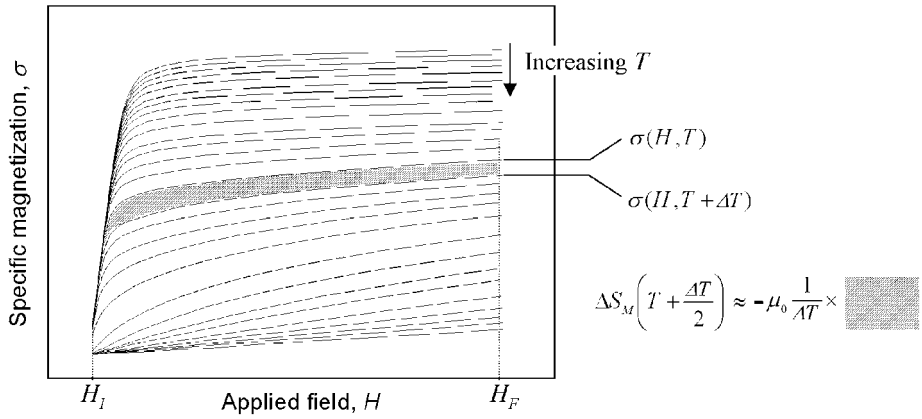

Figure 27. A series of isothermal magnetization curves of a ferromagnetic substance. The area enclosed between the isotherms σ(H,T) and σ(H,T+ΔT) gives the magnetic entropy change for the average temperature T + ΔT/2. The area can be calculated by numerical integration.

Isothermal magnetization curves were obtained using the vibrating-sample magnetometer (cf. Section 4.4). For each member of the $La_{0.67}Ca_{0.33-x}Sr_xMnO_3$ series, the field dependence of the specific magnetization was recorded at fixed temperatures in an appropriate temperature range around the Curie temperature. The interval between the isotherms was 2–3 K, and a complete series typically consisted of about 25–30 magnetization curves. The applied field was varied between the remnant field H_r of the electromagnet ($H_r \approx 10$ kAm^{-1}) and the maximum field H_{max} provided by the magnet (H_{max} = 981 kAm^{-1}). This corresponds to a flux density variation of $B = \mu_0 H = 0.01$–1.23 T. In the following, field changes will usually be given in tesla, i.e. in terms of $\mu_0 H$. Since $H_{max} >> H_r$, the remanent field was neglected and field changes were calculated as $\Delta H = H_{max}$, i.e. H_I and H_F in Equation (14) were set to 0 and H_{max}, respectively. The field direction was not altered between measurements, so possible effects of coercivity were ignored (the coercivity of the samples was on the same order of magnitude as the minimum applied field (H_r), and thus negligible compared to ΔH).

Because calculation of the isothermal magnetic entropy change is based on numerical integration, where the exact differentials $d\sigma$, dT, and dH have been substituted, respectively, by the measured quantities $\Delta\sigma$, ΔT and ΔH, the error associated with $\Delta S_M(T)_{\Delta H}$ values calculated from magnetization data may sum up to be as high as 20–30 % (Gschneidner, Jr. and Pecharsky, 2000). The samples used for magnetization measurements were small pieces of the $La_{0.67}Ca_{0.33-x}Sr_xMnO_3$ compounds. The pieces were irregularly shaped, making it very difficult to determine the demagnetization factors. The lack of demagnetization correction may also contribute to the total error.

5.3.2 Direct measurements of the magnetocaloric effect

Direct measuring of the magnetocaloric effect in terms of the adiabatic temperature change involves measurements of sample temperatures T_I and T_F in an initial magnetic field H_I and a final magnetic field H_F , respectively. The adiabatic temperature change is then determined as the difference $T_F - T_I$. To obtain the temperature dependence of $\Delta T_{ad}(T)_{\Delta H}$, this procedure must be repeated at different initial sample temperatures.

Direct magnetocaloric measurements were carried out as follows (see Figure 28). The sample was placed in the cavity of a sample container made of Teflon®. The purpose of using Teflon® was to obtain a good thermal insulation and thereby near-adiabatic conditions. A small NiCr–Ni (type K) thermocouple was lead trough a hole in the lid of the Teflon container and was placed directly on the sample using thermally conducting grease. An identical thermocouple was placed in the wall of the sample holder without being in contact with the sample. This second thermocouple was used for reference measurements and detection of the possible influence of the magnetic field on the thermocouple voltage. The thermocouples were connected to Prema-5000 voltmeters and data was collected on a computer. The data acquisition program performed the conversion from thermocouple voltage to temperature. The sample holder was placed in a liquid-nitrogen cryostat supplied with a differential temperature controlling system. The cryostat could be tilted, such that the sample was moved in and out of the pole gap of an electromagnet providing a homogeneous field of 557 kAm^{-1} (corresponding to 0.7 T). This way the field could be applied or removed in less than one second. As for the indirect measurements, the remnant field of the electromagnet was small compared to the field change and could be neglected, i.e. $\mu_0 \Delta H = 0.7$ T.

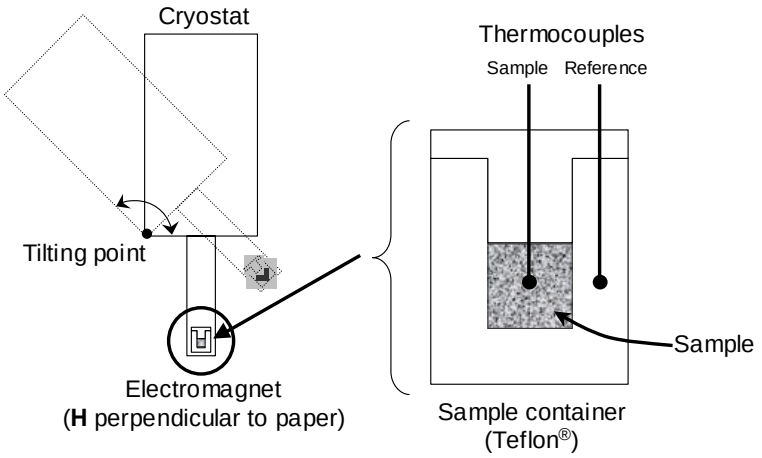

Figure 28. Schematic illustration of the experimental setup used for direct measurements of the adiabatic temperature change, $\Delta T_{ad}(T)_{\Delta H}$. Left) The liquid nitrogen cooled cryostat, which could be tilted, whereby the sample container was moved in and out of the magnetic field induced by an electromagnet. Right) Enlarged view of the sample container and thermocouple mounting.

The insulating properties of the Teflon container were tested by introducing a rapid change of the cryostat temperature and then follow the change of temperature inside the sample holder. A very long response time was observed, indicating that the Teflon® provided a good thermal insulation and hence nearly adiabatic conditions.

The sample was cooled down to the initial measuring temperature (typically about 200 K). The temperature was then increased at a rate of about 0.5 $Kmin^{-1}$ to the final measuring temperature. Every one and a half minute the external magnetic field was applied and the sample was left in the field for about thirty seconds, which was sufficient for a possible temperature change to be detected. Figure 29 shows typical temperature readings for the sample and reference thermocouples during a single magnetization cycle. The adiabatic temperature change is clearly distinguished as a shift of the sample temperature

occurring immediately after the field was applied. Upon removal of the field, the sample temperature drops back to the baseline. Except for small fluctuations associated with field changes, the NiCr–Ni thermocouples appeared to be uninfluenced by the presence of magnetic fields.

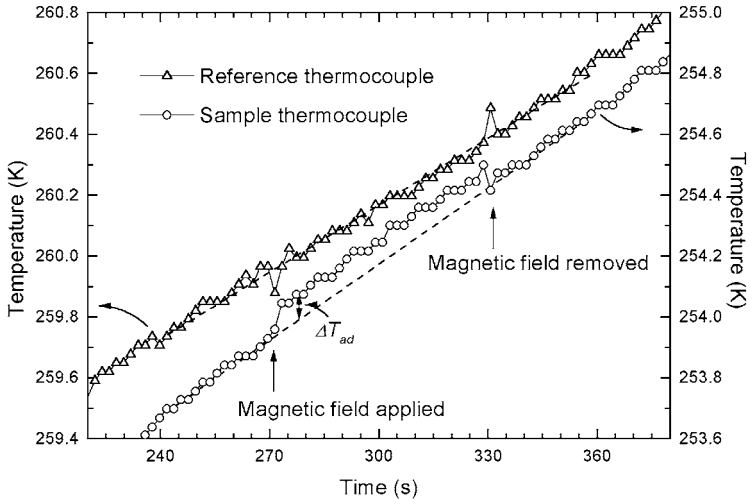

Figure 29. Temperatures recorded by sample and reference thermocouples during a single magnetization sequence. Changes of the magnetic field give rise to a weak noise signal. The adiabatic temperature change of the sample is, however, clearly distinguishable. Note that the reference thermocouple was mounted closer to the outer wall of the sample holder than the sample thermocouple, which explains why the reference temperature is slightly (~0.2 K) higher than the sample temperature.

The accuracy of the direct measuring technique described above depends on the errors in thermometry, the errors in magnetic field setting and the quality of the thermal isolation of the sample. It is rather difficult to quantify the various error contributions and an exact error analysis was not performed. By considering the typical noise in the temperature readings and making reasonable assumptions on the precision in the field setting, the error was estimated to be about 20 % as in the case of the indirect measurements, cf. Section 5.3.1.

5.3.3 Measurements of heat capacity

The specific heat capacity of the $La_{0.67}Ca_{0.33-x}Sr_xMnO_3$ compounds was obtained from differential scanning calorimetry (DSC) measurements conducted on a Seiko DSC-120 instrument. The measurements were carried out at atmospheric pressure and with no external magnetic field. Basically, DSC measures the heat absorbed or released by the sample (in terms of heat flow) as a function of temperature by continuously comparing the temperature of the sample with that of a reference compound. The sample and the reference are contained in small crucibles, which are placed above two very sensitive temperature sensors. For a thorough introduction to the techniques see e.g. Höhne *et al*. (1995).

Determination of C_P required three DSC measurements: 1) a baseline measurement obtained with empty crucibles, 2) a reference measurement, where one of the crucibles contained a reference material, for which $C_P(T)$ was known, and 3) a sample measurement, where the reference material was replaced by the $La_{0.67}Ca_{0.33-x}Sr_xMnO_3$ specimen. The specific heat capacity was then be deduced using the following expression:

$$C_P(T) = \frac{DSC_{ref}(T) - DSC_{base}(T)}{DSC_{sample}(T) - DSC_{base}(T)} \frac{m_{ref}}{m_{sample}} C_{P,ref}(T), \quad (15)$$

where $DSC_{ref}(T)$, $DSC_{base}(T)$, and $DSC_{sample}(T)$ are the DSC signals obtained for the reference compound, the empty crucibles, and the sample, respectively, m_{ref} and m_{sample} denote the mass of the reference compound and the $La_{0.67}Ca_{0.33-x}Sr_xMnO_3$ sample, respectively, and $C_{P,ref}$ is the known specific heat of the reference compound. Silver was used as reference material.

The DSC measurements were performed between about 225 K and 420 K (depending on the Curie temperature of the sample under investigation) with a heating rate of 2 $Kmin^{-1}$. The DSC instrument did not have any build-in cooling facility, so in order to obtain sub-room temperatures the DSC oven was cooled with solid carbon dioxide (dry ice). This non-conventional cooling method caused some disturbance of the very sensitive DSC system. However, based on a comparison with literature data, the obtained results appeared to be reliable.

5.4 Results and discussion

This section gives an overview of the results of the direct and indirect magnetocaloric measurements carried out on the $La_{0.67}Ca_{0.33-x}Sr_xMnO_3$ series. Results of a quantitative comparison between $\Delta T_{ad}(T)_{\Delta H}$ and $\Delta S_M(T)_{\Delta H}$ values are also presented.

5.4.1 Indirect measurements

Figure 30 shows the result of the indirect magnetocaloric measurement carried out for the end-member $La_{0.67}Ca_{0.33}MnO_3$. The complete series of isothermal magnetization curves are shown along with the corresponding calculated magnetic entropy change for two selected values of the magnetic field change, 0.7 T and 1.2 T, respectively.

The Curie temperature of this sample is 267K, cf. Section 4.4. The area enclosed between neighboring isotherms is clearly increasing as the temperature approaches T_C from both ends of the temperature range. Qualitatively this is in very good agreement with thermodynamic considerations made in Section 5.2. The magnetic entropy change, which is negative, increases correspondingly and distinct peaks occur close to the Curie point. For a field change of 1.2 T, a maximum (negative) magnetic entropy change of 5.8 $Jkg^{-1}K^{-1}$ is obtained. The width of the peak at half maximum is about 9 K.

Figure 31 summarizes the results of the indirect measurements of the $La_{0.67}Ca_{0.33-x}Sr_xMnO_3$ series, showing both isothermal magnetization curves and corresponding calculated $\Delta S_M(T)_{\Delta H}$ profiles for field changes of 0.7 and 1.2 T, respectively. For all the samples in the series, the magnetic entropy change exhibits a peak in the vicinity of the Curie temperature. However, the increase of the area between neighboring isotherms near T_C becomes less distinct with increasing x and the maximum magnetic entropy change decreases correspondingly to a more or less constant level of about 1.7 $Jkg^{-1}K^{-1}$ (considering data for $\mu_0\Delta H$ = 1.2 T). The exchange of Ca and Sr also causes an asymmetric broadening of the $\Delta S_M(T)_{\Delta H}$ profiles. This broadening could be an indication of the presence of a distribution of Curie temperatures, probably associated with the surface-near regions of the grains. This possibility will be discussed further in the next chapter. The magnetocaloric peak breath gradually increases with x but settles at about 30 K when x exceeds 0.165.

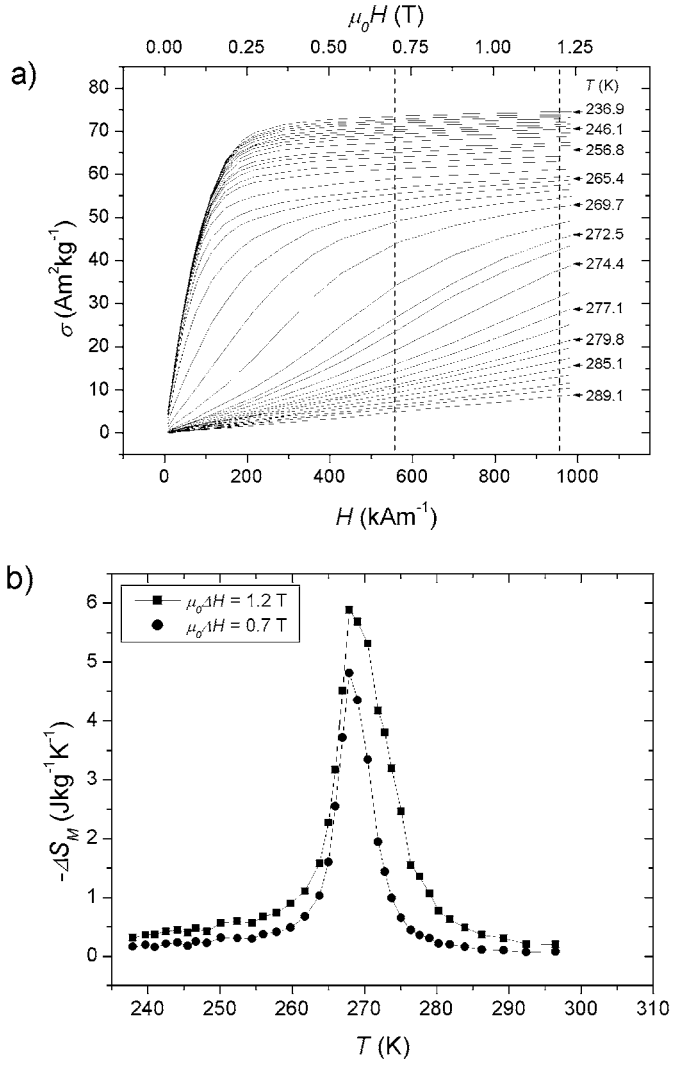

Figure 30. a) Isothermal magnetization curves of the La0.67Ca0.33MnO3 sample. The vertical lines mark maximum field values used for calculation of magnetic entropy changes. b) Isothermal magnetic entropy change of the La0.67Ca0.33MnO3 sample due to field changes of 0.7 T (circles) and 1.2 T (squares), respectively.

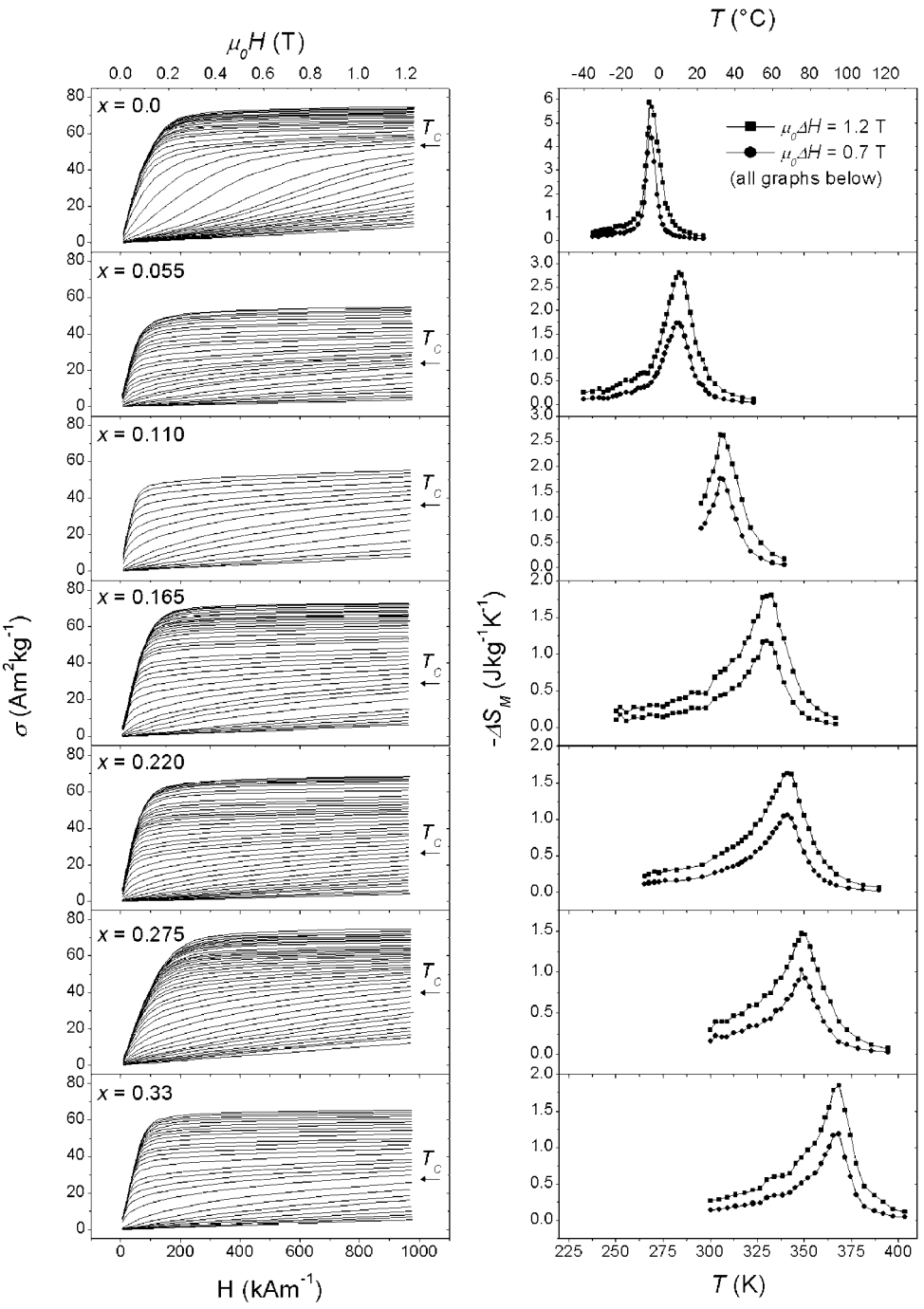

Figure 31. Left panel) Isothermal magnetization curves of the samples in the $La_{0.67}Ca_{0.33-x}Sr_xMnO_3$ series (labeled by their corresponding x value). The arrows mark isotherms obtained near the Curie temperature T_C. Right panel) Corresponding magnetic entropy changes as a function of temperature. $\Delta S_M(T)_{\Delta H}$ has been calculated for $\mu_0 \Delta H$ = 0.7 and 1.2 T, respectively.

5.4.2 Direct measurements

The raw data of the direct magnetocaloric measurements consisted of temperature-versus-time profiles like the one shown for the $La_{0.67}Ca_{0.33}MnO_3$ sample in Figure 32 (a). Each step on the temperature curve is associated with magnetization and subsequent demagnetization of the sample. The height of the step determines the adiabatic temperature change for the temperature, at which the external field was applied. The steps superimpose the steadily increasing "background" temperature controlled by the cryostat system. (The increasing background temperature provided the variation of the initial sample temperature.) The step height, and thus the adiabatic temperature change, increased significantly as the temperature approached the Curie temperature of the sample (267 K). Above T_C the temperature change decreased. Qualitatively, this consists very well with theory; cf. Figure 26 (p. 50).

A single magnetization cycle has been outlined and is shown in an enlarged view in Figure 32 (b). The field was applied when the sample temperature was 266.4 K, as indicated by the horizontal arrow labeled T_I. The temperature immediately started to increase and after about ten seconds it stabilized at $T_F \approx 267.9$, also indicated by a horizontal arrow. To compensate for the increase of the background temperature during temperature stabilization, T_F was determined by back-extrapolating from the data points obtained after stabilization to the point where the field was applied. The adiabatic temperature change was calculated from $\Delta T_{ad}(T_I) = T_F - T_I$ with the result ΔT_{ad} (266.4 K) = 1.44 K.

The decrease of temperature upon the subsequent removal of the field is slightly larger (~1.5 K). This is most likely because the removal of the field took place closer to the Curie temperature (due to the increasing background temperature). For magnetization cycles performed above T_C this is opposite and the temperature changes associated with magnetization are smaller than the temperature change upon the subsequent demagnetization.

Each magnetization cycle was analyzed as described above to obtain a complete $\Delta T_{ad}(T)_{\Delta H}$ profile. The result for the $La_{0.67}Ca_{0.33}MnO_3$ sample is shown in Figure 32 (c). Like the magnetic entropy change, the adiabatic temperature change shows a distinct peak around the Curie temperature (compare with Figure 30 (b), p. 55). The maximum $\Delta T_{ad}(T)_{\Delta H = 0.7\ \mathrm{T}}$ value is 1.5 K and the maximum occurs for T = 267 K, i.e. very close to T_C.

The upper panel in Figure 33 shows the complete result of the direct measurement of the adiabatic temperature change in the $La_{0.67}Ca_{0.33-x}Sr_xMnO_3$ series. In order not to damage the experimental apparatus the temperature measurements were terminated at about 370 K, for which reason the $\Delta T_{ad}(T)_{\Delta H}$ peak of the $La_{0.67}Sr_{0.33}MnO_3$ sample is incomplete. For comparison the isothermal magnetic entropy changes calculated for $\mu_0 \Delta H$ = 0.7 T are also shown in Figure 33. Taking into consideration the rather large experimental errors associated with both direct and indirect magnetocaloric measurements, cf. Sections 5.3.1 and 5.3.2, the results show a high degree of conformity. In both experiments the magnetocaloric peak of the $La_{0.67}Ca_{0.33}MnO_3$ sample is sharp and intense, while an increasing Sr content leads to broader and more asymmetric peaks with a lower maximum value. All peaks are centered near the Curie temperature of the corresponding $La_{0.67}Ca_{0.33-x}Sr_xMnO_3$ compound.

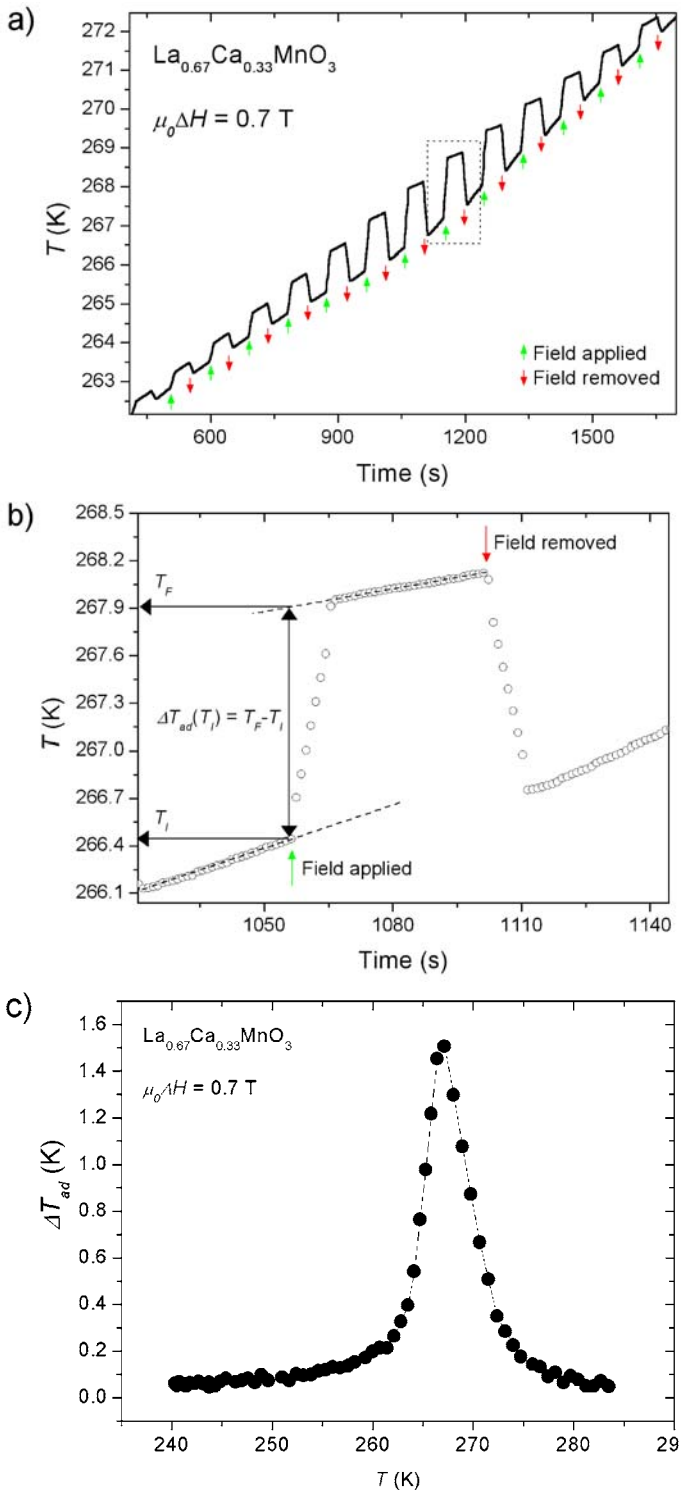

Figure 32. a) Temperature profile for the $La_{0.67}Ca_{0.33}MnO_3$ compound obtained during a direct measurement of the adiabatic temperature change. b) Enlarged view of the magnetization cycle outlined in panel (a). The adiabatic temperature change was determined as indicated. c) Adiabatic temperature change as a function of temperature as obtained from the temperature profile in panel (a).

The decreasing magnetocaloric effect arising from increasing Sr content is related to the increased broadening of the ferromagnetic transition. In Section 4.5.1 it was shown that the sharpness of the ferromagnetic transition in the $La_{0.67}Ca_{0.33-x}Sr_xMnO_3$ system decreases systematically with increasing *x,* cf. Figure 23. The broadening of the Curie transition was ascribed to the decreasing grain size associated with the increasing Sr content. The very sharp transition observed for the samples with low Sr content, especially $La_{0.67}Ca_{0.33}MnO_3$, could also be related to dynamic Jahn-Teller effect. It is obvious that a broadening of the ferromagnetic transition causes a decrease of the maximum isothermal magnetic entropy change because $\Delta S_M(T)_{\Delta H}$ is determined directly from $\partial\sigma/\partial T$, cf. Equation (9). For the adiabatic temperature change the relationship is less obvious because the expression for $\Delta T_{ad}(T)_{\Delta H}$ involves the heat capacity, cf. Equation (8), which may change dramatically at the Curie point (see below).

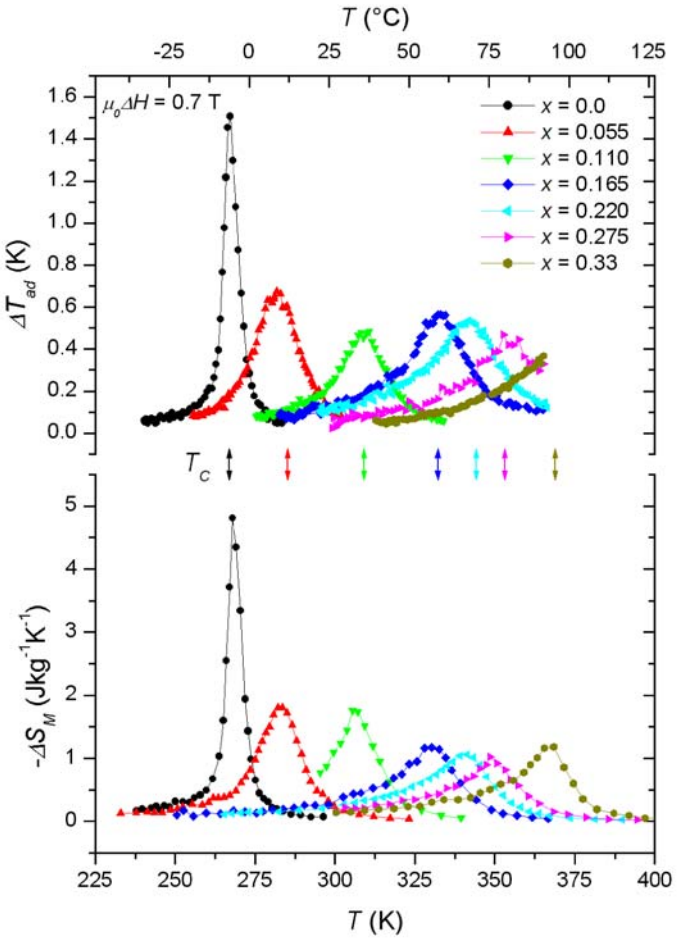

Figure 33. Adiabatic temperature change (top panel) and isothermal magnetic entropy change (bottom panel) for the $La_{0.67}Ca_{0.33-x}Sr_xMnO_3$ series obtained with field change $\mu_0\Delta H$ = 0.7 T. Curie temperatures are indicated by double-arrows.

The above results are very interesting because they show that both crystallographic and micro-structural properties of the manganites play an important role to the magnetocaloric effect. For instance, it is possible that improving the sintering properties, e.g. by applying long-term heat treatment, could enhance the magnetocaloric properties.

It is also interesting to see that the $La_{0.67}Ca_{0.33-x}Sr_xMnO_3$ compounds do in fact exhibit a significant magnetocaloric effect near room temperature. The possible application of this effect in magnetic refrigeration devices will be discussed further in Section 5.6 below.

5.4.3 Comparison between $\Delta S_M(T)_{\Delta H}$ and $\Delta T_{ad}(T)_{\Delta H}$

A quantitative comparison between the results of the direct and the indirect measurements was carried out employing results of heat capacity measurements. Such a comparison is interesting because it can be considered as a test of the reliability of the results obtained by the two different measuring techniques.

Figure 34 shows the temperature dependence of the zero-field heat capacity of the $La_{0.67}Ca_{0.33-x}Sr_xMnO_3$ samples. For all the compounds C_P increases with increasing temperature to a point just below T_C and then rather suddenly decreases. This anomaly can be attributed to the ferromagnetic transition, which causes a dramatic change of the heat capacity of the spin system. In addition to the ferromagnetic transition, the materials simultaneously undergo a transition from a conducting to an insulating (or semiconducting) state (cf. Section 2.4). Variations of the internal energy due to this transition could also contribute to the heat capacity anomaly. The heat capacity peaks superimpose a base level of about 500 $Jkg^{-1}K^{-1}$, which can be ascribed mainly to the electronic and lattice heat capacities.

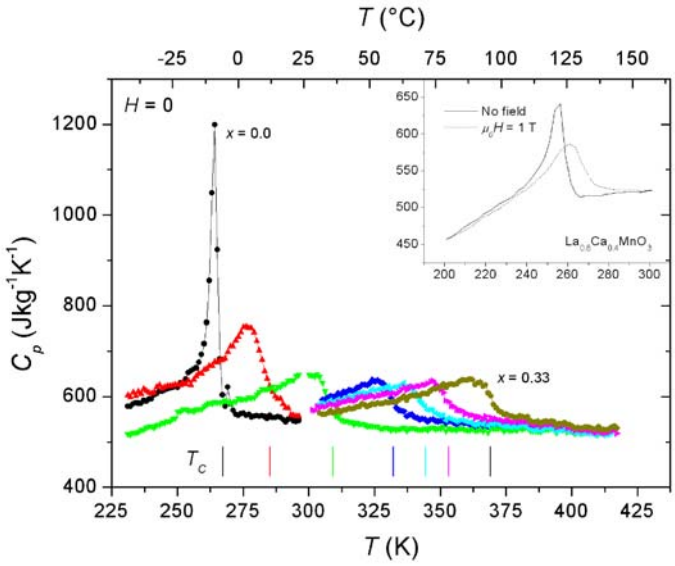

Figure 34. Heat capacity of the $La_{0.67}Ca_{0.33-x}Sr_xMnO_3$ samples as a function of temperature. The Curie temperatures of the samples are indicated. Color and symbol designations are the same as in Figure 33. The inset shows heat capacity as a function of temperature on zero field and in a field of 1T of a $La_{0.6}Ca_{0.4}MnO_3$ sample with T_C = 260 K (adopted from Bohigas et al. (2000)).

The adiabatic temperature change and the isothermal magnetic entropy change are related through the approximate expression given in Equation (13), p. 49, which involves the term $C(T)_{P,H_F}$, i.e. the heat capacity in the final magnetic field. In this investigation

the heat capacity measurements were carried out in zero magnetic field and Equation (13) could only be used assuming that the influence of a magnetic field on the heat capacity would be negligible. In principle, this assertion is only valid for temperatures far below or far above the Curie point: From thermodynamics, the field dependence of the magnetic contribution to the specific heat is given (Roy *et al*., 2000) by

$$\left(\frac{\partial C_{P,H}}{\partial H}\right)_T = \mu_0 T\left(\frac{\partial^2 M}{\partial T^2}\right)_H, \tag{16}$$

where M is the magnetization. Thus, far from the Curie point, where the magnetization shows only little variation with temperature regardless of the field, the magnetic heat capacity is vanishing. Near T_C, however, the magnetic heat capacity may be strongly affected by external fields. Using Equation (13) with the zero-field heat capacity is therefore basically wrong, but on the other hand the rather moderate magnetic fields used for the magnetocaloric measurements in the present investigation should allow for a rough comparison between $\Delta S_M(T)_{\Delta H}$ and $\Delta T_{ad}(T)_{\Delta H}$ using the approximation |

$$\left|\Delta S_M(T)_{\Delta H}\right| \cong \frac{C_{P,H=0}}{T}\Delta T_{ad}(T)_{\Delta H}, \tag{17}$$

This equation was used to calculate a theoretical value for maximum magnetic entropy change, $\left|\Delta S_M^{\max}\right|$, based on the observed heat capacity and the observed maximum adiabatic temperature change $\Delta T_{ad}^{\max}$. An appropriate choice was made for the heat capacity value based on a review of previous results on the temperature and field dependence of the heat capacity in lanthanum manganites: The inset in Figure 34 shows the heat capacity of a $La_{0.6}Ca_{0.4}MnO_3$ sample in zero magnetic field and in an applied field of 1 T (data obtained from Bohigas *et al*. (2000)). At the Curie temperature, which is 260 K for this compound, the heat capacity in the applied field is about 50 % of the maximum zero-field heat capacity (compared to the flat base level above T_C). Since the applied magnetic field in the present investigation was of the same order of magnitude, corresponding heat capacity values were used for the $La_{0.67}Ca_{0.33-x}Sr_xMnO_3$ series, e.g. 860 $Jkg^{-1}K^{-1}$ for the x = 0 sample. Using the heat capacity value C_P^*, a theoretical value $\left|\Delta S_M^{calc}\right|$ for the maximum magnetic entropy change could be calculated and compared with the $\left|\Delta S_M^{\max}\right|$ value obtained experimentally. From Equation (17),

$$\left|\Delta S_M^{calc}\right| = \frac{C_P^*}{T_C}\Delta T_{ad}^{\max}. \tag{18}$$

Table 6 lists the values used for the calculations and compares the calculated magnetic entropy changes with the corresponding observed values. In view of the experimental errors and the fact that the calculated values are based on rather rough estimates of heat capacity, the observed and calculated magnetic entropy change values are fairly consistent. For the $La_{0.67}Ca_{0.33}MnO_3$ sample the values are equivalent. For the remaining samples the values differ by 11–20 %, except for the $La_{0.67}Ca_{0.220}Sr_{0.110}MnO_3$ sample, for which the error is 40 %. It is difficult to identify the cause for this rather large error. From Figure 33 it seems that the measured adiabatic temperature change is too low. This could be due to a poor thermal contact between the sample and the thermocouple.

Table 6. Comparison of theoretical and experimental maximum magnetic entropy changes for the samples in the $La_{0.67}Ca_{0.33-x}Sr_xMnO_3$ series. The table shows the Curie temperature, T_C, the heat capacity at 50 % of the peak value compared to the base level, C_P^*, the maximum observed adiabatic temperature change $\Delta T_{ad}^{\max}$, the maximum observed magnetic entropy change $\left|\Delta S_M^{\max}\right|$, the calculated magnetic entropy change $\left|\Delta S_M^{calc}\right|$, and the relative deviation between the calculated and measured entropy change. Experimental values were obtained with an applied field of 0.7 T.

	Observed values			Calculated values		
Sample	T_C	C_P^*	$\Delta T_{ad}^{\max}$	$\left\|\Delta S_M^{\max}\right\|$	$\left\|\Delta S_M^{calc}\right\|$	Deviation
x	K	$Jkg^{-1}K^{-1}$	K	$Jkg^{-1}K^{-1}$	$Jkg^{-1}K^{-1}$	%
0	267	860	1.50	4.8	4.8	0
0.055	285	650	0.70	1.8	1.6	11
0.110	309	590	0.50	1.7	1.0	40
0.165	332	580	0.55	1.2	1.0	17
0.220	344	575	0.55	1.1	0.9	18
0.275	353	580	0.50	1.0	0.8	20
0.33	369	585	-	1.2	-	-

5.5 Modeling of the magnetocaloric effect

A physical model for the magnetocaloric properties of the $La_{0.67}Ca_{0.33-x}Sr_xMnO_3$ series was established. The model was based on Weiss molecular mean field theory for ferromagnetic interaction, the Debye theory for lattice heat capacity and the classical Sommerfeld theory for conduction electron heat capacity as outlined below. These are well-established theories treated in various textbooks on magnetism and the physical properties of solids. For an introduction to the mean field theory see e.g. Morrish (1965) or Smart (1966). The Debye model for the heat capacity associated with lattice vibrations and the Sommerfeld theory for the thermal properties of conduction electrons are treated for instance in Ashcroft and Mermin (1976). Here, the classical expressions have been adapted to comply with the SI unit system.

5.5.1 The model

In the classical mean field theory the specific magnetization is given by

$$\sigma(T,H) = \sigma_0 B_J(\alpha) = n_s g J B_J(\alpha), \tag{19}$$

where σ_0 is the saturation magnetization, n_s the number of magnetic spins per unit mass, g the Landé factor, J the total angular momentum, μ_B the Bohr magneton, and $B_J(\alpha)$ the Brillouin function defined by

$$B_J(\alpha) = \frac{2J+1}{2J}\coth\left(\frac{2J+1}{2J}\alpha\right) - \frac{1}{2J}\coth\left(\frac{1}{2J}\alpha\right). \tag{20}$$

The argument α is the solution to the simultaneous equations

$$\begin{aligned} \gamma &= B_J(\alpha) \\ \alpha &= \frac{gJ\mu_B\mu_0 H}{k_B T} + \frac{3T_C J}{T(J+1)}\gamma \end{aligned}, \tag{21}$$

where k_B is the Boltzmann constant and γ is the reduced magnetization ($\gamma = \sigma/\sigma_0$). The solution to this set of equations can be found by iteration.

Values were assigned to the parameters entering into these equations as follows: The number of spins per unit mass was derived from the nominal sample compositions. The samples contained one Mn ion per formula unit and from this, $n_s \approx 2.8 \cdot 10^{24}$ kg^{-1}. The Landé factor was assumed to be 2. The *d* shells of Mn^{3+} and Mn^{4+} constitute total spins of 2 and 3/2, respectively. The total average angular momentum arising from these spins was calculated from the nominal Mn^{3+}/Mn^{4+} ratio (67/33), resulting in $J = 1.83$. The only empirical parameter was T_C, for which the experimental values listed in Table 6 were used.

Figure 35 shows the temperature dependence of the specific magnetization obtained using the above-mentioned parameter values and T_C = 300 K. $\sigma(T,H)$ was calculated for zero applied field and for the field values corresponding to those used in the direct and indirect measurements described above (0.7 and 1.2 T, respectively). An external field tends to smear out the sharp drop in magnetization at T_C. This is because the field tends to suppress the transition from ferromagnetism to paramagnetism by aligning spins that would otherwise be fluctuating randomly due to thermal excitations in the paramagnetic regime.

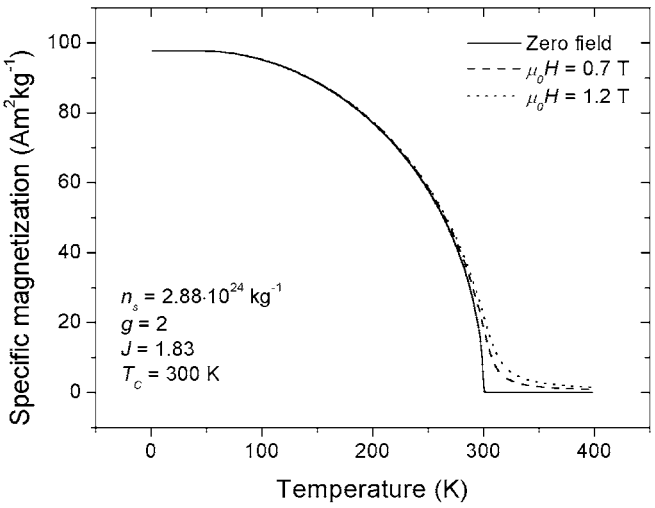

Figure 35. Temperature dependence of specific magnetization in zero magnetic field (solid line) and in applied fields of 0.7 T (dashed line) and 1.2 T (dotted line) calculated by the mean field model. Parameter values used for calculations are indicated.

The specific heat capacity was assumed to be the sum of three contributions: the magnetic heat capacity C_M, the lattice heat capacity C_L and the conduction electron heat capacity C_E. Expressions for the three quantities are derived below (details can be found in the textbook references given above (p. 62).

The contribution of the magnetization to the internal energy is given by

$$U_M = -\mu_0 \int H_{tot} d\sigma \,, \tag{22}$$

where H_{tot} is the sum of the external magnetic field H and the internal mean field H_{int}. By convention, the internal field is assumed to be proportional to the magnetization:

$$\mu_0 H_{\text{int}} = N_{\text{int}} \sigma, \tag{23}$$

where N_{int} is the mean field constant,

$$N_{\text{int}} = \frac{3k_B T}{n_s g^2 \mu_B^2 J(J+1)} \,. \tag{24}$$

By definition, the magnetic contribution to the specific heat capacity C_M is given by $\partial U_M / \partial T$. Thus, from Equations (22), (23), and (24)

$$C_M = -\mu_0 H \frac{\partial \sigma}{\partial T} - \frac{1}{2} N_{\text{int}} \frac{\partial \sigma^2}{\partial T} \,. \tag{25}$$

The heat capacity associated with lattice vibrations, C_L, were calculated using the Debye model,

$$C_L = 9nk_B \left(\frac{T}{\Theta_D} \right)^3 \int_0^{\Theta_D / T} \frac{x^4 e^x}{(e^x - 1)^2} dx \,, \tag{26}$$

where n is the number of atoms per unit mass and Θ_D is the Debye temperature. The nominal compositions were used to derive values for n. The Debye temperature was assumed to be 353 K based on data for polycrystalline $La_{0.7}Sr_{0.3}MnO_3$ (Coey *et al*., 1995).

In the Sommerfeld theory of conduction in metals, the free electron contribution to the specific heat capacity is given by

$$C_E = \gamma_e n_e T \,, \tag{27}$$

where γ_e is a constant, which is proportional to the density of electronic levels at the Fermi level, and n_e is the number of conduction electrons per unit mass. The value of γ_e was taken to be 5.6 $mJmole^{-1}K^2$, which is the average of γ_e values reported by Coey *et al*. (1995) for $La_{0.7}Ca_{0.3}MnO_3$ and $La_{0.7}Sr_{0.3}MnO_3$, respectively. The carrier density was derived from the nominal sample composition considering that Mn^{3+} has one mobile e_g electron, whereas Mn^{4+} has none. With 0.67 carriers per formula unit, n_e becomes $\sim 1.9 \cdot 10^{24}$ kg^{-1}.

Figure 36 shows the specific heat capacity as calculated by means of the combined mean field, Debye and Sommerfeld model using the parameter assignments mentioned above and a T_C value of 300 K. For comparison, the three heat capacity contributions are plotted separately. The lattice contribution is dominating but is clearly superimposed by the magnetic heat capacity, which shows a distinct anomaly at the Curie point. At high tem-

peratures the electronic heat capacity is vanishing compared to the other two contributions. The effect of applying magnetic fields (0.7 T and 1.2 T) is indicated. As for the magnetization, an external field is seen to cause a smearing around T_C. This is clearly related to the suppression of the ferromagnetic transition caused by the field (cf. Figure 35, p.63).

It is noteworthy that the calculated specific heat capacity, which except for the Debye and Curie temperatures is based on theoretical values for the $La_{0.67}Ca_{0.33-x}Sr_xMnO_3$ system, shows a high-temperature value about 575 $Jkg^{-1}K^{-1}$, which is slightly overestimated but still in very good agreement with the observed heat capacity.

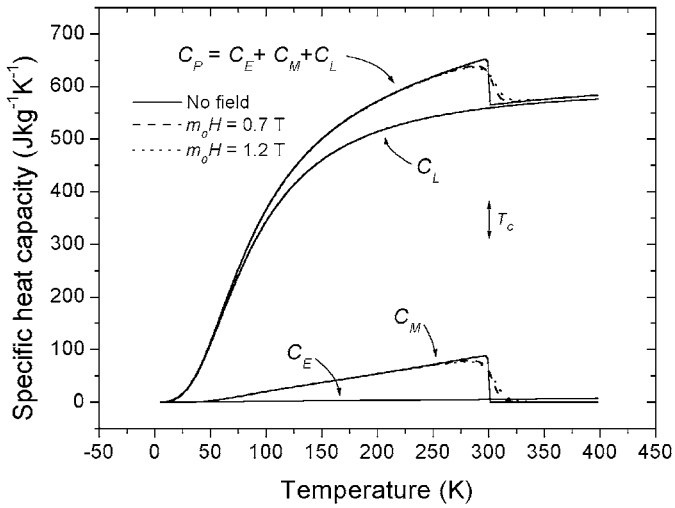

Figure 36. Specific heat capacity as a function of temperature calculated for a $La_{0.67}Ca_{0.33-x}Sr_xMnO_3$ compound with T_C = 300 K. The electronic, magnetic, and lattice heat capacities are plotted separately (curves labeled C_E, C_M, and C_L, respectively) along with their sum (denoted C_P). The heat capacity was calculated for zero external field (solid lines) and for applied fields of 0.7 T (dashed lines) and 1.2 T (dotted lines), respectively.

Using the expressions above, the magnetization and the heat capacity could be calculated for any given temperature and any given applied magnetic field. In combination with the magnetocaloric relations derived from classical thermodynamics in Section 5.2 this allowed for calculation of theoretical values for the isothermal magnetic entropy change and the adiabatic temperature change. (One could enter the above expressions for σ and $C_{P,H}$ into the thermodynamic relations to arrive at final theoretical expression for $\Delta S_M(T)_{\Delta H}$ and $\Delta T_{ad}(T)_{\Delta H}$, but since the calculations eventually were carried out numerically this was unnecessary.)

5.5.2 Comparison of theory with experiment

A comparison of the theoretical model with experimental data is presented in Figure 37 showing observed and calculated isothermal magnetic entropy changes, heat capacities and adiabatic temperature changes for all the samples in the $La_{0.67}Ca_{0.33-x}Sr_xMnO_3$ series. $\Delta S_M(T)_{\Delta H}$ and $\Delta T_{ad}(T)_{\Delta H}$ are shown for $\mu_0\Delta H$ = 0.7 T, while $C_P(T)$ is shown for zero external field. Figure 38 shows theoretical and experimental magnetic entropy changes for field changes of $\mu_0\Delta H$ = 0.7 and 1.2 T, respectively (selected samples only).

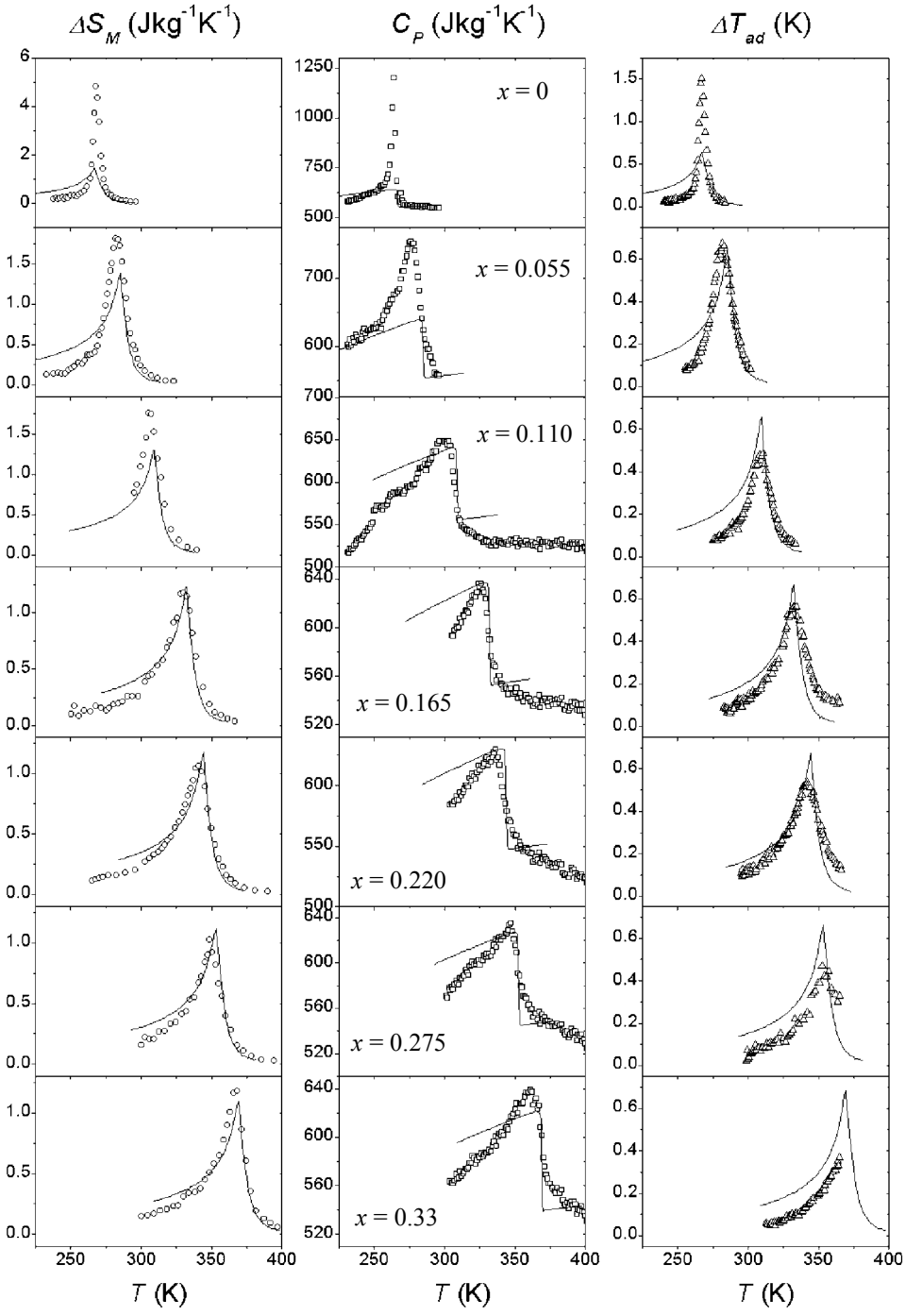

Figure 37. Temperature dependence of the isothermal magnetic entropy change, the zero-field heat capacity, and the adiabatic temperature change for the $La_{0.67}Ca_{0.33-x}Sr_xMnO_3$ series. Data points are observed values, while solid lines represent model calculations. $\Delta S_M(T)_{\Delta H}$ and $\Delta T_{ad}(T)_{\Delta H}$ values are for a field change of 0.7 T.

For the $La_{0.67}Ca_{0.33}MnO_3$ sample there is a relatively poor consistency between theory and experiment. Both the maximum magnetic entropy change and the maximum adiabatic temperature change are underestimated by approximately a factor of three. The model description of the zero-field heat capacity anomaly is also inadequate. The disagreement between theory and experiment arises from the fact that the mean field model fail to explain the very sharp ferromagnetic transition. For the samples with $x > 0$, and especially the rhombohedral phases ($x \geq 0.165$), the agreement between theory and experiment improves significantly.

There is a good accordance between calculated and observed maximum values for both $\Delta S_M(T)_{\Delta H}$ and $\Delta T_{ad}(T)_{\Delta H}$. The model consistently overestimates the magnetocaloric effect below the Curie point, but theoretical and experimental FWHM values for the magnetocaloric peaks are in quite good agreement. The model also gives adequately predicts the heat capacity anomaly related to the transition from ferromagnetism to paramagnetism at T_C. Finally, the model seems to allow for reliable predictions of the dependence of the magnetocaloric effect on the change of the external field, see Figure 38.

Altogether the consistency between calculated and observed magnetocaloric effects is satisfactory. In spite of its simplicity, the model can be regarded a useful tool for prediction of the cooling capacities obtainable for various types of magnetic refrigeration cycles and different external magnetic field strengths.

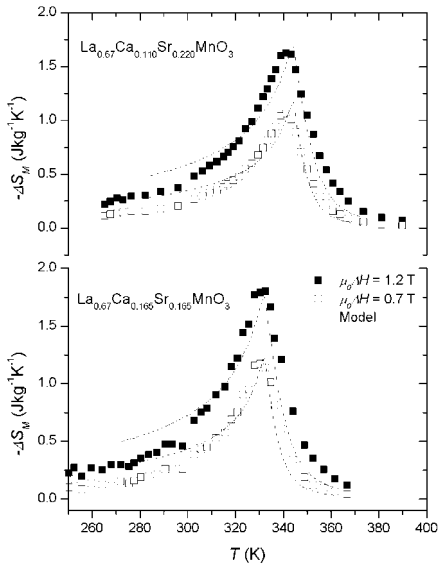

Figure 38. Observed and calculated isothermal magnetic entropy changes for $La_{0.67}Ca_{0.165}Sr_{0.165}MnO_3$ and $La_{0.67}Ca_{0.110}Sr_{0.220}MnO_3$ for field changes of 0.7 T (open symbols) and 1.2 T (closed symbols). Data points (squares) show experimental data, while solid lines represent the theoretical model.

5.6 Application of $La_{0.67}Ca_{0.33-x}Sr_xMnO_3$ in magnetic refrigeration

So far, the magnetocaloric properties of the $La_{0.67}Ca_{0.33-x}Sr_xMnO_3$ samples have been considered from a rather phenomelogical point of view. In this section the practical application of these materials in magnetic refrigeration will be discussed.

The lanthanide gadolinium (Gd) is considered the prototypical material for magnetic refrigeration at ambient conditions because it exhibits a substantial magnetocaloric effect near room temperature. The material has a large total angular moment (7/2) and a Curie transition at $T_C \approx 293$K (Benford and Brown, 1981). Gadolinium has been used as working substance in several proof-of-principle magnetic refrigerators: Brown (1976) obtained a temperature difference of 46 K between the hot and cold end of a simple refrigerator using 1 mole (~158 g) of gadolinium and an applied field of 7 T. Pecharsky and Gschneidner, Jr. (1999) have constructed a cooling machine generating 600 W of cooling power in a 5 T field using 3 kg gadolinium as refrigerant. Recently, Bohigas and coworkers (2000) presented a magnetic refrigerator based on permanent magnets. The refrigerator produced a temperature difference of 1.6 K between hot and cold fluid chambers with an external field of just 0.3 T.

Other materials have been suggested as refrigerants for room temperature magnetic refrigeration. A very recent example is the transition-metal based alloy $MnFeP_{0.45}As_{0.55}$, which shows a Curie temperature of 300 K and exhibits a very large magnetocaloric effect exceeding that of gadolinium (Tegus *et al*., 2002; Brück *et al*., *in press*). Fairly large magnetocaloric effects near room temperature have also been found in $La(Fe,Co)_{11.83}Al_{1.17}$ compounds (Hu *et al*., 2001). However, to the knowledge of the present author, gadolinium is the only material, which has been used in proof-of-principle room temperature refrigerators. A comparison of the magnetocaloric properties of the $La_{0.67}Ca_{0.33-x}Sr_xMnO_3$ samples with those of gadolinium is therefore interesting.

Figure 39 shows the temperature dependence of the magnetic entropy change of gadolinium plotted together with the $\Delta S_M(T)_{\Delta H}$ profiles obtained for the $La_{0.67}Ca_{0.33-x}Sr_xMnO_3$ compounds with $\mu_0\Delta H = 1.2$ T. Data for gadolinium was obtained from Zhou *et al*. (1999). It ought to be mentioned that the $\Delta S_M(T)_{\Delta H}$ curve for gadolinium was constructed by linear extrapolation because the original data were obtained with a maximum field of 1.5 T. In fact, for applied fields up to about 4 T, the magnetic entropy change in Gadolinium does increase linearly with temperature (Gschneidner, Jr. and Pecharsky, 2000) (at least near T_C), so the error associated with the extrapolation is irrelevant for the present comparison. Considering the maximum magnetic entropy change, the values obtained for the $La_{0.67}Ca_{0.33-x}Sr_xMnO_3$ samples with $x \leq 0.110$ are indeed competitive with that of gadolinium. For the $x = 0$ sample, the maximum magnetic entropy change exceeds the maximum $|\Delta S_M(T)_{\Delta H}|$ value of gadolinium by a factor of 1.7. The samples with $x = 0.055$ and 0.110 show a maximum magnetic entropy change which is close to the gadolinium value. The rhombohedral phases, however, cannot compete with gadolinium in terms of maximum $|\Delta S_M(T)_{\Delta H}|$.

Apart from the maximum magnetic entropy change the width of the $\Delta S_M(T)_{\Delta H}$ peak is a very important parameter with respect to magnetic refrigeration. As for any cooling device, the purpose of a magnetic refrigerator is to transfer heat from a cold reservoir (the heat load) to a hot reservoir (the heat sink). The cooling power of a magnetic refrigerant can be defined as the amount of heat, which the material is capable of absorbing from the heat load and subsequently rejecting to the heat sink in a single thermodynamic cooling cycle.

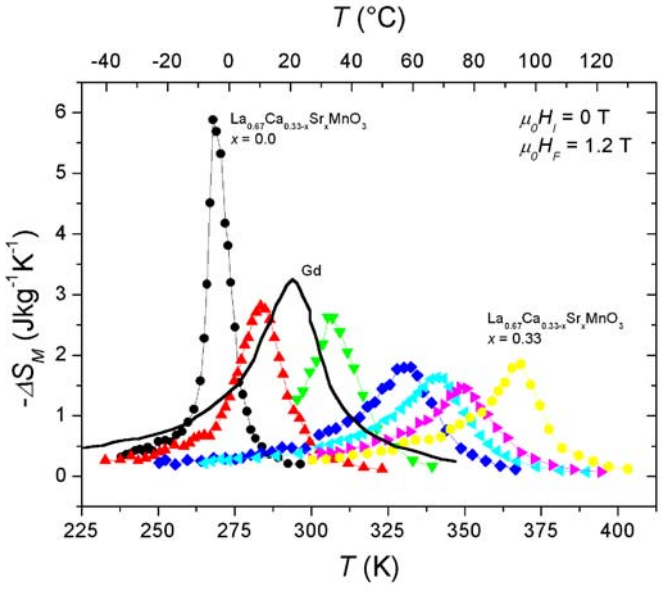

Figure 39. Comparison of the temperature dependence of the magnetic entropy changes in $La_{0.67}Ca_{0.33-x}Sr_xMnO_3$ produced upon application of an external field of 1.2 T with the magnetic entropy change in gadolinium. Data for gadolinium was obtained from (Zhou et al., 1999) and extrapolated to apply to a field change of 1.2 T (original data was obtained for $\mu_0\Delta H = 1.5$ T).

Figure 40 shows a schematic entropy-temperature (*S*–*T*) diagram of a ferromagnetic material. The diagram shows the temperature dependence of the total entropy of the substance in an initial magnetic field $H_I = 0$ and in a final magnetic field H_F .

For a given temperature, the vertical distance between such isofield curves correspondents to the magnetic entropy change, while the horizontal distance correspondents to the adiabatic temperature change, cf. Figure 25. The paths A→B, B→C, C→D, and D→A indicate processes involved in an ideal magnetic cooling cycle. A cycle like this, consisting of two isothermal and two isofield processes, is known as a magnetic Stirling cycle and it can be realized in practice (Brown, 1976).

Along the path C→D the magnetic refrigerant is demagnetized isothermally, i.e. a thermal contact is enforced between the material and the cold reservoir (the load). The amount of heat absorbed from the load is given by $Q_L = T_L \Delta S_M(T_L)_{\Delta H}$ (Smaïli and Chahine, 1997). Similarly, an amount of heat rejected to hot reservoir during the isothermal magnetization process A→B is given by $Q_S = T_S \Delta S_M(T_S)_{\Delta H}$ (*ibid.*). From the S–T diagram it is obvious that a good magnetic refrigerant is a material exhibiting a large magnetocaloric effect over a wide range of temperatures. For materials showing a "caret-like" $\Delta S_M(T)_{\Delta H}$ profile, like for instance gadolinium and for instance and $La_{0.67}Ca_{0.220}Sr_{0.110}MnO_3$, the optimum trade-off between the magnetic entropy change

and the temperature span between heat load and heat sink is obtained somewhere around the full width at half maximum. The $La_{0.67}Ca_{0.33}MnO_3$ sample shows a very large magnetic entropy change, but the FWHM of the magnetocaloric peak is only about 8 K (with $\mu_0\Delta H$ = 1.2 T). Although a large applied field would tend to broaden the peak, the material would hardly be applicable to refrigeration at room temperature. The $\Delta S_M(T)_{\Delta H}$ peak of $La_{0.67}Ca_{0.220}Sr_{0.110}MnO_3$ has a width of about 18 K (also with $\mu_0\Delta H$ = 1.2 T), which seems more promising with regard to the practical application at ambient conditions. Still, however, none of the ceramic samples can compete with the width gadolinium showing a magnetocaloric peak with a FWHM of about 27 K for a field change of 1.2 T.

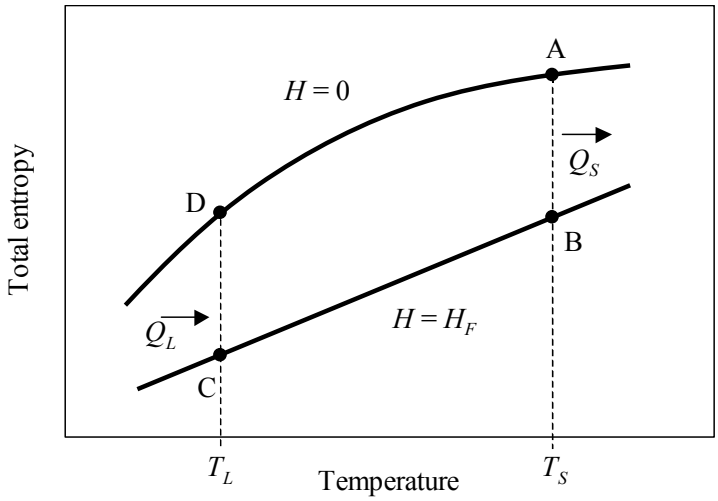

Figure 40. Schematic S–T diagram for a ferromagnetic substance showing the total entropy as a function of temperature with and without an external field. ABCDA defines an ideal magnetic Stirling refrigeration cycle. The cycle involves absorption of a heat amount Q_L from a load at temperature T_L and rejection of a heat amount Q_S sink at temperature T_S.

According to the empirical relation between the composition parameter x and the Curie temperature derived in Section 4.4 a compound with composition $La_{0.67}Ca_{0.27}Sr_{0.06}MnO_3$ would have a Curie temperature near 293 K like gadolinium. Figure 39 suggest that this material would exhibit a maximum magnetic entropy change almost equivalent to the maximum magnetic entropy change of gadolinium. The FWHM of the magnetocaloric peak would probably be about 20 K. This compound could be considered a possible candidate as working substance in future cooling technology based on the magnetocaloric effect.

5.7 Summary and conclusion

The magnetocaloric properties of the samples in the $La_{0.67}Ca_{0.33-x}Sr_xMnO_3$ series were investigated by means of direct and indirect measurements, providing the temperature dependence of the adiabatic temperature change $\Delta T_{ad}(T)_{\Delta H}$ and the isothermal magnetic entropy change $\Delta S_M(T)_{\Delta H}$, respectively. Both $\Delta T_{ad}(T)_{\Delta H}$ and $\Delta S_M(T)_{\Delta H}$ showed distinct peaks around the Curie temperature. The observed maximum $|\Delta S_M(T)_{\Delta H}|$ and $\Delta T_{ad}(T)_{\Delta H}$ values obtained with a field change of 0.7 T were compared quantitatively using zero-field heat capacity data and an approximate thermodynamic relation. The results were found to be in good accordance.

A theoretical model for the magnetocaloric effect in the $La_{0.67}Ca_{0.33-x}Sr_xMnO_3$ system was established. The model provided reasonable predictions of the magnetocaloric properties of the samples. However, the model could not reproduce the very large magnetocaloric effect observed for the $La_{0.67}Ca_{0.33}MnO_3$ compound.

The magnetic entropy changes of the samples were compared to the magnetic entropy change in gadolinium, which is the prototypical material for room temperature magnetic refrigeration. The maximum magnetic entropy change of the $La_{0.67}Ca_{0.33}MnO_3$ sample exceeded that of gadolinium by a factor of 1.7. The other orthorhombic samples (x = 0.055 and 0.110, respectively) showed a maximum $|\Delta S_M(T)_{\Delta H}|$ value close to that of gadolinium.

A compound of the $La_{0.67}Ca_{0.33-x}Sr_xMnO_3$ series with $x \approx 0.06$ would be expected to exhibit the same ferromagnetic transition temperature as gadolinium and to show almost competitive magnetocaloric properties. This compound could be considered a suitable candidate as working material in magnetic refrigeration near room temperature.

6 Magnetoresistive properties of $La_{0.67}Ca_{0.33-x}Sr_xMnO_3$

6.1 Introduction

This chapter concerns the magnetoresistive properties of the $La_{0.67}Ca_{0.33-x}Sr_xMnO_3$ series. Magnetoresistance, *MR*, will here be defined as the relative change of resistance (or resistivity) upon a change of the external magnetic field:

$$MR = \frac{\Delta R}{R_0} = \frac{R_H - R_0}{R_0}, \tag{28}$$

where R_0 and R_H are the resistance in zero field and in an external field H, respectively. The resistances R_0 and R_H are usually replaced by the corresponding resistivities ρ_0 and ρ_H. Sometimes authors use a slightly different definition, namely $MR = \Delta R/R_H$. This expression gives a larger *MR* value for a given change of resistance. When Jin *et al*. (1994) reported on a magnetoresistance exceeding than 100,000 % in thin film manganites they used the last-mentioned definition. Otherwise they would have obtained an *MR* value of ~99.9 %, as mentioned by the authors.

The $La_{0.67}Ca_{0.33-x}Sr_xMnO_3$ samples under investigation here are polycrystalline materials. Polycrystalline mixed-valence manganites exhibit magnetoresistance effects, which are not observed in single-crystalline materials of the same composition. Grain boundaries play a decisive role to the magnetoresistive properties, especially below the Curie temperature, where the magnetoresistance associated with changes of the local spin disorder is vanishing. The magnetoresistance associated with intra-grain effects (changes of local spin disorder) is usually referred to as intrinsic, while magnetoresistance associated with grain boundary effects is called extrinsic. As will be shown below, the magnetoresistive properties of some of the $La_{0.67}Ca_{0.33-x}Sr_xMnO_3$ samples are almost completely dominated by grain boundary transport and extrinsic magnetoresistance. Before results on the magnetotransport properties of the $La_{0.67}Ca_{0.33-x}Sr_xMnO_3$ series are presented an introduction to intrinsic and extrinsic magnetoresistance will be given. It ought to be mentioned that the investigation on the magnetoresistive properties of the $La_{0.67}Ca_{0.33-x}Sr_xMnO_3$ series was less comprehensive than the investigation on the magnetocaloric properties presented in the previous chapter. The results presented below describe the broad features of the magnetoresistive properties of the ceramic compounds, but also leaves issues to be addressed in future work.

6.2 Intrinsic and extrinsic magnetoresistance

Below follows a brief discussion on magnetoresistive properties of mixed-valence manganites. The aim is to explain the difference between intrinsic and extrinsic magnetoresistance and to illustrate how they can be distinguished from experiment. Some results from the literature are used for exemplification.

6.2.1 Intrinsic magnetoresistance

Figure 41 shows the temperature dependence of the zero field and $\mu_0 H = 5$ T resistivities of a single-crystalline thin film $La_{0.7}Ca_{0.3}MnO_3$ sample (data obtained from Hundley *et al*. (1995)). The corresponding magnetoresistance, $MR = \rho_H/\rho_0$-1, is shown in the same

graph. This sample has no internal grain boundaries so the magnetoresistive response is therefore entirely intrinsic.

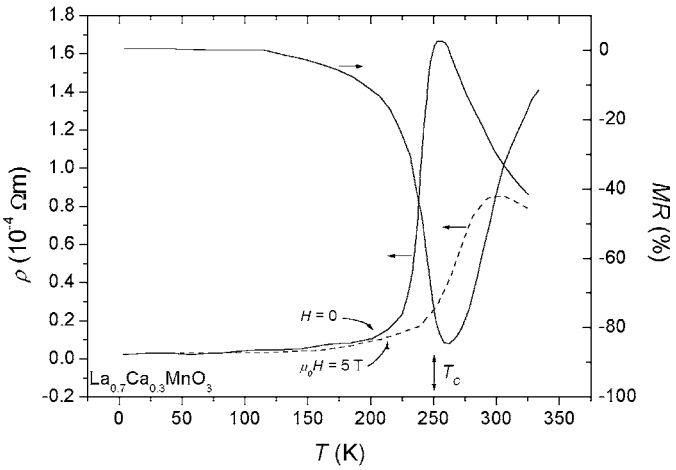

Figure 41. Resistivity of single-crystalline thin-film $La_{0.7}Ca_{0.3}MnO_3$ in zero magnetic field and in an applied field of 5 T. The graph shows also the corresponding magnetoresistance. Adopted from Hundley et al. (1995).

The thin-film substance shows a metal-to-insulator transition coinciding with the ferromagnetic-to-paramagnetic transition at the Curie temperature (250 K). Qualitatively, the temperature dependence of the magnetoresistance can be explained in terms of Zener's double-exchange mechanism introduced in Section 2.4: The simplest expression for conductivity is $G = ne\mu$, where n is the number of carriers, e is their charge, and μ their mobility. The metal-to-insulator transition could thus originate from either a change of the number of carriers or a change the mobility of the carriers. In the double-exchange theory the change of hopping mobility is the dominant effect on the conductivity. The transfer integral for electron transport between adjacent Mn sites is $t = t_0 \cos(\theta/2)$ where θ is the angle between the spin directions of the two Mn cores spins, cf. Equation (4). Below the ferromagnetic transition temperature the spin system is ferromagnetically ordered and the probability for electron transfer (and thereby the mobility) is high. The zero-field resistivity shows metallic-like temperature dependence with a positive slope. Around the Curie temperature the spin system becomes disordered because the thermal energy exceeds the ferromagnetic exchange energy. The hopping amplitude decreases and a drastic increase of the zero-field resistivity is observed. Above TC the resistivity decreases with temperature as expected for an insulator, where transport is thermally activated. The sample exhibits a large negative magnetoresistance peaking just above the Curie temperature. Below T_C the spins align spontaneously and the external field has little influence on θ. The magnetoresistance gradually vanishes when the magnetic moment approaches its saturation value. Near T_C, however, the spin system is highly susceptible to the external field, which causes a substantial change of the local spin disorder and thereby of the carrier mobility. Thus, the field drives the material more metallic. Far above the Curie point the external field can no longer compete with the thermally induced random spin fluctuations and the magnetoresistive response decreases with temperature.

It has been argued (Millis *et al.*, 1995) that double-exchange alone cannot explain the metal-to-insulator transitions in mixed-valence manganites: The double exchange trans-

fer integral is largest for complete ferromagnetic alignment ($\theta = 0$). In the paramagnetic state the average angle between adjacent spins is $\theta/2$ and the hopping probability is reduced roughly by a factor of $2^{-½}$ (Dessau and Shen, 1998). To first order one would therefore expect the zero-field resistivity to be $2^{-½}$ times larger in the paramagnetic state than it is in the ferromagnetic state. However, the resistivity usually changes several orders of magnitude at the metal-to-insulator transition. It has been suggested that the very large change in resistivity observed for manganites is due to magnetic polaron formation in the paramagnetic regime (cf. e.g. Coey *et al*. (1999) or von Helmolt *et al*. (1994)). The e_g electrons may induce a local polarization of its neighboring spins forming a small ferromagnetic entity called a magnetic polaron. A magnetic polaron can be considered a quasi-particle and it can jump from lattice site to lattice site carrying along its spin polarization. This hopping takes place via thermal activation. Below the Curie temperature (or when a magnetic field is applied) the magnetic polarons are destroyed. This could contribute to the abrupt change of resistivity near T_C. Another kind of polarons, which could be present in manganites, are dielectric polarons formed due to the Coulomb interaction between the electron and its surrounding ionic charges. Dielectric polarons also acts as quasi-particles. The concept of polaron transport in mixed-valence manganites is not yet fully understood and will not be discussed further here.

Model for intrinsic resistivity

Dionne (1996b) has developed a model for calculation of the temperature and field dependence of the intrinsic resistivity of mixed-valence manganites. This model will be applied to the $x = 0$ end-member of the $La_{0.67}Ca_{0.33-x}Sr_xMnO_3$ series below. An extensive description of the model can be found in Dionne (1996a). Below follows a brief introduction.

The electrical conductivity, here denoted G, of mixed-valence manganites obeys the relation for mobility-activated semiconductors:

$$G = ne\frac{eD}{K_B T}e^{-\frac{E_{hop}}{k_B T}}, \tag{29}$$

where n is the carrier density, the factor $eDk_B^{-1}T^{-1}$ is the Einstein diffusion mobility, D is the diffusion constant given by $d^2\tau^{-1}$, where d is the hopping distance and τ is the mean carrier lifetime, k_B is the Boltzmann constant, and E_{hop} is the activation energy for carrier hopping. The resistivity ($\sim 1/G$) can be expressed

$$\rho = Ck_B T\frac{1-x}{x}e^{\frac{e_{hop}}{k_B T}}. \tag{30}$$

Here C equals $Ve^{-2}d^{-2}\nu_{hop}^{-1}$, where V is the volume of a formula unit and ν_{hop} is the hopping frequency. x has its usual meaning, i.e. the divalent substitution factor of the mixed-valence manganite. Hence, $x = 0.33$ and $(1\text{-}x)x^{-1} = 2.03$.

The value of the C parameter for $La_{0.67}Ca_{0.33}MnO_3$ can be estimated as follows: From the Rietveld analysis the unit cell volume of this compound was found to be ~0.23 nm^3, cf. Section 4.3.1. The Pbnm unit cell contains four formula units, hence $V \approx 5.8\cdot10^{-29}$ m^{-3}. The hopping distance is taken to be equal to the distance between two neighboring Mn ions. Again using results from the Rietveld analysis, $d \approx 3.9\cdot10^{-9}$ m. The hopping frequency is equated to the Debye frequency $\nu_D = k_B h^{-1}\Theta_D$, where h is the Planck constant

and Θ_D is the Debye temperature. Taking Θ_D to be 270 K, the hopping frequency becomes ~$5.6 \cdot 10^{12}$ s^{-1}. Based on these estimates $C = 2.65 \cdot 10^{13}$ mJ^{-1}.

Dionne considered two contributions to the total activation energy: a magnetic exchange stabilization energy E_{hop}^{ex} and a (dielectric) polaron stabilization energy E_{hop}^{pol}. The magnetic exchange stabilization energy is closely related to the double exchange mechanism. It expresses the energy required to restore spin alignment if a change transfer between adjacent Mn ions takes place when the two Mn spins are not parallel. This energy can be written

$$E_{hop}^{ex} \cong 2zJ_0S_3S_4(1-\cos\theta), \tag{31}$$

where z is the number of nearest neighbors, J_0 is the exchange constant for the Mn^{3+}–Mn^{4+} coupling, S_3 is the total spin of Mn^{3+}, S_4 is the total spin of Mn^{4+}, and θ is the average angle between the spins. In the perovskite manganites each Mn ion has six nearest Mn neighbors, i.e. $z = 6$. The Mn spins are 2 and 3/2 for Mn^{3+} and Mn^{4+}, respectively. Dionne estimated the exchange constant to be $J_0 \approx 4.8 \cdot 10^{-22}$ J $= 0.0030$ eV for $x \approx 0.3$, and suggested to represent $\cos\theta$ by the Brillouin function $B_J(T,H)$ (previously introduced in Section 5.5.1). As in the model for the magnetocaloric properties J was taken to be 1.83, i.e. the average total angular moment of Mn^{3+} and Mn^{4+}. With these values the magnetic exchange stabilization energy can be written

$$E_{hop}^{ex} \cong 1.7 \cdot 10^{-20}(1-B_J)\,\mathrm{J} = 0.108(1-B_J)\ \mathrm{eV}, \tag{32}$$

The polaron stabilization energy is related to the electrostatic potential well in which the carriers reside. No details will be given on the evaluation of E_{hop}^{pol}. The value suggested by Dionne, $E_{hop}^{pol} = 6.4 \cdot 10^{-22}$ J = 0.004 eV, is simply adopted. Collecting from above the final expression for the resistivity becomes

$$\rho(T,H) = 5.4 \cdot 10^{13} k_B T \exp\left(\frac{6.4 \cdot 10^{-22} + 1.7 \cdot 10^{-20}(1-B_J(T,H))}{k_B T}\right) \Omega\mathrm{m}. \tag{33}$$

Note that the field dependence of the resistivity is incorporated via the Brillouin function.

The theoretical expression for the resistivity of $La_{0.67}Ca_{0.33}MnO_3$ will be compared with experimental data below.

6.2.2 Extrinsic magnetoresistance

Figure 42 (a) compares the temperature dependence of magnetoresistance of a single-crystalline manganite (an epitaxial thin film) with that of a polycrystalline thin film having the same composition ($La_{0.67}Ca_{0.33}MnO_3$). Data was obtained from (Gupta *et al.*, 1996).

Both samples show a magnetoresistance maximum near the Curie temperature, which can be ascribed to intrinsic magnetotransport (the CMR effect). For the epitaxial film the magnetoresistance vanishes at low temperatures, as expected for a single-crystalline material, cf. Figure 41. However, the polycrystalline film shows an increasing magnetoresistance with decreasing temperature.

Figure 42 (b) shows the field dependence of magnetoresistance at two different temperatures below the ferromagnetic transition temperature. The epitaxial sample shows a linear variation of the magnetoresistance with the applied field. This indicates that the

Bloch wall motion and domain rotation in single-crystalline manganites do not dominate transport. The magnetoresistance varies smoothly through the region of domain rotation, which takes place in low fields, so the increasing magnetoresistance is mainly due to enhanced local magnetic order. The magnetoresistance effect is small and decreases with decreasing temperature. The polycrystalline sample exhibits a completely different behavior characterized by two features: 1) a sharp increase of magnetoresistance at low-fields followed by 2) at linear background at higher fields. The slope of the high-field contribution is broadly temperature independent. The low-field magnetoresistance, which is often termed LFMR, increases with decreasing temperature.

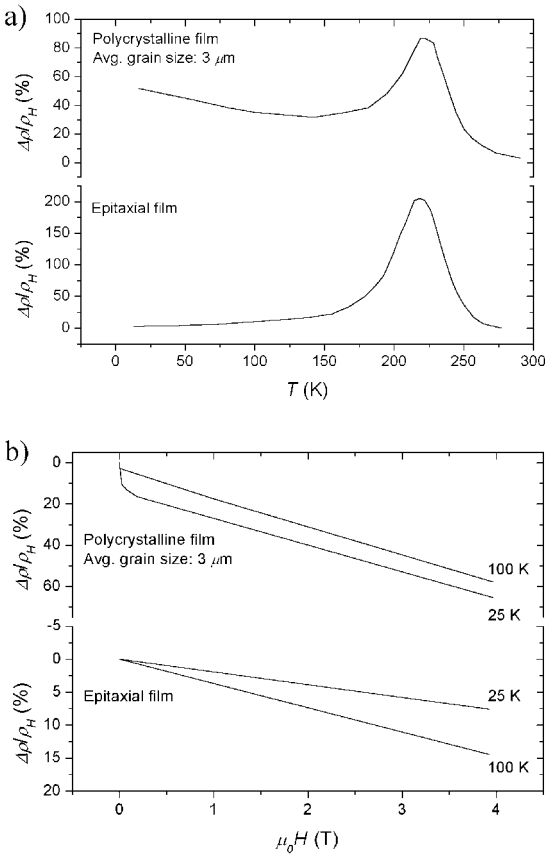

Figure 42. Magnetoresistance for a field change of 0 to 2 T versus temperature of polycrystalline (top panel) and epitaxial (bottom panel) thin film $La_{0.67}Ca_{0.33}MnO_3$. b) Magnetoresistance as a function of applied field taken at 25 and 100 K. Adopted from Gupta et al. (1996).

It has been suggested (Gupta *et al*., 1996; Li *et al*., 1997) that the low-field magnetoresistance, which is consistently observed in polycrystalline manganites, is due to spin-dependent scattering in grain boundaries. In ferromagnetic metals the exchange energy splits the conduction band into majority and minority carrier bands resulting in a spin imbalance at the Fermi level (Gupta and Sun, 1999). In mixed-valence manganites the majority and the minority bands are separated by an energy gap arising from the strong intra-atomic coupling between the $3d$ e_g conduction electrons and the $3d$ t_{2g} core spins (Okimoto *et al*., 1995). The spin polarization may therefore approach 100 % at low temperatures (thus, manganites may be characterized as half-metals). In the ferromagnetic state each grain in a polycrystalline manganite may constitute a single magnetic domain

(Gupta *et al*., 1996; Li *et al*., 1997; Hwang *et al*., 1996). In the virgin state, where no field is applied, the grains have their magnetic moments randomly oriented. The polarized conduction electrons are easily transferred between Mn sites within a magnetic domain. However, an electron traveling across a grain boundary to an adjacent grain (or domain) may become subject to a strong spin-dependent scattering leading to a high zero-field resistivity. A low external field can readily rotate the grain magnetization into a parallel configuration and thereby cause a significant drop in resistivity and low-field magnetoresistance. The degree of spin polarization is temperature dependent and increases with decreasing temperature (Ju *et al*., 2002). This could explain why the low-field magnetoresistance becomes more and more dominant as the temperature is decreased. Spin-dependent scattering of polarized conduction carriers is the dominant mechanism describing spin-valve effects in metallic GMR multilayers (Tumanski, 2001).

Hwang *et al*. (1996) offered a different explanation to the low-field magnetoresistance effect observed below the Curie temperature. They compared the magnetoresistive properties of single-crystalline and polycrystalline $La_{0.67}Sr_{0.33}MnO_3$ and also observed LFMR in the polycrystalline samples, which was absent in the single crystal. They suggested that the effect was due to spin-dependent tunneling between adjacent grains separated by an insulating grain boundary constituting a tunnel barrier for the spin-polarized conduction electrons. Also within this model the low-field magnetoresistance can be explained by the alignment of magnetizations of neighboring grains.

Spin-dependent scattering or spin-dependent tunneling can explain the low-field magnetoresistance but fail to explain the linear high-field magnetoresistance. Evetts *et al*. (1998) suggested that the high-field magnetoresistance is associated with a magnetically mesoscopic disordered interface layer present in the vicinity of grain boundaries (see Figure 43). The transport mechanism in the interface layer is the same as in the bulk parts of the grains, but the the layer has depressed Curie temperature and magnetization, which could be caused by strain, defects and weakened or absent bonds near the grain surface. The high-field MR could be related to alignment of spins in the disordered interface layer.

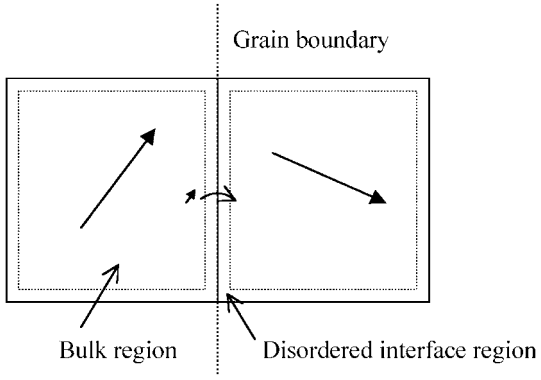

Figure 43. Schematic illustration of grain-boundary transport in a polycrystalline mixed-valence manganite. Each grain constitutes a single-magnetic domain. The conduction electrons show a high degree of spin polarization inside the grains. When traveling across the grain boundary conduction electrons may be subject to a strong spin-dependent scattering, which can be reduced if a low external magnetic field aligns the magnetizations of the two grains. Spin alignment in the disordered surface layers gives raise to high-field magnetoresistance.

6.3 Experimental procedures

Transport measurements were carried out by means of the conventional four-point probe method. For this purpose, four wires were attached to the sample using conductive silver paint. A mild heat treatment (425K, two hours) was applied to improve the adhesion of the paint to the sample surface. The wires were mounted about 4 mm apart. For the field dependence measurements (see below), a probe consisting of four collinearly placed two-part spring probes were used rather than wires. Here the inter-probe spacing was ~1 mm. The principle of the four-point resistance measuring technique is the following: A current, I, is made to flow between the two outer probes, and the voltage drop, U, between the two inner probes is measured. The high impedance of the voltmeter minimizes the current flow through the portion of the circuit comprising the voltmeter. Thus, there is no voltage drop across the resistance associated with the contact points of the inner probes; only the resistance of the sample is measured. From the resistance data the bulk resistivity can be calculated as

$$\rho = \frac{2\pi s}{F\left(\frac{a}{s}\right)}\frac{U}{I}, \tag{34}$$

where s is the inter-probe spacing, a is the side length of the cross section of the sample, and F is a geometrical correction factor compensating for the limitation of possible current paths by sample boundaries ($F = 1$ for an infinitely long sample). The samples were cut into bars with slightly different cross sections between 2×2 mm^2 and 5×5 mm^2. Two kinds of measurements were carried out to characterize the magnetotransport properties of the samples: 1) Measurements of resistance as a function of temperature with and without an external field of fixed strength. 2) Measurements of resistance as a function of field strength at fixed temperature. The temperature was controlled using a liquid-nitrogen cooled cryostat system with an integrated heater. The magnetic field was supplied by an electromagnet. In all experiments the field was applied in the current direction. However, applying the field perpendicular to the current direction did not cause any observable changes (except for a small variation, which could be ascribed to the change of the demagnetization factor). For the first type of measurement a lock-in amplifier was used both as current source and for the voltage measurement. In the second type of measurement a regulated power supply was used as current source, while the inner probe voltage drop were measured using a digital voltmeter. (The were no specific reasons other than practical reasons for using different instrumentation for the two kinds of measurements.) In both experiments, the power supplies were adjusted to provide a constant voltage of 1 V. A constant current was then obtained by inserting a resistor with resistance R, which was much larger than the resistance of the sample, R_{sample}, into the circuit. Thus, $I = U_R(R + R_{sample})^{-1} \approx UR^{-1}$, if $R >> R_{sample}$. U_R is the voltage drop over the resistor.

6.4 Results and discussion

This section presents results obtained on the magneto-transport properties of the $La_{0.67}Ca_{0.33-x}Sr_xMnO_3$ series. The $La_{0.67}Ca_{0.33}MnO_3$ sample was examined in somewhat more detail than the other samples of the series. The discussion below begins by considering the results obtained for this sample.

6.4.1 Magneto-transport in the $La_{0.67}Ca_{0.33}MnO_3$ sample

Figure 44 shows a plot of the temperature dependence of the resistivity of the $La_{0.67}Ca_{0.33}MnO_3$ sample taken in zero magnetic field and in an applied field of 0.8 T. The resistivity curves were obtained by slowly increasing the temperature from 145 to 300 K and frequently switching the magnetic field on and off. The graph also shows the corresponding magnetoresistance, $(\rho_H-\rho_0)/\rho_0$. Near the Curie temperature, which is 267 K for this compound (cf. Section 4.4), the sample exhibits a sharp transition from a metallic-like state, where the resistivity shows a positive temperature coefficient, as usually expected for a metal, to an insulator-like state, where the resistivity decreases with temperature, as expected for thermally activated conduction. The resistivity shows a maximum at the Curie temperature. The external field causes a reduction of the resistivity in the entire temperature range. The very large magnetoresistance near the Curie temperature can be ascribed to the intrinsic magnetoresistance (the CMR effect). Below the Curie temperature the magnetoresistance does not vanish as would be expected for a single-crystalline material. The magnetoresistance rather increases with decreasing temperature. From the above discussion this is a contribution arising from the presence of grain boundaries in the material. The observation of grain boundary magnetoresistance is not surprising: In Section 3.5 it was shown that the sample consists of aggregated grains with a mean diameter of about 2.2 μm. The magnetoresistance profile resembles that obtained by Gupta *et al*. (1996) for a polycrystalline thin film with a grain size of 3 μm, cf. Figure 42 (a), top panel. In both cases intrinsic magnetoresistance dominates near the Curie temperature and gives rise to a distinct CMR peak. The extrinsic magnetoresistance becomes dominant below the Curie temperature and increases as the temperature is reduced.

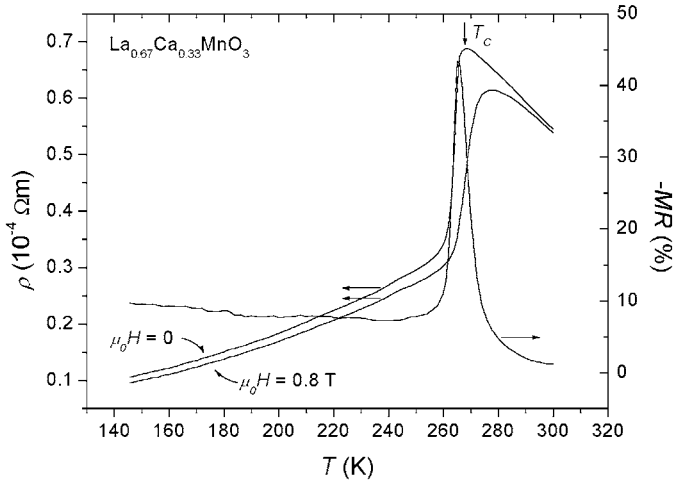

Figure 44. Temperature dependence of resistivity taken at zero field and in a field of 0.8 T and corresponding magnetoresistance for the $La_{0.67}Ca_{0.33}MnO_3$ compound. Note that the magnetoresistance is negative.

Figure 45 shows the field dependence of the resistivity taken at fixed temperatures above, near, and below the Curie temperature. The corresponding field dependence of magnetoresistance is shown for selected isotherms. The field was swept in both directions from -1.2 T to 1.2 T. Note that since *MR* is linearly dependent of ρ_H, the corresponding resistivity and magnetoresistance curves have exactly the same shape. Within the field resolution of these measurements the resistivity curves peak at zero field reflect-

ing the very low magnetic coercivity of the compounds (a high coercivity would tend to shift the resistivity maximum to the coercivity field (Linderoth and Jacobsen, 1996)). The variation of the resistivity with the applied field depends strongly on temperature. Near the Curie temperature (267 K) the resistivity drops rapidly at low field and then tend to saturate at higher fields. A large magnetoresistance is observed. Above and below T_C the resistivity varies slowly with the external field in the entire field range and accordingly the magnetoresistance effect is smaller. Because the resistivity depends on the angle between neighboring Mn spins, the field dependence of ρ and *MR* should be correlated with change of magnetization caused by the magnetic field. Near the Curie temperature, where the spin interaction is still weak, the magnetoresistance in mixed-valence manganites is usually reported to be proportional to $\sigma^2\sigma_s^{-2}$, where σ_s is the saturation magnetization (Urushibara *et al*., 1995; Vertruyen *et al*., 2001). This is also the case for the $La_{0.67}Ca_{0.33}MnO_3$ compound. For instance, at 283 K the magnetoresistance varies as H^2 (the solid line through the *MR*(*H*) data points shows the best fit to a second order polynomial), while the magnetization is linear in *H*, cf. Figure 30 (a), p. 55). Thus, $MR \propto \sigma^2\sigma_s^{-2}$. Near the transition temperature the magnetization shows a nonlinear dependence of *H*. The spin system is much more susceptible to the external field and the magnetization increases fast at low field before it starts to saturate. The magnetoresistance shows a qualitatively similar field dependence (for instance at 269 K).

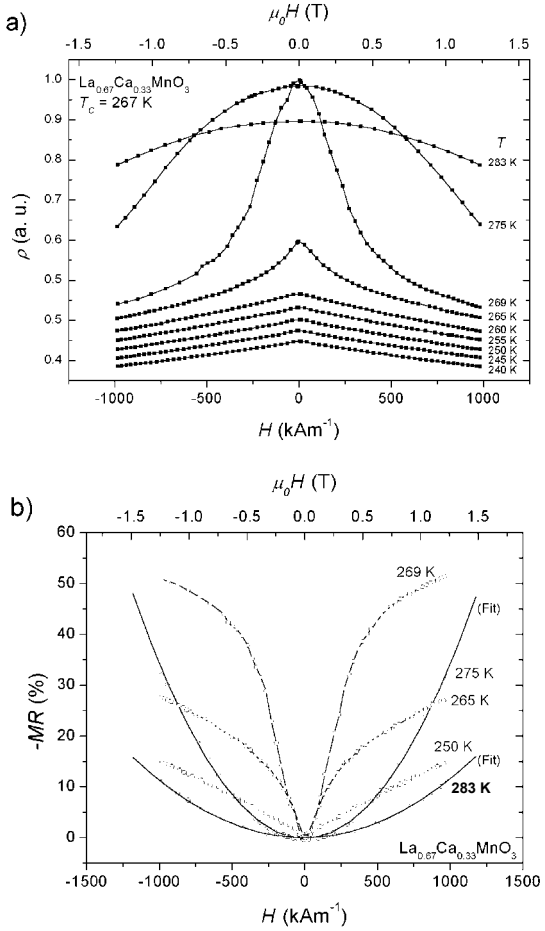

Figure 45. a) Resistivity of $La_{0.67}Ca_{0.33}MnO_3$ (normalized to the maximum ρ value) versus applied magnetic field for different temperatures. b) Corresponding magnetoresistance for selected isotherms.

Figure 45 shows no evidence of grain boundary effects. The material basically behaves as would be expected for a single crystal, where the field dependence on the resistivity can be understood from the changes of the local spin disorder (the angle between neighboring Mn core spins) caused by the external field. However, at somewhat lower temperatures, the extrinsic magnetoresistance contributions become apparent. Figure 46 shows the magnetoresistive response at 200 and 220 K, respectively. For a single-crystalline material the magnetoresistance would be expected to show a linear variation with increasing field and the MR would be expected to decrease with decreasing temperature, cf. Section 6.2.2. The $La_{0.67}Ca_{0.33}MnO_3$ sample shows distinct low-field magnetoresistance. The *LFMR*, which is usually determined by back-extrapolating the linear high-field contribution, increases with decreasing temperature. At 200 K the low-field magnetoresistance is thus about 4 %.

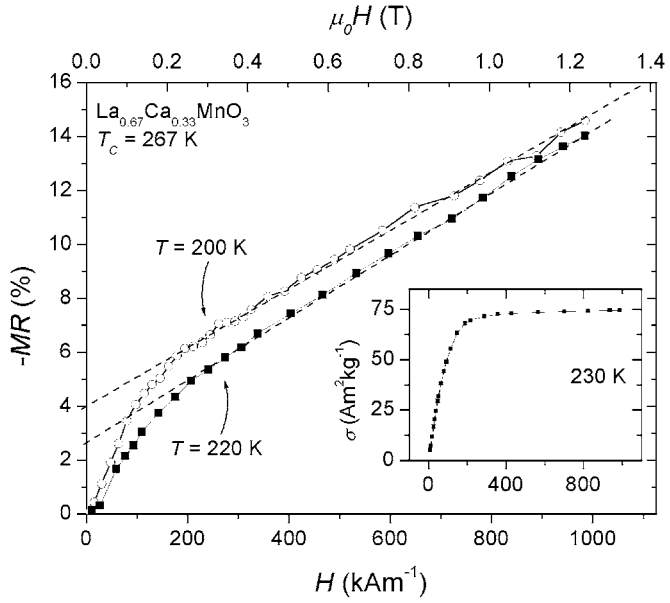

Figure 46. Magnetoresistance of the $La_{0.67}Ca_{0.33}MnO_3$ compound versus the external magnetic field at 200 K and 220 K, respectively. Inset shows magnetization curve taken at 330 K.

Once more referring to the discussion in Section 6.2.2 the low-field magnetoresistance could be due to spin-dependent scattering in grain boundaries. The *LFMR* dominates for field values up to about 150–200 kAm^{-1}. This agrees quite well with magnetization data. The inset in Figure 46 shows the magnetization curve taken at 230 K (i.e. at slightly higher temperature than the two *MR*-curves). A sharp increase in magnetization, which can be ascribed to domain rotation, is observed for the field range 0–180kAm^{-1}. Qualitatively, the *MR* data thus appears to be consistent with the theory of spin-dependent scattering at grain boundaries. A quantitative analysis would require further research. It would be interesting to investigate the relationship between domain rotation and *LFMR*, for instance by means of magneto-optic microscopy.

Enhancing the grain boundary resistivity

To gain further insight into the role of grain boundary transport in the $La_{0.67}Ca_{0.33}MnO_3$ system two additional samples with this composition were prepared. As described in

Section 3.3, the $La_{0.67}Ca_{0.33}MnO_3$ samples was prepared by pressing a calcined powder into a bar, which was sintered at 1775 K for five hours. The same calcined powder was used for the two additional samples, but the sintering temperature T_s was reduced to 1475 and 1275 K, respectively. The sintering time was not altered. The sintering temperature 1275 K was in fact lower than the calcination temperature (1375 K), for which reason the sintering activity was very low. Therefore this sample basically constituted a powder compact.

Figure 47 compares x-ray patterns of the three $La_{0.67}Ca_{0.33}MnO_3$ compounds. The diffractograms are very similar indicating that the reduced sintering temperature did not lead to any significant changes of the crystallographic properties. The two samples with reduced T_s had the same orthorhombic perovskite structure as the original $La_{0.67}Ca_{0.33}MnO_3$ sample, cf. Section 4.3. The sample sintered at 1275 K, i.e. the lowest temperature of the series, showed a slight line broadening, which could be ascribed to increased stress/strain or the presence of a fraction of very small crystallites causing Scherrer broadening.

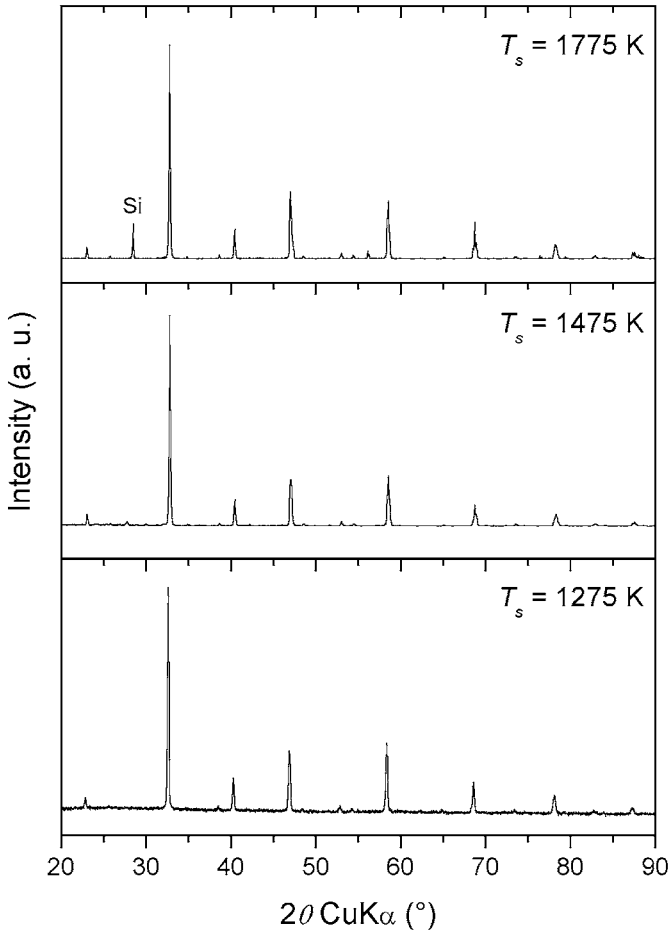

Figure 47. X-ray patterns of the $La_{0.67}Ca_{0.33}MnO_3$ samples sintered at different temperatures.

The morphological properties of the samples were strongly affected by the reduced sintering temperature. Figure 48 shows scanning electron micrographs of the three samples. As was previously shown in Section 3.5, the sample sintered at 1775 K showed a very dense microstructure with almost no pore formation. The samples sintered at lower temperatures were clearly less compact and showed a smaller average grain size. The typical grain size of the sample with T_s = 1275 K is about 0.5 μm, i.e. about five times smaller than the average grain size of the sample sintered at 1775 K. The sample with T_s = 1475 K shows an "intermediate" microstructure.

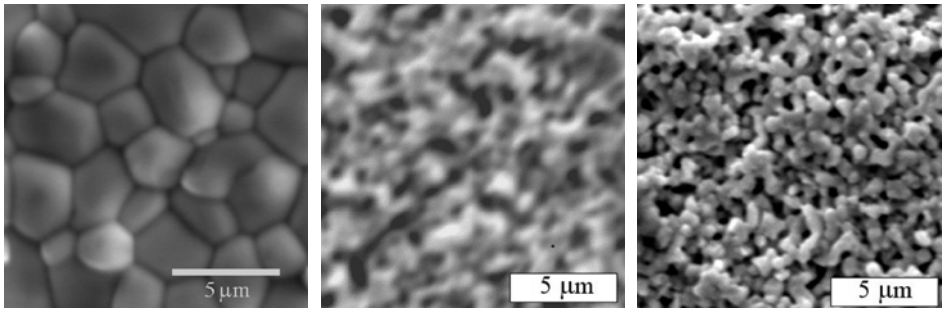

Figure 48. Surface electron micrographs of $La_{0.67}Ca_{0.33}MnO_3$ samples sintered at different temperatures. From left, T_s = 1775, 1575, and 1275 K. Scale bars = 5 μm. The sample sintered at 1575 and 1275 K were analyzed in a low-vacuum SEM instrument, which explains the somewhat poor image quality.

As anticipated, the change of microstructure introduced by reducing sintering temperature clearly affected the transport properties. Figure 49 shows the temperature dependence of ρ and ρ_H ($\mu_0 H$ = 0.8 T) for the three samples. The upper panel shows the theoretical $\rho(T,H)$ curves calculated from Equation (33), p. 76.

It is interesting to compare the calculated zero-field resistivity curves with that of the original $La_{0.67}Ca_{0.33}MnO_3$ sample (T_s = 1775 K). The calculated curve does not represent a best fit. The calculation is based on a combination of empirical and theoretical structural and magnetic parameter values. With that in mind, and considering that the model does not include resistivity contributions arising from grain boundaries, the resemblance between the calculated and observed zero-field resistivity is rather striking. Near the Curie temperature, the calculated and observed resistivities are almost equal with maximum values of $\sim 0.25 \cdot 10^{-4}$ and $\sim 0.6 \cdot 10^{-4}$ Ωm, respectively. Considering the theoretical resistivity to be representative for the intrinsic resistivity, the observed $\rho(T)$ curve seems to be superimposed by an additional resistivity component, which could be ascribed to scattering at grain boundaries.

When the sintering temperature is reduced, ρ increases. The resistivity of the sample sintered at 1275 K is about two orders of magnitude larger than the resistivity of the Ts = 1775K sample. This is not surprising since a current path of a given length involves a lot more grain boundary passages in the powder compact than in the dense sintered samples. The intrinsic metal-to-insulator transition is hardly visible for the sample with T_s = 1275 K; it appears only as a small bump near 270 K. This indicates that the effective resistivity can be considered as the superposition of the intrinsic and the extrinsic resistivity, so to first approximation the two resistances seem to be acting in series.

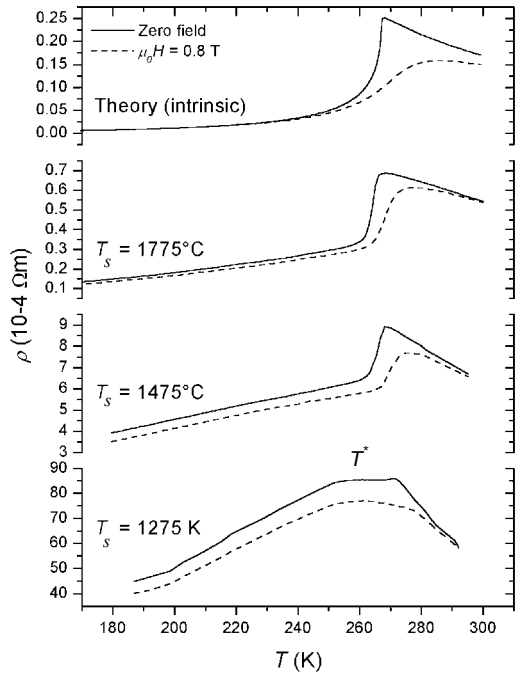

Figure 49. Temperature dependence of zero-field resistivity and the resistivity in an applied field of 0.8T for $La_{0.67}Ca_{0.33}MnO_3$ sintered at different temperatures. Top panel shows the theoretical intrinsic resistivity calculated from the model proposed by Dionne, cf. Section 6.2.1

The extrinsic resistivity component increases rather rapidly with temperature and reaches a plateau around 260 K (denoted T^* in Figure 49) before its starts to decrease above the Curie temperature. This behavior could be due to the presence of a magnetically disordered interface layer near the grain boundaries (i.e. near grain surfaces) as suggested by Evetts *et al*. (1998). The curve could be representing a complex superposition of "metal-to-insulator transitions" in the surface-near regions showing a wide distribution of local Curie temperatures. Vertruyen *et al*. (2001) succeeded in measuring the resistivity across a single grain boundary in a Ca-doped lanthanum manganite. The single grain boundary gave rise to a $\rho(T)$ curve very similar to the one observed for the sample with T_s = 1275 K. The temperature T^* is sometimes referred to as the Curie temperature of the disordered interface layer believed to be present adjacent to grain boundaries in the granular manganites (Zhang *et al*., 1997; Hernández *et al*., 2002).

Some authors have attempted to reproduce these broad "metal-to-insulator" transitions associated with grain boundaries by empirical models. Hernández *et al*. (2002) suggested to fit the grain boundary resistivity to as e xpression involving a metallic resistivity contribution given by $A + BT^2$ (metallic-like behavior) and a paramagnetic contribution given by $\rho_0 \exp(E_a k_B^{-1} T^1)$ (thermally activated polaronic transport). They used an empirical expression for the volume fraction f of ferromagnetic regions:

$$f = \frac{1}{1 + e^{-\frac{U(1-T/T_C)}{k_B T}}}, \tag{35}$$

where U is an energy parameter and T_C is the "Curie temperature" of the disordered phase. The fraction f is 1 for $T << T_C$ and 0 for $T >> T_C$. The resistivity measured for the T_s = 1275 K sample can also be fitted using such a model, but the result reveals very lit-

tle information on the physics involved with the temperature dependence of the grain boundary resistivity. It just states that the broad resistivity feature showing a plateau below the intrinsic metal-to-insulator transition feature could be related to disordered magnetic regions adjacent to the grain boundaries showing a distribution of Curie temperatures.

Figure 50 shows the magnetoresistance as a function of temperature for the three $La_{0.67}Ca_{0.33}MnO_3$ samples. This figure illustrates very clearly that the extrinsic magnetoresistance gradually becomes more dominant as the sintering temperature is decreased. The intrinsic CMR peak near the Curie temperature is observed for all the samples, but its intensity decreases. The slight shifting of the CMR peaks towards higher temperatures could reflect that the Curie temperature of the intra-grain regions increases with decreasing grain size (this remains to be confirmed by magnetization measurements). It is evident that the non-vanishing low-temperature magnetoresistance is due to the grain boundaries. Although the sample sintered at 1275 K shows a slightly enhanced low-T magnetoresistance compared to the other samples, the variation of the low-temperature magnetoresistance with sintering temperature is surprisingly marginal. The main difference between the samples seems to be the number of grain boundaries that the conduction electrons must cross for a given distance between the contact electrodes.

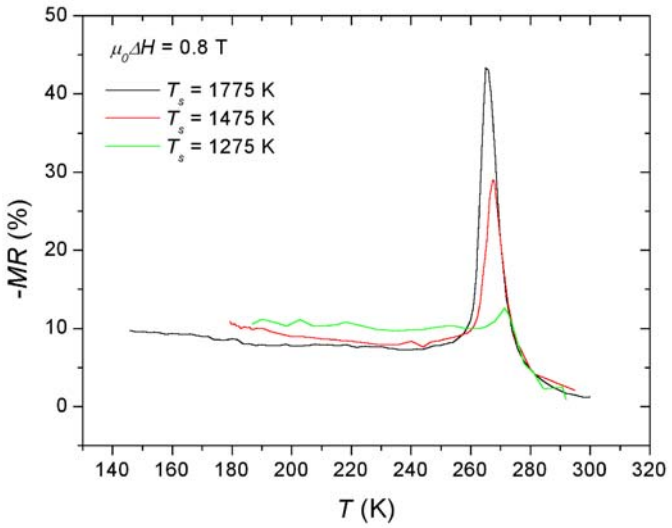

Figure 50. Magnetoresistance versus temperature for the $La_{0.67}Ca_{0.33}MnO_3$ samples sintered at different temperatures. Curves were obtained with a magnetic field change of 0.8 T.

This section is concluded by a brief discussion on the field dependence on the resistivity of the $La_{0.67}Ca_{0.33}MnO_3$ samples sintered at reduced temperatures. Figure 51 shows ρ versus H curves for the two samples taken at different temperatures. The curves obtained for the sample sintered at 1475 K resemble that of the main $La_{0.67}Ca_{0.33}MnO_3$ sample, cf. Figure 45. Above T_C, e.g. at 284 K, the resistivity versus field curves show a parabolic behavior. Near below T_C, at 267 K, the resistivity decreases rapidly at low fields and more slowly at higher fields. Below *TC*, e.g. at 240 K, the resistivity tends to become linear in H also at low fields, but when the temperature is increased further the low-field magnetoresistance component appears. For the powder compact sample (T_s = 1275 K) grain boundary resistance appears to be dominating also near the Curie temperature of the bulk phase. The 269 K isotherm does not show the characteristic rapid decrease in

low fields expected when intrinsic transport is dominating (compare for instance with the 269 K isotherm of the T_s = 1475 K sample in the left panel of Figure 51). This is a further indication that grain boundaries almost completely dominate resistance in this sample.

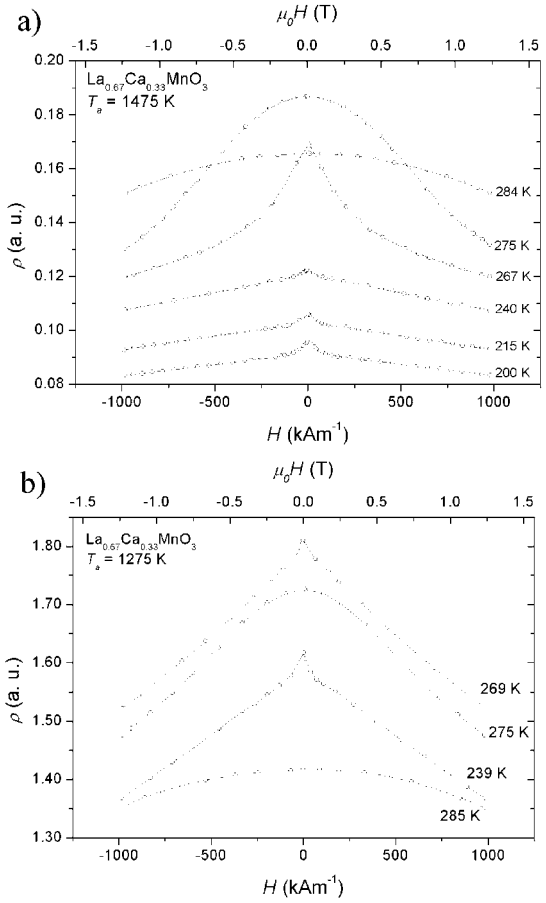

Figure 51. Resistivity (in a.u.) versus applied field at various temperatures for a) the $La_{0.67}Ca_{0.33}MnO_3$ sample sintered at 1475 K and b) the $La_{0.67}Ca_{0.33}MnO_3$ sample sintered at 1275 K.

6.4.2 Magnetotransport in $La_{0.67}Ca_{0.33-x}Sr_xMnO_3$

The above discussion on the magnetoresistive properties of the $La_{0.67}Ca_{0.33}MnO_3$ samples sintered at different temperatures provides a good basis for the interpretation of the results obtained on the magneto-transport in the remaining samples of the $La_{0.67}Ca_{0.33-x}Sr_xMnO_3$ series.

In Section 3.5 it was shown that the average grain size of the $La_{0.67}Ca_{0.33-x}Sr_xMnO_3$ samples decreases linearly with the Sr content. The compounds also appeared to become less compact (more porous) with increasing x, cf. Figure 10, p. 24. To some extent, this variation of the microstructure corresponds to the morphological changes caused by decreasing the sintering temperature for the $La_{0.67}Ca_{0.33}MnO_3$ compound. A similar influence on the magnetoresistive properties, i.e. an enhanced grain boundary contribution, would therefore be expected. Figure 52 shows the temperature dependence of ρ and ρ_H ($\mu_0 H$ = 0.8 T) for five selected samples of the $La_{0.67}Ca_{0.33-x}Sr_xMnO_3$ series. Considering the zero-field resistivities, there is a striking resemblance between the results obtained by lowering the sintering temperature for the $La_{0.67}Ca_{0.33}MnO_3$ and the results obtained by in-

creasing x. When x is increased from 0 to 0.275 the zero-field resistivity increases by one order of magnitude most likely due to the increased specific number and maybe the physical characteristics of grain boundaries. A parabolic-like resistivity component also recognized feature related to grain boundaries becomes dominant for x = 0.220, where the intrinsic metal-to-insulator transition is almost vanishing and only appears as a small shoulder. For the x = 0.275 sample the intrinsic resistivity contribution is hardly observable.

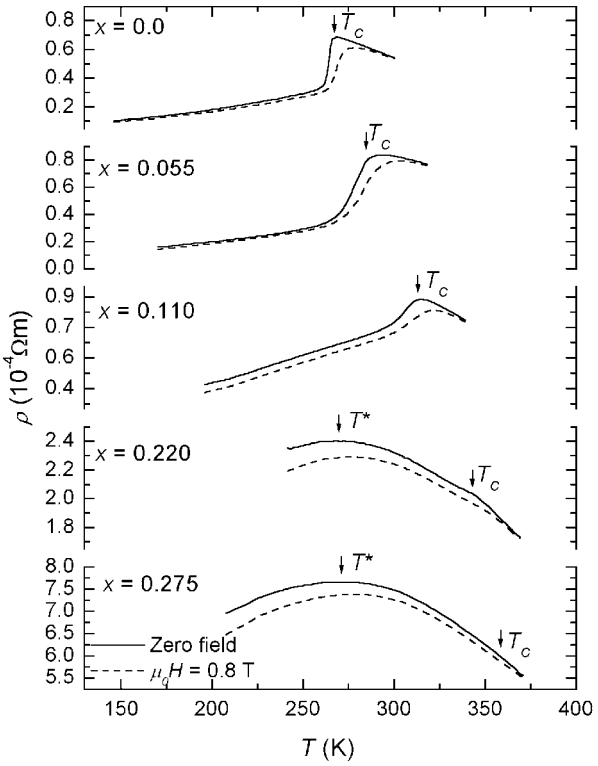

Figure 52. Zero field resistivity (solid curves) and resistivity in an applied field (0.8 T) as a function of temperature for five selected $La_{0.67}Ca_{0.33-x}Sr_xMnO_3$ samples. Curves are labeled by corresponding x values.

It is remarkable that the grain boundaries have such a strong influence on the resistive properties of these two samples considering that the grain size is only reduced by about 1 μm compared to the $La_{0.67}Ca_{0.33}MnO_3$ sample, cf. Figure 12, p. 25. The explanation could be that the intrinsic resistivity is decreasing with increasing Sr content. As was shown in Section 4.3, the mean Mn–O–Mn bond angle increases with increasing x. This enhances the e_g(Mn)–$2p_\sigma$(O)–e_g(Mn) hybridization strength and thereby the electronic bandwidth. Thus, the resistivity associated with intrinsic transport would be expected to decrease with increasing x (or more specifically increasing mean A-site ionic radius, $\langle r_A \rangle$). Coey *et al*. (1995) have reported the low-temperature resistivity of thin film $La_{0.7}Sr_{0.3}MnO_3$ to be two orders of magnitude smaller than the low-temperature resistivity in $La_{0.7}Ca_{0.3}MnO_3$, so the gradual substitution of Ca with Sr in the $La_{0.67}Ca_{0.33-x}Sr_xMnO_3$ series is definitely expected to cause a decrease of the intrinsic resistivity. The fact that the resistivity contribution ascribed to the disordered grain boundary region gradually becomes more dominant with increasing x is most likely related to a simultaneous increase of extrinsic and decrease of intrinsic resistivity.

For the $La_{0.67}Ca_{0.33}MnO_3$ sample sintered at low temperature (the powder compact) the extrinsic resistivity component showed a plateau and a maximum (designated T^* in Figure 49) just below the Curie temperature of the bulk phase. The difference between T_C and T^* is about 10 K. For the x = 0.220 and 0.275 samples of the $La_{0.67}Ca_{0.33-x}Sr_xMnO_3$ series this difference is much larger, about 73 and 82 K, respectively (see Figure 52). $|T_C - T^*|$ thus seem to increase with increasing Sr content. Assuming that the extrinsic resistivity is related to a surface layer with depressed T_C and magnetization, this would mean that this surface layer becomes more disordered and showing a wider distribution of Curie temperatures with increasing substitution of Ca with Sr. It is not evident why this should be the case. A possible explanation is the decreasing sintering ability of the samples with high Sr content. The comparatively heavy Sr ions have a lower diffusion rate than the Ca ions so it might be that a high Sr content leads to less homogeneous compounds perhaps with a disordered surface region extending over more atomic layers than in the samples with low Sr content. This could lower the coupling between the surface layer and the intra-grain regions and cause a further reduction of the surface Curie temperature. High-resolution transmission electron microscopy could provide more information on the degree to which these samples are disordered near grain surfaces. This is suggested for future work.

Figure 53 shows the magnetoresistance versus temperature for the five $La_{0.67}Ca_{0.33-x}Sr_xMnO_3$ samples. As was also seen directly from the corresponding resistivity curves in Figure 52, the extrinsic magnetoresistance gradually becomes more dominant as x is increased. Intrinsic CMR peaks are observed for all the samples, but for x = 0.275 the CMR peak is almost vanishing. The magnetoresistive response for this sample is very similar to that of the $La_{0.67}Ca_{0.33}MnO_3$ powder compact (sintered at 1275 K), where the grain boundary magnetoresistance was almost completely dominating. The CMR peak of the $La_{0.67}Ca_{0.33}MnO_3$ sample is markedly sharper than it is for the other samples in the series. This can be ascribed to the very sharp ferromagnetic transition in this sample, which naturally also leads to a sharp CMR response. As mentioned in the previous chapters, the enhanced ferromagnetic properties of this sample could be related to the dynamic Jahn-Teller effect. All the samples show a similar non-vanishing low-temperature magnetoresistance, which increases with decreasing temperature.

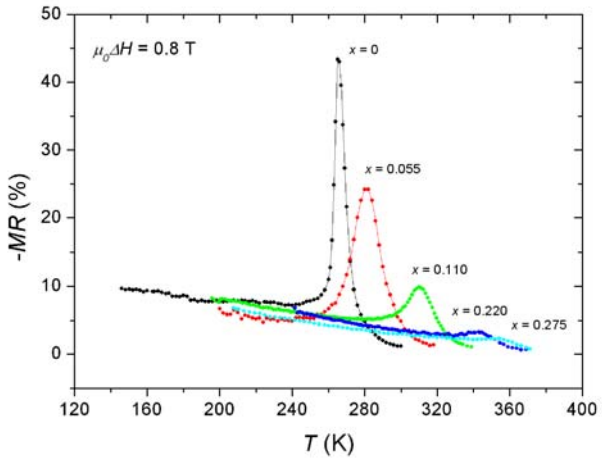

Figure 53. Magnetoresistance due to an applied field of 0.8 T as a function of temperature. MR calculated from resistivity data in Figure 52.

Figure 54 shows the magnetoresistance at the intrinsic metal-to-insulator transition temperature T_{MI} , i.e. the maximum CMR effect (not corrected for the *MR* background signal related to extrinsic magnetoresistance) and the magnetoresistance obtained 80 K below the CMR peak, where extrinsic *MR* is dominating, both as a function of the Ca/Sr ratio of the $La_{0.67}Ca_{0.33-x}Sr_xMnO_3$ series, i.e. *x*. The CMR effect decays exponentially with x. As suggested above, this is probably due to 1) a decrease in intrinsic resistivity, which also leads to a less distinct metal-to-insulator transition ($La_{0.67}Sr_{0.33}MnO_3$ is shows good conducting properties also in the paramagnetic regime) and therefore also a smaller CMR effect, and 2) the increasing extrinsic resistivity. The magnetoresistance obtained 80 K below the CMR maximum decreases roughly linearly with *x*. This could be related to an increase of the thickness of the disordered surface layer, which was also suggested as an explanation for the depressed Curie temperature of the surface layer, T^*. Spin-dependent scattering varies as d^{-3}, where *d* is the domain wall width (Coey et al., 1999). Thus, if the interface layer becomes wider the magnetoresistance associated with spin-dependent scattering would decrease.

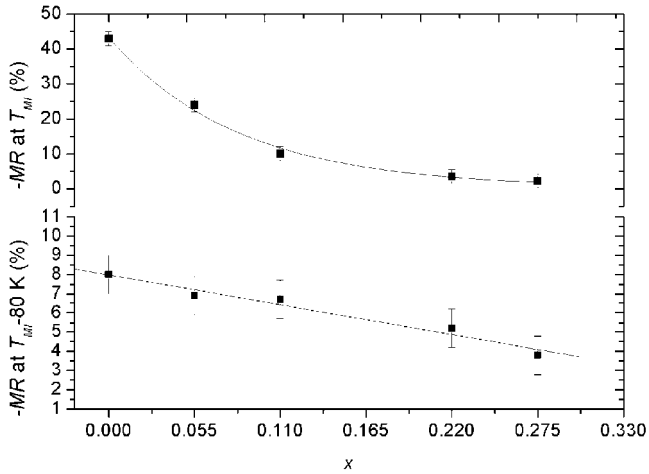

Figure 54. Maximum CMR effect (top panel) and magnetoresistance (bottom panel) obtained 80 K below CMR peak temperature (T_{MI}) as a function of x.

The last result to be presented is a very nice example of low-field and high-field magnetoresistance obtained for the $La_{0.67}Ca_{0.110}Sr_{0.220}MnO_3$ sample at temperatures far below the intrinsic metal-to-insulator transition temperature (~344 K), see Figure 55. At 185 K the sample shows a large low-field magnetoresistance. An applied field of just 0.1 T produces a resistivity change of 7 %, probably due to a reduction of spin-dependent scattering induced be alignment of magnetic domains (possibly each grain constitutes a domain). At higher fields the usual linear background ascribed to spin alignment in the disordered interface layer appears. At 278 K, i.e. somewhat closer to the metal-to-insulator transition, the low-field component is less distinct. The slope of the high-field magnetoresistance is roughly temperature independent. As pointed out earlier, this is typical the behavior of a granular perovskite manganites, cf. Section 6.2.2.

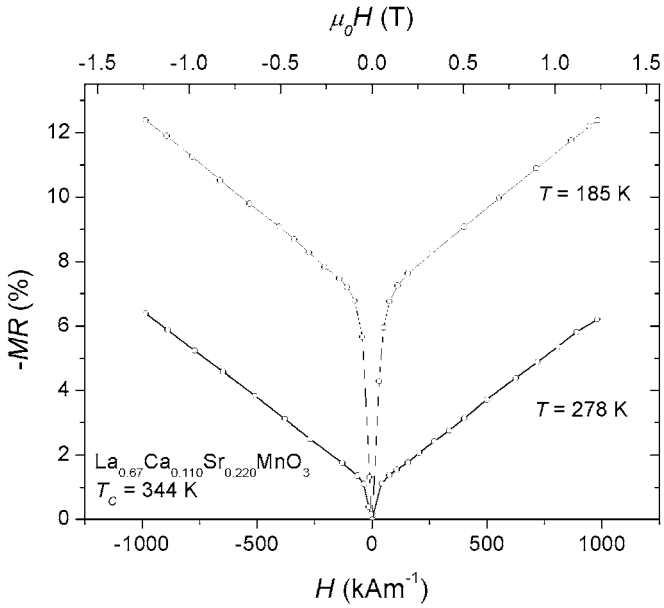

Figure 55. Magnetoresistance of the $La_{0.67}Ca_{0.110}Sr_{0.220}MnO_3$ sample (x = 0.220) versus applied field. Data obtained at T = 185 and 275 K, respectively.

6.5 Applications

The CMR effect in manganites has drawn lot of attention due to its possible application in magnetic sensing devices. In Section 5.6, the compound $La_{0.67}Ca_{0.27}Sr_{0.06}MnO_3$ was predicted to show a Curie transition at room temperature. Taking into account the exponential decay of the CMR effect with increasing Sr content, cf. Figure 54, the compound would be expected to show a CMR effect of about 20 % with an external field of 0.8 T (including the background *MR* arising from the presence of grain boundaries). Based on the peak width obtained for the $x = 0.055$ sample, the magnetoresistance would exceed 10 % between 288 K (12°C) and 315 K (42°C). One could imagine many kinds of magnetoresistive devices based on this effect, for instance position sensors and rotation speed sensors, see e.g. Tumanski (2001).

It has been argued that the technological relevance of the CMR effect might be questionable because 1) the effect is confined to a rather narrow temperature range around T_C and 2) the metal-to-insulator transition would probably give rise to an unacceptably high electrical noise (Hwang *et al.*, 1996). For these reasons the low-field magnetoresistance observed for granular manganites could be more significant for applications than the intrinsic CMR effect. A position-sensing device based on the grain boundary magnetoresistance in thick film Sr-doped lanthanum manganite has already been demonstrated (Balcells *et al.*, 2000; Fontcuberta *et al.*, 2002).

The $La_{0.67}Ca_{0.33-x}Sr_xMnO_3$ samples as prepared here might not be of any practical application. However, the precursor material used for preparation of the solid $La_{0.67}Ca_{0.33-x}Sr_xMnO_3$ bars (i.e. the calcined powder) could readily be used also for preparation of thick films. Based on the present investigation the samples with high Sr content would show a magnetoresistance of several percent even in a rather low applied field. Reduction of the calcination temperature could lead to a decreased grain size and probably an enhancement of the low-field magnetoresistance. The $La_{0.67}Ca_{0.33-x}Sr_xMnO_3$ compounds definitely may have potential as working materials in magnetoresistive devices.

6.6 Summary and conclusion

Results on the magnetoresistive properties of selected $La_{0.67}Ca_{0.33-x}Sr_xMnO_3$ samples have been presented. From a comparison with previous reports on the magneto-transport in single-crystalline and polycrystalline mixed-valence manganites it was concluded that the presence of grain boundaries play a decisive role to the magnetoresistive properties of the $La_{0.67}Ca_{0.33-x}Sr_xMnO_3$ system.

By preparing $La_{0.67}Ca_{0.33}MnO_3$ samples with different sintering temperatures, grain boundary-related resistivity and magnetoresistance features were enhanced. It appeared that the grain boundary resistance to first approximation acted in series with the intrinsic resistance associated with local spin disorder. It was concluded that grain boundaries gave rise to 1) increased zero-field resistivity 2) a characteristic resistivity signal showing a maximum at a temperature below the intrinsic insulator-to-metal transition 3) a low-field magnetoresistance increasing with decreasing T 4) a high-field magnetoresistance showing very little variation with temperature. These features could indicated that there exists two magnetic phases in the granular perovskites: 1) bulk intra-grain regions which may constitute single magnetic domains below T_C and 2) an interface layer adjacent to the grain boundaries with depressed magnetization and a distribution of local Curie temperatures. Spin-dependent scattering of polarized conduction electrons traveling between adjacent grains could be the source of the characteristic low-field magnetoresistance, asserting that a low field readily may align the magnetizations of adjacent grains. The high-field magnetoresistance could be due to spin alignment in the disordered surface layer. For the $La_{0.67}Ca_{0.33-x}Sr_xMnO_3$ series, the CMR effect decreased exponentially with increasing Sr content. This was ascribed not only to the increasing contribution from grain boundaries, but also to an expected reduction of the intrinsic resistivity and magnetoresistance caused by enhanced bandwidth (increasing Mn–O–Mn bond angle).

The above discussion on the magnetoresistive properties of the $La_{0.67}Ca_{0.33-x}Sr_xMnO_3$ sample has mostly been qualitative. The presently available data simply did not allow for a proper quantitative analysis. Some proposals for further research on the magnetotransport properties of the $La_{0.67}Ca_{0.33-x}Sr_xMnO_3$ series were put forward.

7 Conclusion and outlook

Results on structural, magnetic, magnetocaloric, and magnetoresistive properties of a series of Ca- and Sr- doped lanthanum manganites, $La_{0.67}Ca_{0.33-x}Sr_xMnO_3$ ($0 < x < 0.33$) have been presented and discussed. The samples were polycrystalline ceramics prepared by the glycine-nitrate combustion process. Elemental analysis showed a reasonable agreement between nominal and actual sample compositions, although the oxygen stoichiometry might not be ideal. The grain size decreased and the sample became more porous with increasing Sr content.

A structural analysis was carried out by means of *x*-ray diffraction and the Rietveld refinement method (all measurements were performed at room temperature). The samples were single-phase perovskites. The variation of the Ca/Sr ratio caused significant structural changes. A transition from orthorhombic (Pbnm) to rhombohedral ($R\bar{3}c$) symmetry occurred in the composition range $0.110 < x < 0.165$. The Mn–O bond distance was found to be independent of x, whereas the mean Mn–O–Mn bond angle increased systematically with x. This was ascribed to the size mismatch between the divalent A-site ions (Ca^{2+} and Sr^{2+}) and the space between the oxygen octahedra, where they reside. The size mismatch decreased with increasing Sr content and the Mn–O–Mn bond angle approached the ideal 180°.

The temperature dependence of the adiabatic temperature change, $\Delta T_{ad}(T)_{\Delta H}$, and the isothermal magnetic entropy change, $\Delta S_M(T)_{\Delta H}$, were measured by means of direct and indirect measuring techniques, respectively. Both quantities are measures of the magnetocaloric effect. The latter was calculated from a series of isothermal magnetization curves. The samples showed distinct magnetocaloric peaks around their respective Curie temperature. Maximum $\Delta T_{ad}(T)_{\Delta H}$ and $|\Delta S_M(T)_{\Delta H}|$ values were compared using results of heat capacity measurements and were found to be in fairly agreement. A model for the magnetocaloric effect was established. The model provided reasonable predictions for the magnetocaloric properties of the $La_{0.67}Ca_{0.33-x}Sr_xMnO_3$ samples. The $La_{0.67}Ca_{0.33}MnO_3$ compound showed a magnetocaloric effect comparable to that of gadolinium, which is usually suggested as working material for magnetic refrigeration near room temperature. The magnetic entropy change observed for the $La_{0.67}Ca_{0.33}MnO_3$ exceeded that of gadolinium by a factor of 1.7. $La_{0.67}Ca_{0.33-x}Sr_xMnO_3$ (with a fairly low Sr content) thus seem to be a suitable candidate as working substance in future magnetic cooling technology operable near room temperature.

The temperature and magnetic field dependence of the resistivity of selected samples in the compound series were measured by means of the conventional four-point probe technique. The samples with low Sr content showed distinct metal-insulator transitions near the Curie point, which could be ascribed to the increasing local spin disorder associated with the cross-over from the ferromagnetic to the paramagnetic state. An external field caused a large change of resistivity and CMR peaks were observed. The intrinsic resistivity appeared to be superimposed by an additional resistivity component, which could be ascribed to the presence of grain boundaries. This was confirmed by preparing additional $La_{0.67}Ca_{0.33}MnO_3$ samples, where grain size and sample compactness were reduced by introducing a lower sintering temperature. All the samples showed a non-vanishing low-temperature magnetoresistance, which is absent in single-crystalline materials. A characteristic low-field magnetoresistance was also observed at low temperature. This

effect is usually ascribed to spin-dependent scattering in the grain boundary regions. Qualitatively the results obtained for the $La_{0.67}Ca_{0.33-x}Sr_xMnO_3$ compounds appeared to be consistent with this model. Grain boundary-related resistance was dominating transport for the samples with high Sr content. This was ascribed partly to an anticipated decrease of the intrinsic resistance due to the reduced Mn–O–Mn bond angle, and partly to the reduced grain size and sample compactness caused by the increased Sr content.

The variation of one single parameter, namely the Ca/Sr ratio of the mixed-valence lanthanum manganite series $La_{0.67}Ca_{0.33-x}Sr_xMnO_3$, has revealed a wide range of interesting physical phenomena. It has also demonstrated a strategy for tailoring working substances for specific technological applications. Hopefully future work will be carried out to test the performance of the fascinating materials in real devices.

Appendix A: The basics of the Rietveld refinement method

This appendix gives a brief introduction to the Rietveld technique. For further details, see e.g. Young (1995) or consult the Rietica manual (Hunter, 1997).

The basis of the Rietveld method is the equation

$$y_{ic} = y_{ib} + \sum_k G_{ik} I_k \,, \tag{A1}$$

where y_{ic} is the calculated intensity at the i'th point of the pattern, y_{ib} is the background intensity, G_{ik} is a normalized peak profile function, and I_k is the intensity of the k'th Bragg reflection. The sum runs over all reflections contributing intensity to point i. The intensity I_k is given by the expression

$$I_k = SM_k L_k \left|F_k\right|^2 P_k A_k E_k \,, \tag{A2}$$

where S is the scale factor, M_k is the multiplicity, L_k is the Lorentz-polarisation factor, F_k is the structure factor, P_k is a factor describing the effects of preferred orientation (for powders unaffected by preferred orientation $P_k = 1$), A_k is the absorption correction and E_k an extinction correction factor. The structure factor is given by

$$F_k = \sum_{j=1}^{n} f_j e^{2\pi i(\mathbf{h}_k^t \mathbf{r}_j - \mathbf{h}_k^t \mathbf{B}_j \mathbf{h}_k)} \,, \tag{A3}$$

where f_j the scattering factor of the *j'th* atom and $\mathbf{h}_k$, $\mathbf{r}_j$ and $\mathbf{B}_j$ are matrices representing the Miller indices, atomic coordinates and anisotropic thermal vibration parameters, respectively. The superscript t indicates matrix transposition and the sum runs over the n atoms of a unit cell.

Various choices can be made for the peak profile function, G_{ik}. In the present analysis the pseudo-voight profile, which constitutes a simple convolution between a gaussian and a lorentzian profile, was used. It is given by the expression

$$G_{ik} = \gamma \frac{2}{H_k \pi}(1 + 4X_{ik}^2) + (1-\gamma)\frac{2\sqrt{\ln 2}}{H_k\sqrt{\pi}} e^{-4\ln 2 X_{ik}^2} \,, \tag{A4}$$

where H_k is the width (FWHM) of the *k'th* Bragg reflection, $X_{ik} = (2\theta_i\text{-}2\theta_k))H_k^{-1}$, and γ is the "mixing" parameter, which determines the degree of "lorentzianess" of the profile (for $\gamma = 0$ the profile is a pure gaussian profile).

The variation of the peak width is defined by the function

$$H_k = \sqrt{U\tan^2\theta + V\tan\theta + W} \,, \tag{A5}$$

where U, V, and W are refineable parameters, which in a non-trivial way describes the line broadening due to stress, strain, particle size, etc.

The positions of the Bragg peaks are determined the set of cell dimensions, in conjunction with a zero parameter and the wavelength (diffractometer constants) provided.

The goal of a Rietveld refinement is to minimize the deviation between the calculated x-ray pattern and the observed pattern, i.e. to minimize the quantity

$$R = \sum_i w_i (y_{io} - y_{ic})^2 , \tag{A6}$$

where y_{io} is the set of observed diffraction intensities, y_{ic} is the calculated intensities obtained from Equation (A1), and w_i is the weight assigned to the *i'th* observation (based on the counting statistics). R can be minimized employing a conventional minimization method, such as the Newton-Raphson algorithm (see e.g. (Press *et al*., 1992)). The real difficulty lies in establishing the model for the calculation and in choosing which parameters should be fixed and which should be allowed to vary during minimization. It is usually easy to obtain a good fit by introducing many degrees of freedom, but far more difficult to extract relevant physical information from the fit.

References

Anderson, P. W. and H. Hasegawa (1953). Considerations on double exchange. *Physical Review*, **100** (2), 675–681.

Asamitsu, A., Y. Moritomo, R. Kumai, Y. Tomioka, and T. Tokura (1996). Magneto-structural phase transitions in $La_{1-x}Sr_xMnO_3$ with controlled carrier density. *Physical Review B*, **54** (3), 1716–1723.

Ashcroft, N. W. and N. D. Mermin (1976). *Solid State Physics*. Saunders College Publishing.

Balcells, L., A. E. Carrillo, B. Mart´ýnez, F. Sandiumenge, and J. Fontcuberta (2000). Room temperature magnetoresistive sensor based on thick films manganite perovskite. *Journal of Magnetism and Magnetic Materials*, **221**, 224–230.

Benford, S. M. and G. V. Brown (1981). T–S diagram of gadolinium near the Curie temperature. *Journal of Applied Physics*, **52** (3), 2110–2112.

Bilde-Sørensen, J. (2002). Personal communication.

Bohigas, X., E. Molins, A. Roig, J. Tejada, and X. X. Zhang (2000). Room temperature magnetic refrigerator using permanent magnets. *IEEE Transactions in Magnetics*, **36** (3), 538–544.

Bohigas, X., J. Tejada, M. L. Marínez–Sarrión, S. Tripp, and R. Black (2000). Magnetic and calorimetric measurements on the magnetocaloric effect in $La_{0.6}Ca_{0.4}MnO_3$. *Journal of Magnetism and Magnetic Materials*, **208**, 85–92.

Brown, G. V. (1976). Magnetic heat pumping near room temperature. *Journal of Applied Physics*, **47** (8), 3676–3680.

Brück, E., O. Tegus, X. W. Li, F. R. de Boer, and K. H. J. Bushow. Magnetic refrigeration – towards room temperature applications. *Physica B*, *In press*.

Chick, L. A., L. R. Pederson, G. D. Maupin, J. L. Bates, L. E. Thomas, and G. J. Exarhos (1990). Glycine-nitrate combustion synthesis of oxide ceramic powders. *Materials Letters*, **10** (1,2), 6–12.

Coey, J. M. D., M. Viret, and L. Ranno (1995). Electron localization in mixed-valence manganites. *Physical Review Letters*, **75** (21), 3910–3913.

Coey, J. M. D., M. Viret, and S. von Molnar (1999). Mixed-valence manganites. *Advances in Physics*, **48** (2), 167–293.

Dai, P., J. Zhang, H. A. Mook, S.-H. Liou, P. A. Dowben, and E. W. Plummer (1996). Experimental evidence for the dynamic Jahn-Teller effect in $La_{0.65}Ca_{0.35}MnO_3$. *Physical Review B*, **54** (6), R3694–R3697.

de Gennes, P.-G. (1960). Effects of double exchange in magnetic crystals. *Physical Review*, **118** (1), 141–154.

Debye, P. (1926). *Annalen der Physik*, **81**, 1154–60.

Dessau, D. S. and Z. S. in Y.Tokura (Ed.) (1998). *Colossal Magnetoresistive Oxides*. London: Gordon and Breach.

Dionne, G. F. (1996a). Anomalous magnetoresistance in the lanthanide manganites and its relation to high-T_C superconductivity. *MIT Lincoln Laboratory, Technical Report* **1029**.

Dionne, G. F. (1996b). Magnetic exchange and charge transfer in mixed-valence manganites and cuprates. *Journal of Applied Physics*, **79** (8), 5172–5174.

Evetts, J. E., M. G. Blamire, N. D. Mathur, S. P. Isaac, B. Teo, L. F. Cohen, and J. L. Macmanus-Driscol (1998). Defect-induced spin disorder and magnetoresistance in single-crystal and polycrystal rare-earth manganite thin film. *Philosophical Transactions of the Royal Society London A*, **356**, 1593–1615.

Fontcuberta, J., L. Balcells, M. Bibesa, J. Navarro, C. Frontera, J. Santiso, J. Fraxedas, B. Mart´ýnez, S. Nadolski, M. Wojcik, E. Jedryka, and M. Casanove (2002). Magnetoresistive oxides: new developments and applications. *Journal of Magnetism and Magnetic Materials*, **242–245**, 98–104.

García-Muñoz, J. L., J. Fontcuberta, B. Martínez, A. Seffar, S. Piñol, and X. Obradors (1997). Magnetic frustration in mixed valence manganites. *Physical Review B*, **55** (2), R668–R671.

García-Muñoz, J. L., J. Fontcuberta, M. Suaaidi, and X. Obrados (1996). Bandwidth narrowing in bulk $L_{2/3}A_{1/3}MnO_3$. *Journal of Physics: Condensed Matter*, **8**, L787–L793.

Giauque, W. F. (1927). A thermodynamic treatment of certain magnetic effects. A proposed method of producing temperatures considerably below 1° absolute. *Journal of the American Chemical Society*, **49** (8), 1864–1870.

Goldschmidt, V. (1958). *Geochemistry*. Oxford University Press.

Goodenough, J. B. (1955). Theory of the role of covalence in the perovskite-type manganites [La,M(II)]MnO_3. *Physical Review*, **100** (2), 564–573.

Gschneidner, Jr., K. A. and V. K. Pecharsky (2000). Magnetocaloric materials. *Annual Review of Materials Science*, **30**, 387–429.

Guo, Y., K. Tao, Y. Liu, H. Zhou, and R. Wäppling (2000). Crystal structures and giant magnetoresistance of fluoride $La_{2/3}Ca_{1/3}MnO_3$ compounds. *Journal of Alloys and Compounds*, **296**, 33–38.

Guo, Y., X. Zhang, and R. Wäppling (2000). Crystal structure of $La_{1-x}Sr_xMnO_{3-2x+\delta}F_{2x}$. *Journal of Alloys and Compounds*, **306**, 133–140.

Guo, Z. B., Y. W. Du, J. S. Zhu, H. Huang, W. P. Ding, and D. Feng (1997). Large magnetic entropy change in perovskite-type manganese oxides. *Physical Review Letters*, **78** (6), 1142–1145.

Gupta, A., G. Q. Gong, G. Xiao, P. R. Duncombe, P. Lecoeur, P. Trouilloud, Y. Y. Wang, V. P. Dravid, and J. Z. Sun (1996). Grain-boundary effects on the magnetoresistance properties of perovskite manganite films. *Physical Review B*, **54** (22), R15629–R15632.

Gupta, A. and J. Z. Sun (1999). Spin-polarized transport and magnetoresistance in magnetic oxides. *Journal of Magnetism and Magnetic Materials*, **200**, 24–43.

Hernández, A. D., C. Hart, R. Escudero, and O. Arés (2002). Fitting of transport measurements in polycrystalline $La_{2/3}Ca_{1/3}MnO_3$. *Physica B*, **320**, 64–66.

Höhne, G. W. H., W. Hemminger, and H.-J. Flammersheim (1995). *Differential Scanning Calorimetry – An Introduction for Practitioners*. Berlin: Springer.

Hu, F., B. Shen, J. Sun, and Z. Cheng (2001). Large magnetic entropy change in $La(Fe,Co)_{11.83}Al_{1.17}$. *Physical Review B*, **64**, 012409-1–012409-3.

Hundley, M. F., M. Hawley, R. H. Heffner, Q. X. Jia, J. J. Neumeier, and J. Tesmer (1995). Transport-magnetism correlations in the ferromagnetic oxide $La_{0.7}Ca_{0.3}MnO_3$. *Applied Physics Letters*, **67** (6), 860–862.

Hunter, B. A. (1997). *Rietica version 1.7.7*. http://www.rietica.org.

Hwang, H. Y., S. Cheong, N. P. Ong, and B. Batlogg (1996). Spin polarized intergrain tunneling in $La_{2/3}Sr_{1/3}MnO_3$. *Physical Review Letters*, **77** (10), 2041–2044.

Hwang, H. Y., S.-W. Cheong, P. G. Radeaelli, M. Marezio, and B. Batlogg (1995). Lattice effects on the Magnetoresistance in Doped $LaMnO_3$. *Physical Review Letters*, **75** (5), 914–917.

Jin, S., M. McCormack, T. H. Tiefel, and R. Ramesh (1994). Colossal magnetoresistance in La-Ca-Mn-O ferromagnetic thin films. *Journal of Applied Physics*, **76** (10), 6929–6933.

Jonker, G. H. and J. H. van Santen (1950). Ferromagnetic compounds of manganese with perovskite structure. *Physica*, **16** (3), 337–349.

Ju, S., H. Sun, and Z. Li (2002). Study of magnetotransport in polycrystalline perovskite manganites. *Journal of Physics Condensed Matter*, **14**, L631–L639.

Li, X. W., A. Gupta, G. Xiao, G. Q. Gong, and G. Q. Gong (1997). Low-field magnetoresistive properties of polycrystalline and epitaxial perovskite manganite films. *Applied Physics Letters*, **71** (8), 1124–1126.

Linderoth, S. and C. S. Jacobsen (1996). Some properties of the giant magnetoresistance (GMR) material La-Y-Ca-Mn-O. *Czechoslovak Journal of Physics*, **46** (S4), 2007–2008.

Millis, A. J., P. B. Littlewood, and B. I. Shraiman (1995). Double exchange alone does not explain the resistivity of $La_{1-x}Sr_xMnO_3$. *Physical Review Letters*, **74** (25), 5144–5147.

Morelli, D. T., A. M. Mance, J. V. Mantese, and A. L. Micheli (1996). Magnetocaloric properties of doped lanthanum manganite films. *Journal of Applied Physics*, **79** (1), 373–375.

Mori, M., N. M. Sammens, and G. A. Tompsett (2000). Fabrication processing condition for dense sintered $La_{0.6}AE_{0.4}MnO_3$ perovskites synthesized by the coprecipitation method (AE = Ca and Sr). *Journal of Power Sources*, **86**, 395–400.

Morrish, A. H. (1965). *The Physical Principles of Magnetism*. New York: John Wiley & Sons, Inc.

Nagaev, E. L. (1996). Lanthanum manganites and other giant magnetoresistance magnetic conductors. *Physics – Uspekhi*, **39** (8), 781–805.

Okimoto, Y., T. Katsufuji, T. Ishikawa, A. Urushibara, T. Arima, and Y. Tokura (1995). Anomalous variation of optical spectra with spin polarization in double-exchange ferromagnet: $La_{1-x}Sr_xMnO_3$. *Physical Review Letters*, **75** (1), 109–112.

Pecharsky, V. K., A. Gschneidner, Jr., A. O. Pecharsky, and A. M. Tishin (2001). Thermodynamics of the magnetocaloric effect. *Physical Review B*, **64**, 144406-1–144406-13.

Pecharsky, V. K. and K. A. Gschneidner, Jr. (1999). Magnetocaloric effect and magnetic refrigeration. *Journal of Magnetism and Magnetic Materials*, **200**, 44–56.

Philip, J. and T. R. N. Kutty (2000). Preparation of manganite perovskites by a wet-chemical method involving a redox reaction and their characterisation. *Materials Chemistry and Physics*, **63**, 218–225.

Prellier, W., P. Lecoeur, and B. Mercey (2001). Colossal-magnetoresistive manganite thin films. *Journal of Physics: Condensed Matter*, **13**, R915–R944.

Press, W. H., S. A. Teukolsky, W. T. Vetterling, and B. P. Flannery (1992). *Numerical Recipes in Fortran* (2^{nd} edition). New York: Cambridge University Press.

Radaelli, P. G., D. E. Cox, M. Marezio, S. Cheong, P. E. Schiffer, and A. P. Ramirez (1995). Simultaneous structural, magnetic, and electronic transitions in $La_{1-x}Ca_xMnO_3$. *Physical Review Letters*, **75** (24), 4488–4491.

Rietveld, H. M. (1967). Line profiles of neutron powder-diffraction peaks for structure refinement. *Acta Crystallographica*, **22** (1), 151–152.

Rietveld, H. M. (1969). A profile refinement method for nuclear and magnetic structures. *Journal of Applied Crystallography*, **2** (2), 65–71.

Roy, M., F. F. Mitchell, S. J. Potashnik, and P. Schiffer (2000). Field dependence specific-heat of rare earth manganites. *Journal of Magnetism and Magnetic Materials*, **218**, 191–197.

Schiffer, P., A. P. Ramirez, W. Bao, and C.-W. Cheong (1995). Low temperature magnetoresistance and the magnetic phase diagram of $La_{1-x}Ca_xMnO_3$. *Physical Review Letters*, **75** (18), 3336–3339.

Shannon, R. D. (1976). Revised effective ionic radii and systematic studies of interatomic distances in halides and chalcogenides. *Acta Crystallographica A*, **32** (5), 751–767.

Smaïli, A. and R. Chahine (1997). Composite materials for Ericsson-like magnetic refrigeration cycle. *Journal of Applied Physics*, **81** (2), 824–829.

Smart, J. S. (1966). *Effective field theories of magnetism*. Philadelphia: W.B. Saunders Co.

Tegus, O., E. Brück, K. H. J. Buschow, and F. R. De Boer (2002). Transitionmetal-based magnetic refrigerants for room-temperature applications. *Nature*, **415**, 150–152.

Thomas, R. M., L. Ranno, and J. M. D. Coey (1997). Transport properties of $(Sm_{0.7}A_{0.3})MnO_3$ (A = Ca^{2+}, Sr^{2+}, Ba^{2+}, Pb^{2+}. *Journal of Applied Physics*, **81** (8), 5763–5765.

Tokura, Y. and Y. Tomioka (1999). Colossal magnetoresistive manganites. *Journal of Magnetism and Magnetic Materials*, **200**, 1–23.

Tumanski, S. (2001). *Thin film magnetoresistive sensors*. Bristol: Institute of Physics Publishing.

Urushibara, A., Y. Moritomo, T. Arima, A. Asamitsu, and Y. Tokura (1995). Insulator-metal transition and giant magnetoresistance in $La_{1-x}Sr_xMnO_3$. *Physical Review B*, **51** (20), 14103–14109.

Vertruyen, B., R. Cloots, A. Rulmont, G. Dhalenne, M. Ausloos, and P. Vanderbemden (2001). Magnetotransport properties of a single grain boundary in bulk La-Ca-Mn-O materials. *Journal of Applied Physics*, **90** (11), 5692–5697.

Volger, J. (1950). Further experimental investigations on some ferromagnetic oxidic compounds of manganese with perovskite structure. *Physica*, **20**, 49–66.

von Helmolt, R., J. Wecker, L. Haupt, and K. Bärner (1994). Intrinsic giant magnetoresistance of mixed valence La-A-Mn oxide (A = Ca, Sr, Ba). *Journal of Applied Physics*, **76** (10), 6925–6928.

Warburg, E. (1881). Magnetische Untersuchungen. *Annalen der Physik (Leipzig)*, **13**, 141–146.

Yamada, Y., O. Hino, S. Sohdo, R. Kanao, T. Inami, and S. Katano (1996). Polaron ordering in low-doping $La_{1-x}Sr_xMnO_3$. *Physical Review Letters*, **77** (5), 904–907.

Yosida, K. (1996). *Theory of Magnetism*. Springer-Verlag Berlin Heidelberg.

Young, R. A. (Ed.) (1995). *The Rietveld Method*. Oxford University Press.

Zener, C. (1951a). Interaction between the d shells in the transition metals. *Physical Review*, **81** (4), 440–444.

Zener, C. (1951b). Interaction between the s-shells in the transition metals: II. Ferromagnetic compounds of manganese with perovskite structure. *Physical Review*, **81** (3), 403–406.

Zhang, N., W. Ding, W. Zhong, D. Xing, and Y. Du (1997). Tunnel-type giant magnetoresistance in the granular perovskite $La_{0.85}Sr_{0.15}MnO_3$. *Physical Review B*, **56** (13), 8138–8142.

Zhang, N., F. Wang, W. Zhong, and W. Ding (1999). Spin-dependent interfacial tunneling and tunnel-type GMR in granular perovskite family $La_{1-x}Sr_xMnO_3$ ($0.05 \leq x \leq 0.45$). *Journal of Physics: Condensed Matter*, **11**, 2625–2635.

Zhang, X. X., J. Tejada, Y. Xin, G. F. Sun, K. W. Wong, and X. Bohigas (1996). Magnetocaloric effect in $La_{0.67}Ca_{0.33}MnO_\delta$ and $La_{0.60}Y_{0.07}Ca_{0.33}MnO_\delta$ bulk materials. *Applied Physics Letters*, **69**, 3596–3598.

Zhou, T., Z. Y. W. Zhong, X. N. Xu, H. H. Zhang, and Y. W. Du (1999). Larger magnetocaloric effect in two-layered $La_{1.6}Ca_{1.4}Mn_2O_7$. *Journal of Applied Physics*, **85** (11), 7975–7977.

Publications related to the work covered by this thesis

A. R. Dinesen, S. Linderoth, and S. Mørup (2002). Direct and indirect measurement of the magnetocaloric effect in a $La_{0.6}Ca_{0.4}MnO_3$ caramic perovskite. *Journal of Magnetism and Magnetic Materials*, **253**, 28-34.

A. R. Dinesen and S. Linderoth (2002). Adjustable temperature working range in $La_{2/3}Ca_{1/3-x}Sr_xMnO_3$ manganites with CMR effect. *Eurosensors 2002 – Book of Abstracts II*, 317-318 (extended and reviewed abstract).

A. R. Dinesen and S. Linderoth (2003) Adjustable temperature working range in $La_{2/3}Ca_{1/3-x}Sr_xMnO_3$ manganites with CMR effect. Submitted to Sensors & Actuators.

A. R. Dinesen, S. Linderoth, N. H. Pryds and S. Mørup. Magnetocaloric properties of $La_{0.67}Ca_{0.33-x}Sr_xMnO_3$. To be submitted.

Publications not related to the work covered by this thesis

A. R. Dinesen, C. T. Pedersen and C. Bender Koch (2001). The thermal conversion of lepidocrocite (γ-FeOOH) revisited. *Journal of Thermal Analysis and Calorimetry*, **64**, 1303-1310.

A. R. Dinesen, M. Eldrup, D. Juul Jensen, S. Linderoth, T. B. Pedersen, N. H. Pryds, A. Schrøder Pedersen, and J. A. Wert (Eds.) (2001). *Science of Metastable and Nanocrystalline Alloys: Structure, properties and modeling*. Risø National Laboratory, Roskilde.

Mission

To promote an innovative and environmentally sustainable technological development within the areas of energy, industrial technology and bioproduction through research, innovation and advisory services.

Vision

Risø's research **shall extend the boundaries** for the understanding of nature's processes and interactions right down to the molecular nanoscale.

The results obtained shall **set new trends** for the development of sustainable technologies within the fields of energy, industrial technology and biotechnology.

The efforts made **shall benefit** Danish society and lead to the development of new multi-billion industries.